NUMERICAL STUDIES OF DISRUPTIONS IN TOKAMAKS

by

Glen Russell Harris

A Thesis submitted for the degree of Doctor of Philosophy
of the University of London and for the Diploma
of Membership of the Imperial College

August 1989

ABSTRACT

A 1−D, two−fluid transport code has been developed to model the interaction between tearing modes, impurity radiation, additional heating, and transport processes within tokamak plasmas. Magnetic islands arise through nonlinear growth and saturation of tearing modes and their sizes are computed using first−order effects usually neglected by other authors. It is assumed the effect of the islands on global plasma properties can be described by a large enhancement in radial transport across the island. The sawtooth oscillation that is important in limiting axial current is also simulated, using the Kadomtsev model for collapse triggered by a resistive m=1 mode.

Disruption is triggered by the m=2, n=1 island growing to large size. This steepens the global current gradient and causes a cascade of instability to short wavelength modes. These modes interact with the sawtooth and provide a thermal short−circuit across the whole radius. The disruption cannot be followed into the current quench phase, but the dynamics described with this simple model agree with that of a full 3−D simulation.

An analysis of the response of the 2/1 island size to parametric variation of several plasma quantities is made, including the effects of a conducting wall, the thermal conductivity, and additional plasma heating. Heating just inside the resonant surface produces maximum destabilization of the island, while heating outside the island prevents disruption.

The postulate that the plasma becomes ballooning mode unstable as the plasma approaches disruption is investigated. The onset of instability is found to depend strongly on the shape of the q profile following sawtooth collapse.

The effects on disruption stability of radiation cooling from light impurities is studied with a coronal model which includes anomalous diffusion of impurity species. With sufficient impurity contamination, radiative contraction of the outer plasma occurs, initiating sudden 2/1 instability, with oscillations in island size and temperature characteristic of minor disruptions. Only if the radiation losses are sufficient to cause a complete collapse of island temperature to low values does interaction with the hot, central core ensue. The onset of radiation−induced 2/1 instability is found to correspond to experimental Murakami density limits for disruption−free tokamak operation.

CONTENTS

LIST OF SYMBOLS

a	minor radius
a_1	coefficient in Taylor expansion of j_b
A	vector potential
A_1, A_2	constants determined by a shooting method that determine ψ_1 near r_s
$A(Z)$	Z_{eff} dependent factor in Spitzer-Harm resistivity
$a_{\theta e,i}$	poloidal electron/ion gyroradius
B	magnetic field
B_{y0}	zero-order y direction B field in slab geometry
B_θ	poloidal magnetic field
B	normalised poloidal magnetic field
$B_{\theta s}$	poloidal magnetic field at resonant surface
B_z	toroidal magnetic field
b_1	coefficient in Taylor expansion of j_b
b	position of perfectly conducting wall
C	$135\pi/128$
C_m	constant in Bessel function solutions for minimum energy state
c_1, c_2, c_3	dimensionless constants in transport equations
D	diffusion coeffcient for impurity ions
∂W	change in potential energy
E	electric field
e	electronic charge
$F(x)$	dimensionless zero-order y direction B field in slab geometry
$F(S_b, \alpha_b)$	ballooning function
f	fraction of neutral oxygen density at wall to average deuterium density
g	gradient of straight line trajectory in $1/q_a$–n_M space
h	half-width of magnetic island
h_{21}, h_{32}	half-width of 2/1 and 3/2 islands
h_1	size of m=1 magnetic island
h_w	FWHM of additional heating
H	helicity
H_e	power density of additional electron heating
H_i	power density of additional ion density
j	current density

j	normalised toroidal current
$j_a(\psi)$	current density outside magnetic island
$j_b(\psi)$	current density inside magnetic island
k	wave number of perturbation
K	kinetic energy
K_e^{an}/K_e^{nc}	anomalous/neoclassical radial electron thermal conductivity
K_i	neoclassical ion thermal conductivity
K_1	enhancement factor for radial island transport
k_1, k_2	constants in expansion of the stability equation near r_s
L	characteristic length of current sheet
M	Murakami parameter
m_e/m_i	electron/ion mass
m	poloidal mode number
n	toroidal mode number
n_e	electron number density
n_i	ion number density
n_D	average deuterium density
n_Z	number density of impurity ion of charge z
n_{ox}	volume average of oxygen impurities summed over z
n_M	$n_D \times 10^{-19} R/B_Z$
p	total plasma pressure
p_1	temperature profile factor
P	radiated power density
$P_T(T)$	radiated power density, normalised by $n_e(r)n_0(a)$, as a function of temperature
$P_f(T)$	fitted function for P_T
P_1, P_3	maxima of P_T
P_2	minimum of P_T
P_l	power density of line radiation
P_H	total additional heating power
P_{rad}	total radiated power
P_{in}, P_{ohm}	total input/ohmic power
q	safety factor
q_0	axial safety factor
q_a	safety factor at plasma boundary
$Q_{e,i}$	electron/ion heat flux
R	major radius
R_1	radiation factor

$R(\psi)$	inverted helical flux before Kadomtsev reconnection
r_m	sawtooth mixing radius
r_s	radius of resonant surface
r_{21}, r_{s21}	radius of m=2, n=1 resonant surface
r_{s1}, r_{s11}	position of q=1 resonant surface
r_{s12}	position of second q=1 surface, inside r_{s1}
r_x	radial position of x-point
r_o	radial position of o-point
r_2	position of island outer edge
r_1	position of island inner edge
r_c	central position of island
r_H	position of maximum applied heating power density
S	magnetic Reynold's number
S_z	ionization rate coefficient
S_b	shear parameter for ballooning instability
s	slope of ψ_1 within island
t	time
t_d	doubling time for current with linear current ramp
T_e	electron temperature
T_i	ion temperature
T_{e0}	axial electron temperature
T_{ea}	electron wall temperature
T_{isl}	electron temperature of q=2 resonant surface
T_{ef}	flattened electron temperature after sawtooth collapse
T_1, T_2, T_3	temperatures for which $P_T=P_1, P_2, P_3$
u_i	vector for unknown $\begin{pmatrix} T_e \\ T_i \end{pmatrix}_i$
v	velocity
v_A	Alfven speed
v_{ox}	thermal velocity of neutral oxygen at plasma boundary
x_ψ	distance from singular surface at which series solution is fitted
x_T	half width of tearing layer
Z_{eff}	effective ionic charge of plasma
α	shaping factor for $K_e(r)$
α_j	factor of the first order term in the expression describing growth of saturated islands

α_1	shape of transport enhancement across island
α_s	shear parameter for m=1 mode
α_b	pressure parameter for ballooning instability
α_z	recombination rate coeffcient
β_1, β_2	shaping factors for profile initialization
γ	linear growth rate of perturbation (chapter 2)
γ	linear growth rate of resistive m=1 mode, reduced by diamagnetic effects (chapter 4)
γ_K	linear growth rate of ideal m=1 internal kink
γ_T	linear growth rate of resistive m=1 mode, excluding diamagnetic effects
Δ'	discontinuity in the exterior solution for ψ_1' across tearing layer
$\Delta(h)$	discontinuity in exterior solution for ψ_1' across magnetic island
Δt	timestep
Δ	grid spacing
Δt_{rad}	maximum timestep permitted by radiation
Δt_{max}	maximum timestep
δ	measure of perturbed flux at x-point
ϵ_1	tearing layer width of m=1 resistive mode
η	resistivity
η_{sp}	Spitzer resistivity when Z=1
θ_s	angular position of separatrix
λ	eigenvalue of dispersion relation for m=1 mode
μ_0	permeability of free space
μ	proportionality constant for j and B for minimum energy state (chapter 4)
μ	viscosity parameter (appendix D)
ξ	radial displacement
ρ	mass density
σ	width of deuterium density profile
τ_R	resistive time
τ_A	Alfven time
τ_{saw}	sawtooth collapse time
τ_e, τ_i	electron-ion/ion-ion collision time
τ_c	collapse time for Kadomtsev reconnection
φ	velocity stream function

Φ	implicitness parameter (chapter 3)
Φ	ratio of radiated to input power (chapter 6)
ψ	magnetic flux function
ψ_0	equilibrium magnetic flux
ψ_1	first-order perturbed magnetic flux
ψ_Z	radial flux of impurity ions of charge z
$\omega_{e,i}$	electron/ion cyclotron frequency
$\omega_{*e,i}$	electron/ion diamagnetic frequency

CHAPTER ONE

INTRODUCTION

1.1 *Disruptions in Tokamaks*

A tokamak is a toroidally shaped vacuum vessel for the production, confinement, and heating of a plasma. Tokamaks are the most promising device for achieving fusion power generation, despite the recent and apparently erroneous claims for "cold fusion" [1]. Proposed experimental reactors such as NET [2] would operate with a deuterium–tritium gas mixture and would attain temperatures necessary for thermonuclear fusion, while simultaneously meeting the Lawson criterion [3] for density and confinement time that would at least allow energy breakeven, if not net energy production. There are three main physical processes that have prevented present–day tokamaks from meeting these objectives.

(i) The electron energy and particle confinement times are up to a factor 10^2 times less than those predicted by neoclassical theory.

(ii) There is a limit to the maximum β (the ratio of plasma to magnetic pressure). As the fusion power goes as β^2, large pressures are desirable for energy production and economic viability.

(iii) The tokamak discharge frequently terminates very suddenly, with total loss of plasma confinement. These disruptions are the subject of this thesis.

Figure 1.1 shows experimental traces for the total current, oscillations of perturbed magnetic field, and soft X–ray emission during a typical disruption in the Frascati tokamak [4]. Four stages may be identified.

(1) Steady–state, stable operation.

(2) Growth to large size of a magnetohydrodynamic (MHD) perturbation with poloidal mode number m= 2. This is typically the first precursor to disruption. Many other modes can also appear later in this stage [5].

(3) Sudden loss of the thermal energy when the X–ray emission, which is a measure of the axial temperature, drops to zero. At the end of this stage, without strong external control, a fast inward motion and expansion in radius of the plasma column is observed [5], and high, localised power loads on the limiters are possible.

(4) A decay in the total current, on a slower timescale than stage (3), but still very fast compared to resistive timescales. In the JET machine [6], 7MA currents can drop to zero over only a few milliseconds, and large induced voltages and currents can

exert strong, and possibly damaging forces on the vacuum vessel.

Experimental scaling laws [7,8] allow one to predict energy breakeven as the dimensions of the tokamak are increased, so problems (i) and (ii) above can be overcome, although large and expensive tokamaks are required. However if large tokamaks are a necessity, then so too are large disruptions, and their potential for causing reactor damage increases. Any disruptions in a power reactor will also inhibit their economic viability, so NET for example has required very low disruption probabilities per discharge of 10^{-2} and 10^{-4} [2] in the two phases of it's operation. To avoid disruption and achieve these figures then greater understanding is required of the causes of disruption, and of the plasma dynamics during disruption.

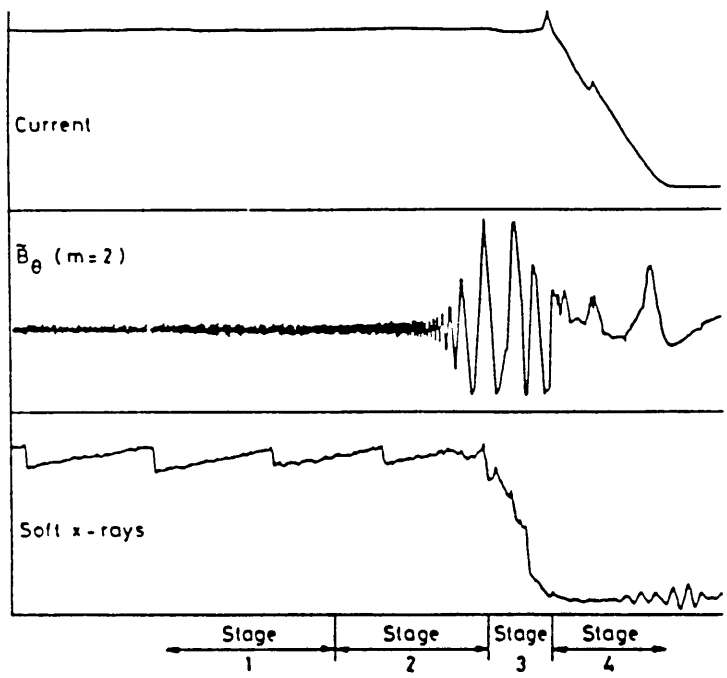

Figure 1.1 The total current, m=2 magnetic oscillations, and soft X-ray emission prior to and during a disruption on the Frascati FT tokamak. The traces occupy 30ms (from [4]).

1.2 *Aims and Layout of the Thesis*

The aim of this thesis is to discover how the stable tokamak discharge in stage (1) above can suddenly become unstable to a m=2 MHD mode, and then disrupt, without any apparent change in operating conditions. Many other authors have studied this problem, notably [9], who coupled the nonlinear theory of resistive tearing modes

to a one dimensional transport code. This approach is also taken for this thesis, but with several natural extensions to the model.

To begin chapter 2 therefore provides an introduction to, and a review of the linear and nonlinear theory of resistive tearing modes with helical symmetry. Chapter 3 then describes the development of a two-fluid, 1D transport code called TRID that is subsequently used to analyse the pre-disruptive state. Only the plasma behaviour up until the end of stage (3) of the previous section can be modelled in one dimension, and as the external circuit is not included, the current quench is also not simulated.

The m=1 sawtooth oscillation observed in tokamak discharges is reviewed in chapter 4 and a description follows of how the Kadomtsev prescription [10] for the post-collapse profiles is implemented in TRID. The response of the saturated magnetic islands to varying current is examined and disruption is interpreted as a strong interaction between the sawtooth and the m=2 island.

Chapter 5 examines the effect of varying several of the most important parameters in TRID. Firstly the catastrophe model [4] for island instability at high current is reviewed, and compared with TRID, where extra first-order terms in the saturation expression for island growth are not neglected. The position of the conducting wall is found to be more crucial in determining stability to disruption. Changes to local current gradients by additional plasma heating may have strong influences on island stability, so the effect on the islands of different positions and power levels of localised additional heating is modelled. Finally chapter 5 examines the likelihood of the pre-disruptive state being unstable to ballooning modes.

Chapter 6 is concerned with the interaction between radiation, islands, and transport. A hydrodynamic-coronal model for the oxygen impurity distributions responsible for radiative cooling is implemented within TRID. The stability to radiative collapse and island destabilization, for different impurity levels, plasma densities, and currents is studied and compared with experimental findings. The final chapter summarises the findings and outlines fruitful areas for further work.

CHAPTER TWO

THEORY OF RESISTIVE TEARING MODES

2.1 *Introduction*

The resistive MHD equations upon which this work is based are [11]:

$$\frac{\partial \rho}{\partial t} + \nabla.\rho v = 0 \tag{2.1}$$

$$\rho\left[\frac{\partial}{\partial t} + v.\nabla\right]v \equiv \rho\frac{dv}{dt} = j \times B - \nabla p \tag{2.2}$$

$$\frac{\partial B}{\partial t} = -\nabla \times E \tag{2.3}$$

$$\nabla.B = 0 \tag{2.4}$$

$$\nabla \times B = \mu_0 j \tag{2.5}$$

$$E + v \times B = \eta j \tag{2.6}$$

$$\nabla.v = 0 \tag{2.7}$$

Some insight into the relative importance of resistivity can be gained by deriving the induction equation. E and j are substituted for from eqs.(2.5) and (2.6) into Faraday's Law eq.(2.3), and assuming constant resistivity:

$$\frac{\partial B}{\partial t} = \nabla\times(v\times B) + \frac{\eta}{\mu_0}\nabla^2 B \tag{2.8}$$

The characteristic time associated with resistive diffusion of the field (second term of eq.(2.8)) is $\tau_R = \mu_0 L^2/\eta$ while the growth time for ideal instabilities is characterised by $\tau_A = 1/kv_A$, where the Alfven speed $v_A = B/(\mu_0\rho)^{1/2}$ (which can be seen from a dimensional analysis of eq.(2.2)). The magnetic Reynolds number $S \equiv \tau_R/\tau_A$ gives the relative importance of resistivity, and for typical tokamak parameters (eg. B= 1T, a= 1m, $\rho = m_H 3\times10^{19} kgm^{-3}$, $\eta = 8\times10^{-8}$(Spitzer)) equals 6×10^7. It appears from this very large S that ideal MHD should indeed provide a good description for tokamaks, but inspection of eq.(2.8) shows that, wherever the first term on the right hand side becomes equal to zero, then the resistive term is of comparable importance. The significance of large S, it shall been seen later, is to imply that this "resonant surface" where $\nabla\times(v\times B)$ is close to zero is very narrow. The problem of resistive instability becomes one of boundary layer theory; ideal MHD holds in the exterior regions

outside the resonant surface, but eigenfunctions must match to the interior region where η is not negligible.

In an ideal plasma the magnetic field lines are "frozen" into any perfectly conducting fluid [12]. This can be seen by neglecting η in eq.(2.8), integrating over a surface, and with $\psi = \int B.ds$ then

$$\frac{\partial \psi}{\partial t} + \oint (v \times dl).B = 0 \qquad (2.9)$$

$v \times dl$ is just the area/unit time swept out by an element of the periphery of the flux loop. Therefore the total flux through a surface moving with the fluid does not change in time, ie. field lines are fixed to flow, and as flow is single-valued then the field lines cannot break or change topology. This means that there may exist inaccessible states of lower magnetic energy near an initial state in ideal MHD. However the inclusion of η allows the fluid to slip relative to the field, which can break and reconnect, and the release of magnetic energy as the plasma relaxes to lower energy states drives a whole new class of resistive instabilities.

Two such resistive instabilities that are interchange in nature are the rippling mode and the resistive g-mode. They both occur at short wavelength and depend on local values of plasma quantities [13]. The g-mode occurs with large pressure gradients in regions of strong unfavourable magnetic field curvature but are stabilized by shear and are stable for tokamaks [14]. The rippling mode is located near the plasma edge in tokamaks and would have little effect on global properties and overall stability toward disruption. A third and more important resistive instability, the tearing mode is considered next.

2.2 *Linear Analysis of Tearing Modes in Plane Geometry*

The zero order field is taken to be fixed in time and assumed to have a null at $x = 0$, corresponding to the resonant surface just discussed, and is shown in figure 2.1. All distances are normalised to the width $L = (\partial F/\partial x)^{-1}$ of the corresponding current sheet, and the plasma is initially stationary. With such an equilibrium both the magnetic and velocity fields can be given in terms of scalar flux functions and the MHD equations reduce to the well known "reduced" equations, which are now derived.

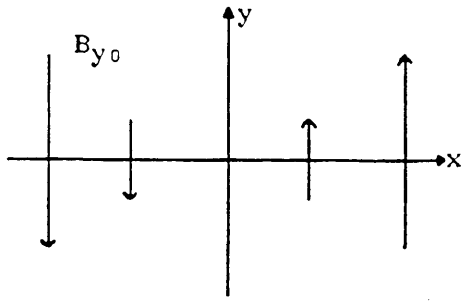

$B_{y0}=BF(x)$, $F(x)$ odd and $F(x)\approx x$, $x<<1$

$B_{z0}=B_z$, constant, $B_z>>B$

$B_{x0}=0$

Figure 2.1 Zero order B field in planar geometry, with a null at x=0.

With $\nabla.\mathbf{B}=0$ and constant B_z one has

$$\mathbf{B}= z\times\nabla\psi'+ B_z z, \quad B_x= -\frac{\partial\psi'}{\partial y}, \quad B_y= \frac{\partial\psi}{\partial x} \tag{2.10}$$

where the flux function also satisfies $\mathbf{B}.\nabla\psi'=0$. ie. $\mathbf{B}$ is tangential to surfaces of constant ψ'. Similarly for incompressible velocities, $\mathbf{v}= z\times\nabla\varphi$. Substituting eq.(2.10) into the z component of Ampere's Law eq.(2.5) gives

$$\mu_0 j_z= \nabla^2\psi' , \tag{2.11}$$

and substitution into eq.(2.8) and taking only the x component then

$$-\frac{\partial}{\partial y}\frac{\partial\psi'}{\partial t} = \frac{\partial}{\partial y}\left[v\times B\right]_z - \frac{\partial}{\partial y}\eta j_z . \tag{2.12}$$

Integrating with respect to y yields

$$\frac{\partial\psi'}{\partial t} + v.\nabla\psi= \eta j_z + E . \tag{2.13}$$

E, the constant of integration is an external (if any) imposed electric field. Finally if one operates on the momentum equation (2.2) with $z.\nabla\times$, and assumes constant density then

$$\rho\frac{\partial}{\partial t} z.\nabla\times v = z.\nabla\times(j\times B) = B.\nabla j_z , \tag{2.14}$$

and substituting for $\mathbf{v}$ and $\mathbf{B}$

$$\rho\mu_0\frac{\partial}{\partial t}\nabla^2\varphi = z.\left[\nabla\psi\times\nabla j_z\right] . \tag{2.15}$$

Equations (2.11), (2.13) and (2.15) are the reduced equations. The zero–order state of figure 2.1 is given by $\varphi = 0$, $\psi_0'(x) = BF(x)$ with $\psi_0''(x) = \mu_0 j_{z0}$. The reduced equations are now linearized, introducing a perturbation growing with growth rate γ that interacts with the resonant surface, by writing [15]

$$\psi(x,y) = \psi_0(x) + \psi_1(x)\cos ky \tag{2.16}$$

$$\varphi(x,y) = \frac{\gamma}{kB}\,\varphi_1(x)\sin ky \tag{2.17}$$

and the flows are given by

$$v_x = -\frac{\gamma}{B}\varphi_1 \cos ky \tag{2.18}$$

$$v_y = \frac{\gamma \partial \varphi_1}{kB \partial x}\sin ky \ . \tag{2.19}$$

If the perturbation is assumed to be strongly localised around $x = 0$ (i.e. narrow tearing layer x_T) then figure 2.2 illustrates the streamlines for eqs.(2.18) and (2.19). Away from $x = x_T$ there is only an x component v_x to the flow if $\partial\varphi_1/\partial x \neq 0$. Within the tearing layer there is a very rapid flow v_y away from the null at (0,0), and then return flow $-v_x$ out of the layer at $y = \pm\pi/k$. If $\eta = 0$ then the field is frozen into the flow so initially straight field lines will first bulge in toward the surface at $x = 0$, and when they enter the tearing layer will react as in figure 2.3. The strongly curved field lines here give rise to strong restoring forces, and thus in ideal MHD this flow is prevented. If resistivity is present, reconnection of the field can occur, producing a field topology as in figure 2.2. The magnetic energy can be less than in the ideal case and resistivity can allow an additional class of instabilities.

The dotted line in figure 2.2, which is the surface of zero field that divides the two topologically different regions, is called the separatrix, and such a field structure is called a magnetic island. The width $w = 2h$ is the distance between separatrices at $y = 0$. To derive h the value of ψ at the x–point (0,0) is equated to that at $(h,\pi/k)$, which is given by a Taylor series expansion of eq.(2.16),

$$\psi_s = \psi_0(0) + \psi_1(0) = \psi_0(0) + \tfrac{1}{2}h^2\psi_0''(0) - \psi_1(0) \tag{2.20}$$

so,

$$h = 2[\psi_1(0)/\psi_0''(0)]^{1/2} \tag{2.21}$$

The requirements for instability, and the linear growth rate are now calculated.

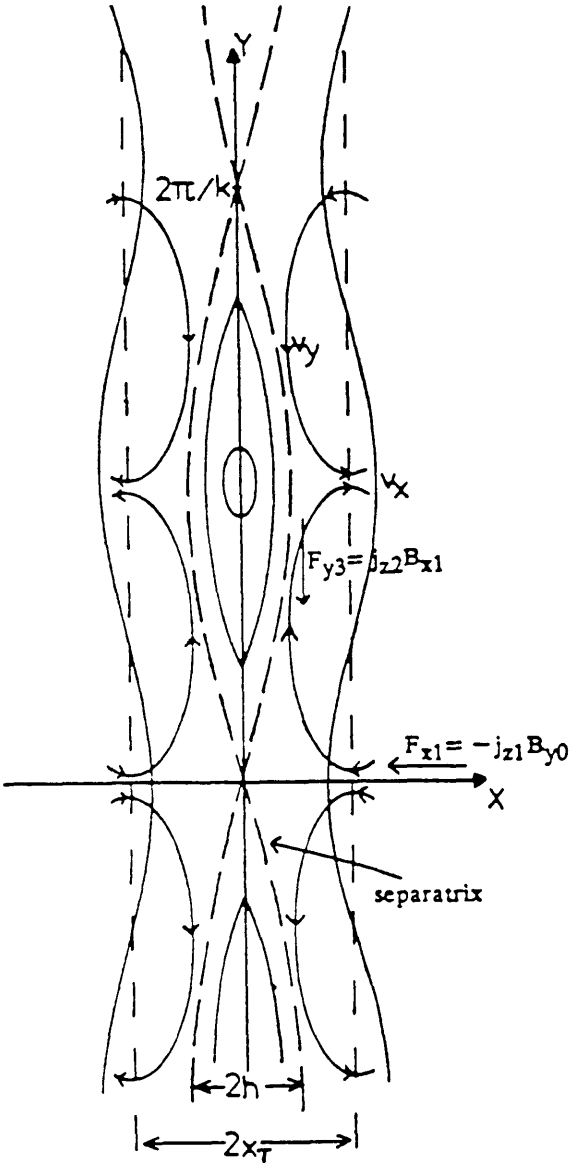

Figure 2.2 First-order fields and flows associated with a linear tearing mode, when $h<<x_T$.

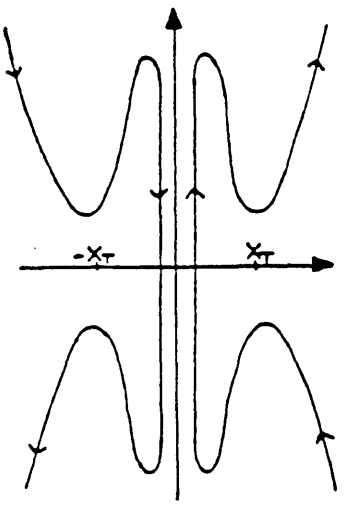

Figure 2.3 The contorted magnetic field that would result if it were frozen into the flow of the tearing motion in figure 2.2

Equations (2.16) to (2.19) are substituted into the reduced equations which when linearized give

$$\psi_1(x)-F(x)\varphi_1(x) = \frac{1}{\gamma\tau_R}\left[\psi_1''(x)-k^2\psi_1(x)\right] \qquad (2.22)$$

$$-\gamma^2\tau_A^2\left[\varphi_1''(x)-k^2\varphi_1(x)\right] = F(x)\left[\psi_1''(x)-k^2\psi_1(x)\right]-F''(x)\psi_1(x) \qquad (2.23)$$

Lengths are normalised to the shear length L, $\tau_A \equiv (\rho\mu_0)^{1/2}/kB$, and $\tau_R \equiv \mu_0 L^2/\eta$. Assumptions concerning the solution are now made that are verified *a posteriori*. The linear growth rate is assumed much less than ideal rates, $\gamma << 1/\tau_A$, and secondly the resistivity can be neglected outside the tearing layer; i.e. $\eta = 0$ for $x >> x_T$. Therefore in the exterior region where η is negligible eqs.(2.22) and (2.23) reduce to

$$\psi_1 = F\varphi_1 \qquad (2.24)$$

$$\psi_1'' - (k^2 + F''/F)\psi_1 = 0 \qquad (2.25)$$

F(x), the zero–order B field is known, so the solution of eq.(2.25) can be found. As $x_T \to 0$, eq.(2.25) becomes singular and so although the exterior solution for $\psi_1(x)$ is continous across the tearing layer, it's derivative is not, and the quantity

$$\Delta' \equiv (\psi_1'(0^+) - \psi_1'(0^-))/\psi_1(0) \qquad (2.26)$$

characterises the linear tearing mode. This exterior solution must be matched to the interior solution where eq.(2.25) no longer holds and the full equations (2.22) and (2.23) must be solved. This solution and matching is reviewed in Appendix A.

2.3 *Onset of Non–Linearity*

Inspection of eq.(A.9) reveals that $\gamma\tau_R \approx S^{2/5} >> 1$, so during a tokamak discharge evolving on resistive timescales, very many linear growth times will pass, and it is necessary to examine the nonlinear behaviour of the mode. Simple arguments are now used to derive the first–order flows in figure 2.2, and by equating the work done by these forces, a more transparent derivation of the tearing width results. The nonlinear forces that replace inertia and provide saturation of the mode are then derived, and the criterion for when they become important is developed.

The perturbation (2.16), which corresponds to perturbed field $(B_{x_1}\sin ky, B_{y_1}\cos ky)$,

induces a first-order current j_{z1} within the tearing layer. From Faraday's Law, $\partial B_{x1}/\partial t = -\partial E_{z1}/\partial y$, so

$$E_{z1} = \frac{\gamma B_{x1}}{k}\cos ky \tag{2.27}$$

and this drives a current

$$j_{z1} = \frac{\gamma B_{x1}}{\eta k}\cos ky \tag{2.28}$$

When crossed with the equilibrium field this produces first-order forces, as in figure 2.2, that drive a vortex flow into the x-point and a return flow from the island centre. $F_{x1} = -j_{z1}B_{y0}$, or

$$F_{x1} = \frac{-\gamma B_{x1}B_{y0}}{\eta k}\cos ky \tag{2.29}$$

Away from the singular layer the v_x flow this force produces is given by Ohm's Law, $v_x = -E_{z1}/B_{y0}$ (η negligible), or

$$v_x = \frac{-\gamma B_{x1}}{kB_{y0}}\cos ky \tag{2.30}$$

The presence of a large B_z implies incompressible flow [16], so the v_x must be balanced by a strongly sheared v_y flow over the narrow width x_T:

$$v_y = \int \frac{-\partial v_x}{\partial x}dy = \frac{\gamma B_{x1}}{k^2 B'_{y0} x_T^2}\sin ky \tag{2.31}$$

where $\partial/\partial x \to 1/x_T$ and $B_{y0} = B'_{y0}x_T$. The work done driving the v_x flow is balanced by the energy dissipated by the v_y flow so

$$\frac{1}{k}F_{y1} = \rho\gamma v_y = F_{x1}x_T \tag{2.32}$$

Substituting eq.(2.29) and (2.31), the tearing width is found to be

$$x_T = \left[\frac{\gamma\rho\eta}{[kB'_{y0}]^2}\right]^{1/4} \tag{2.33}$$

which, substituting τ_A and τ_R, is identical to eq.(A.10), except for a factor of two.

As the mode grows in amplitude, nonlinear forces become large, replacing inertia as the mechanism opposing growth of the mode. Second-order j×B forces arise

$$F_{x2} = -j_{z1}B_{y1} = \frac{-\gamma B_{x1}B_{y1}}{\eta k}\cos^2 ky \tag{2.33}$$

that do not contribute to the torque driving the vortex flow, so forces to third order must be considered. Second-order y-independent currents are induced by the flow:

$$j_{z2} = v_x B_{y1} - v_y B_{x1} = \frac{-\gamma B_{x1}^2}{k^2 B'_{y0} x_T^2} \tag{2.34}$$

where $B_{y1} = B_{x1}/kx_T$ (implied by $\nabla.B = 0$) has been used. When j_{z2} is crossed with B_{x1} the resulting third-order force F_{y3} provides a torque that opposes that produced by linear forces.

$$F_{y3} = j_{z2}B_{x1} = \frac{-\gamma B_{x1}^3 \sin ky}{k^2 B'_{y0} x_T^2} \tag{2.35}$$

This time requiring $F_{y3}/k = F_{x1}x_T$ then gives the condition

$$x_T = \left[\frac{B_{x1}}{kB'_{y0}}\right]^{1/2} \tag{2.36}$$

The definition (2.10) of ψ_1 implies $B_{x1} = k\psi_1$ and $B_{y0}' = \psi_0''$ so eq.(2.36) is equivalent to $x_T = |\psi_1/\psi_0''|^{1/2}$. This is the same as eq.(2.21) for the island width, neglecting numerical factors. The nonlinear and linear forces are therefore of comparable size when the island has grown to become as wide as the tearing layer. For tokamak evolving on resistive timescales, over tearing width dimensions, this would occur very rapidly, so the dynamics of magnetic islands will always be nonlinear. The replacement of inertia by nonlinear forces decreases the growth rate γ so the inertial term in eq.(2.15) is unimportant and $\nabla\psi \times \nabla j_z = 0$, which implies

$$j_z = j_z(\psi) \tag{2.37}$$

Rutherford [17] has analysed this case, assuming small islands compared to the shear

length of the equilibrium field, and constant ψ within the singular region. It is found that growth of the mode becomes proportional to Δ'. This is easy to show.

At the o–point v= 0, so eq.(2.13) gives

$$\partial\psi_1/\partial t = \eta(0) j_{z1}(0) \tag{2.38}$$

Within the tearing layer, if j_{z1} is assumed constant, and $\partial^2/\partial x^2 >> k^2$, then eq.(2.11) becomes, when integrated across the layer

$$j_{z1}(0)2h \simeq \Delta'\psi_1(0) \tag{2.39}$$

Combining eq.(2.38) and (2.39) the growth of h is given by

$$\frac{dh}{dt} = \frac{\Delta'\eta(0)}{2\mu_0} \tag{2.40}$$

During a tokamak discharge, many growth times of eq.(2.40) will pass, so the island will become comparable to the shear length. Equation (2.40) has therefore been quasilinearly extended by White et al. [18] for the case h/L≈1. As the interior region, which now corresponds to the island is large, the constant ψ_1 (and j_{z1}) approximation can no longer be made, and the matching of solutions is now made at the island separatrices.

2.4 *Saturation of Island Growth*

As $x_T << L$, then all previous linear results will hold in more complicated tokamak geometry, although the solution for ψ_1 in the exterior region, upon which Δ' depends, will strongly depend on this geometry. Therefore before discussing saturation of the tearing mode, the fields and equations valid for the cylindrical tokamak approximation are given.

The well known [16,19] low–beta cylindrical tokamak ordering is assumed, ($a/R << 1$, $aB_z/RB_\theta \approx 1$), and furthermore only single perturbations with fixed helical symmetry are considered. Therefore the nonlinear coupling of modes of different helicity is excluded. These assumptions imply the torus can be replaced by a cylinder of length $2\pi R$, the φ–coordinate replaced by $z = \varphi R$, all plasma quantities are a function only of r, $m\theta + kz$, and t. Perturbations of the form

$$\psi_1(r)e^{i(m\theta+kz)}, \qquad k=-n/R \tag{2.40}$$

may then be considered, where m and n are the poloidal and toroidal mode numbers. The helical symmetry eliminates the z–coordinate since

$$\frac{\partial}{\partial z} = \frac{k}{m}\frac{\partial}{\partial \theta} \tag{2.41}$$

Singular surfaces do not now occur for a null in the equilibrium field as in the plane case, but when the second term of eq.(2.8) equals zero; i.e. $\nabla\times(v\times B_0)= B_0.\nabla v= 0$. Using eq.(2.40) this implies

$$\frac{mB_{\theta 0}}{r}\left[1-\frac{n}{m}q(r)\right]v=0 \tag{2.42}$$

where the safety factor q(r) is defined by

$$q(r) \equiv \frac{rB_z}{RB_{\theta 0}} \tag{2.43}$$

Tearing modes grow about the mode rational surface where $q(r_s)= m/n$. Requiring this surface to correspond to $\partial\psi_0/\partial r= 0$ (analogous to the plane case), and the fact that $\nabla.B= 0$ allows **B** to be written in terms of a helical flux function:

$$B \equiv z\times\nabla\psi - \frac{kr}{m}B_z\theta + B_z z \tag{2.44}$$

The equilibrium helical flux satisfies

$$\frac{\partial\psi_0}{\partial r} = B_{\theta 0}\left[1-\frac{n}{m}q\right] \tag{2.45}$$

With the definition (2.44) the reduced equations are the same as in section 2.2, except ∇ is replaced by $\nabla_\perp\equiv\nabla-z\partial/dz$, and eq.(2.11) now becomes

$$\nabla_\perp^2\psi - \frac{2kB_z}{m} = \mu_0 j_z(\psi) \tag{2.46}$$

Saturation of the tearing mode is now considered. A single pitch perturbation expansion of the form

$$\psi = \psi_0(r) + \epsilon\psi_1(r)\cos m\theta + \epsilon^2(\psi_{20}(r)+\psi_2(r)\cos 2m\theta) + \ldots \qquad (2.47)$$

$$j = j_a(\psi_0+\Delta\psi) + \epsilon\Delta j_1(\psi_0+\Delta\psi) + \ldots \qquad (2.48)$$

where ψ_0 and $j_a(\psi_0)$ are the unperturbed quantities, is substituted into eq.(2.46) to give

$$\left[\psi_0'' + \frac{1}{r}\psi_0' - 2kB_z/m\right] + \epsilon\left[\psi_1'' + \frac{1}{r}\psi_1' - \frac{m^2}{r^2}\psi_1\right]\cos m\theta + \ldots = \mu_0 j_0(r) + \epsilon\mu_0 j_1(r)\cos m\theta$$
$$= \mu_0 j(\psi) \qquad (2.49)$$

From eq.(2.21) the expansion parameter $\epsilon \approx \frac{1}{4}h^2\psi_0''$. This is very small, and so there should be little error in excluding the effects of mode–coupling. To first order eq.(2.49) becomes

$$\left[\psi_1'' + \frac{1}{r}\psi_1' - \frac{m^2}{r^2}\psi_1\right]\cos m\theta = \mu_0\frac{\partial j_a}{\partial\psi}\bigg|_{\psi_0}\psi_1\cos m\theta + \mu_0\Delta j_1(\psi_0) = \mu_0 j_1(r)\cos m\theta. \qquad (2.50)$$

Δj_1, the change in the functional form of $j(\psi)$, must equal zero so eq.(2.50) can be rewritten as

$$\frac{\partial^2\psi_1}{\partial r} + \frac{1}{r}\frac{\partial\psi_1}{\partial r} - \left[\frac{m^2}{r^2} + \frac{\mu_0 j_{z0}'}{B_{\theta 0}(1-\frac{n}{m}q)}\right]\psi_1 = 0 \qquad (2.51)$$

Equation (2.51) shall henceforth be called the stability equation, and is the cylindrical equivalent of eq.(2.25). It is singular where $q(r_s) = m/n$, and like the plane case, applies in the region exterior to the island. Within the island ψ_1 and $j(\psi)$ are not now taken constant as in [17], but are assumed to be [18]

$$\psi(r,\theta) = \psi_0(r) + \epsilon\psi_1(r_x)(1+sx)\cos m\theta \qquad (2.52)$$

$$j_b(\psi) = a_1 + b_1\psi \qquad \text{for } \psi > \psi_s = \psi(r_x) \qquad (2.53)$$

A Taylor expansion of $\psi_1(r)$ has been made about r_x, the position of the x–point, so $x = r - r_x$ and the slope s of ψ_1 within the island is

$$s \equiv \psi_1'(r_x)/\psi_1(r_x) \qquad (2.54)$$

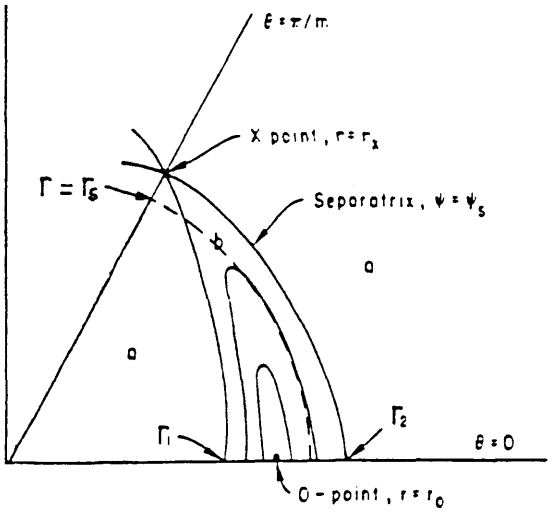

Figure 2.4 Surfaces of constant helical flux $\psi(r,\theta)$, for a large magnetic island in cylindrical geometry. The island region b is bounded by the separatrix $\psi=\psi_s$, which separates it from the exterior region a.

With such a perturbation, the cylindrical island structure of figure 2.4 arises. If $\psi_0(r)$ in eq.(2.52) is expanded about the x−point, and δ is defined to be

$$\delta \equiv -2\psi_1(r_x)/\psi_0''(r_x) \tag{2.55}$$

then the angular position of the separatrix is given by

$$\cos m\theta_s = \frac{-1-sx-x^2/\delta}{1+sx} \tag{2.56}$$

If s is negative, the x− and o−points are shifted outward and inward respectively from the singular surface

$$r_x=r_s-\delta s/2, \qquad r_o=r_s+\delta s/2 \tag{2.57}$$

Substituting $\theta_s=0$ into eq.(2.56), the island half−width is found to be

$$h=(2\delta+\delta^2s^2)^{1/2} = [-4\psi_1(r_s)/\psi_0''(r_s)]^{1/2} \tag{2.58}$$

The inner and outer edges of the island are not equidistant from r_s for large islands, and are located at

$$r_2 = r_s + h(1+hs/4)$$
$$r_1 = r_s - h(1-hs/4) \qquad (2.59)$$

Equation (2.53) corresponds to the first two terms of a Taylor series expansion of $j(\psi)$, and a_1 and b_1 are constants that are solved for by matching ψ in the island and exterior regions across the separatrix. Integration of eq.(2.49) times $\cos m\theta$ gives

$$\psi_1'' + \frac{1}{r}\psi_1' - \frac{m^2}{r^2}\psi_1 = \frac{2\mu_0 m}{\pi}\left[\int_0^{\theta_s} j_b(\psi)\cos m\theta d\theta + \int_{\theta_s}^{\pi/k} j_a(\psi)\cos m\theta d\theta\right] \qquad (2.60)$$

and this is then integrated across the island between r_1 and r_2. The first term gives

$$\int_{r_1}^{r_2}\psi_1''dr = \psi_1'(r_2) - \psi_1'(r_1) \equiv \Delta(h)\psi_1(r_x) \qquad (2.61)$$

The $\Delta(h)$ defined here equals Δ' of the previous section for small h, and is given by solution of the stability equation (2.51). The integrals of the right hand side of eq.(2.61) are tedious but non-trivial, and first involve transforming $j_a(\psi)$ to a function of x and θ, and then transforming the resulting functions of θ_s to functions of x before integrating over the island. Equation (2.60) then relates $\Delta(h)$ to a_1 and b_1, but a second condition is necessary to fully determine them. Integrating eq.(2.49) over θ, the change in total current can be shown to be of order ϵ^2, so to order $\epsilon^{3/2}$ (or h^3) current is conserved and

$$\int_{r_1}^{r_2} j_a(\psi_0))dr = \frac{\pi}{m}\int_{r_1}^{r_2}\int_0^{\pi/m} J(\psi)d\theta dr \qquad (2.62)$$

Carrying out the integrations we find a trivial typographical error in [18] (the 124/135 factor should read 128/135).

This matching relates the amplitude of ψ_1 to the island width h. Evolution of the island is then determined by eq.(2.13). If this is averaged along lines of constant ψ the convective term gives zero contribution. At the x- and o-points eq.(2.13) then reduces to

$$\frac{\partial}{\partial t}\psi(r_x) = \eta(r_x)j(r_x) + E \qquad (2.63)$$

$$\frac{\partial}{\partial t}\psi(r_o) = \eta(r_o)j(r_o) + E \qquad (2.64)$$

Equations (2.63) and (2.64) are subtracted, and using $2\psi_1(r_s) = (\psi_1(r_x) + \psi_1(r_o))$, expanding $\eta(r_x) = \eta_s[1 - \delta s\eta_s'/2\eta_s]$, and substituting

$$j(r_o)=a_1+b_1\psi_0(r_o)+b\psi_1(r_o)$$
$$j(r_x)=a_1+b_1\psi_0(r_x)+b\psi_1(r_x) \qquad (2.65)$$

gives,

$$\frac{\partial}{\partial t}\psi_1(r_s) = \psi_1(r_s)\frac{\eta_s}{\mu_0}\left[b_1-\frac{s\eta_s' j_a(r_s)}{\eta_s\psi_0''(r_s)}\right] \qquad (2.66)$$

Only terms to order h^2 have been retained. With the definition (2.58) of island width it follows that

$$\frac{dh}{dt} = \frac{C\eta_s}{2\mu_0}\left[\frac{1}{2}\Delta(h)-\alpha_j h\right] \qquad (2.67)$$

where $C=135\pi/128$, and

$$\alpha_j = \left[\frac{m^2}{r_s^2}-\frac{s}{r_s}\right] + \frac{1.34s\mu_0 j_a'(r_s)}{\psi_0''(r_s)} + (1-C^{-1})\frac{\mu_0 j_a''(r_s)}{\psi_0''(r_s)} + \frac{s\eta_s'\mu_0 j_a(r_s)}{C\eta_s\psi_0''(r_s)} \qquad (2.68)$$

$\Delta(h)$ is given by the exterior solution of eq.(2.51) and s, the slope of ψ_1 in the island interior, is taken as the average value of ψ_1' at the island edges, where ψ_1' is also obtained from solution of eq.(2.51):

$$s = \frac{1}{2}\left[\psi_1'(r_2)+\psi_1'(r_1)\right] \qquad (2.69)$$

White et al. [18] find an additional term in eq.(2.68) proportional to $\Delta(0)$. How this might arise is not obvious to the author and is neglected here.

For a given equilibrium, the zeros of eq.(2.67) correspond to a saturated island, i.e.:

$$\Delta(h_{sat})=\alpha_j h_{sat} \qquad (2.70)$$

For h_{sat} small it is frequently supposed to be a good approximation to take $\alpha_j h_{sat}=0$ [4,9,20]. This is not a requirement for this work, and the validity and consequences of this assumption are examined in Chapters 4 and 5. The equilibrium profiles, and therefore $\Delta(h)$ and α_j, evolve in time, so eq.(2.67) then describes the growth of a saturated island in response to a changing current profile.

The preceding analysis is invalid for the special case of m=1 [52]. This can be seen if eq.(2.51) is rearranged, substituting eq.(2.46) for $\mu_0 j'_{z0}$, and noting $B_{\theta 0}(1-nq/m)=\psi'_0$, so the stability equation becomes

$$\psi'_0\frac{d}{dr}r\psi'_1 - \psi_1\frac{d}{dr}r\psi'_0 = \frac{m^2-1}{r}\psi'_0\psi_1 \qquad (2.71)$$

For m=1 the solution of eq.(2.71) is $\psi_1=c\psi'_0$ where c is a constant. Also, in the exterior region where this holds, eq.(2.13) implies $\psi_1+\xi\psi'_0=0$, where the radial displacement ξ is defined by $v_r=\gamma\xi$. Therefore the solution for ξ to first order in kr/m is

$$\begin{aligned} \xi(r) &= \xi_0 \quad r<r_s \\ &= 0 \quad r_s<r<a \end{aligned} \qquad (2.72)$$

The solution for ξ outside r_s must equal zero to match the boundary condition $\xi(a)=0$. The singularity at r_s is resolved by either including inertia which gives an ideal m=1 mode, or else resistivity as well, to give a resistive mode. The resolution of the singularity allows a matching of the two solutions in eq.(2.72), but due to the large change in ξ across the singular layer the constant-ψ approximation no longer holds, so the m=1 mode must be treated differently. The solution (2.72) represents a constant displacement of the central region and has no analogue in slab geometry. The m=1 mode is discussed further in Chapter 4.

2.5 *Tearing Modes and Energy*

Detailed calculations of the changes in magnetic energy across the tearing layer have been made in ref. [21]. This section highlights the main points. The change in magnetic energy for incompressible flow is [22]

$$\delta W = \frac{1}{2}\int\left[\frac{1}{\mu_0}B_1^2 + j_0\cdot(\xi\times B_1)\right]d^3x \qquad (2.73)$$

In plane geometry with the fields and flow of eqs.(2.16) to (2.19), and noting $\mu_0 j_{z0}=\psi''_0=BF'$ then eq.(2.73) becomes

$$\delta W = \frac{1}{4\mu_0}\int\left[\psi_1'^2 + k^2\psi_1^2 - F'\frac{d}{dx}(\varphi_1\psi_1)\right]dx \qquad (2.74)$$

In the exterior region $\varphi_1=\psi_1/F$ (from eq.(2.24)), and then integrating the last term by

parts, eq.(2.74) equals

$$\delta W = \frac{1}{4\mu_0}\int_{-\infty}^{\infty}\left[\psi_1'^2 + k^2\psi_1 + \frac{F''}{F}\psi_1^2\right]dx - \frac{1}{4\mu_0}\left[\frac{F'}{F}\psi_1^2\right]_{-\infty}^{\infty} \qquad (2.75)$$

The surface term is of order $1/x_T$, but ref.[21] shows this term is cancelled by contributions from the interior region. Within the singular layer there is a large redistribution of magnetic energy from the tearing layer outward into a skin layer, which is still small compared with the scale length of the zero-order field. However the net magnetic energy released comes from outside this region and is given by eq.(2.75), with the surface term set to zero. It is a simple matter to show this energy is dissipated only within the tearing layer. The kinetic energy K equals $\int \frac{1}{2}\rho v^2 dV$, and substituting for v and τ_A this becomes

$$K = \frac{1}{4\mu_0}\tau_A^2\gamma^2\int\left[\varphi_1'^2 + k^2\varphi_1^2\right]dx \qquad (2.76)$$

If the first term is integrated by parts, and eq.(2.23) is used, then

$$K = \frac{1}{4\mu_0}\gamma^2\tau_A^2\left[\varphi_1\varphi_1'\right]_{-\infty}^{\infty} + \frac{1}{4\mu_0}\int_{-\infty}^{\infty}F\varphi_1\left[\psi_1'' - k^2\psi_1 - \frac{F''}{F}\psi_1\right]dx \qquad (2.77)$$

In plane geometry φ_1 is odd so the surface term equals zero. In cylindrical geometry this is not the case but as $\gamma^2\tau_A^2 << 1$, the surface term may still be neglected. In the exterior region the integrand of eq.(2.77) is just the stability equation, and so equals zero. Contributions to K must therefore come only from the interior region.

The potential energy can also be related to $\Delta'(0)$. This will be done for the cylindrical geometry more applicable to tokamaks so deriving δW in an identical fashion to eq.(2.75):

$$\delta W = \frac{\pi^2 R}{\mu_0}\int_0^a\left[\psi_1'^2 + \left[\frac{m^2}{r^2} + \frac{\mu_0 j_{z0}'}{B_{\theta 0}(1-\frac{n}{m}q)}\right]\psi_1^2\right]rdr \qquad (2.78)$$

Integrating $\psi_1'^2$ by parts gives

$$\delta W = \frac{\pi^2 R}{\mu_0}\left\{\left[r\psi_1\psi_1'\right]_0^a - \int_0^a\psi_1\left[\frac{1}{r}\frac{\partial}{\partial r}r\frac{\partial\psi_1}{\partial r} - \left[\frac{m^2}{r^2} + \frac{\mu_0 j_{z0}'}{B_{\theta 0}(1-\frac{n}{m}q)}\right]\psi_1\right]rdr\right\} \qquad (2.79)$$

The integrand of eq.(2.79) equals zero. The surface term gives an energy proportional to $\Delta'(0)$, and if there is also a vacuum region between the plasma boundary at r=a

and a conducting wall at r= b then

$$\delta W = \frac{\pi^2 R}{\mu_0}\left\{-r_s\psi_1^2(r_s)\Delta'(0) - ma\psi_1^2(a)\left[1+\left[\frac{a}{b}\right]^{2m}\right]\left[1-\left[\frac{a}{b}\right]^{2m}\right]^{-1}\right\} \qquad (2.80)$$

Whenever Δ' is positive then growth of a tearing mode permits a reduction in magnetic energy. The second term of eq.(2.80) is always negative and destabilizing. When $b\to a$ then $\psi_1(a)$ also tends to zero, so the case of a conducting wall on the plasma corresponds to minumum destabilization, while the opposite limit of $b\to\infty$ is most destabilizing. The effect of the current profile can be seen from eq.(2.78). The only negative contribution to δW can come from the current gradient term. Tokamak profiles invariably have j'_{z0} negative and this is weighted strongly by the $(1-nq(r)/m)^{-1}$ factor, which is large and positive for $r< r_s$, and large and negative for radii greater than r_s. Therefore large current gradients just inside r_s are strongly destabilizing, but for $r> r_s$ they have a stabilizing effect. Finally the $(m/r)^2$ line−bending term will give a large positive contribution to δW for large m, so high−m modes could be expected to be much more stable than low−m tearing modes.

CHAPTER THREE

DESCRIPTION OF THE TRID CODE

3.1 *Introduction*

This chapter describes a time–dependent one dimensional computer code which is used to follow the interaction between transport, radiation, magnetic islands and disruptions; hence the name TRID. The equations and transport coefficients that constitute TRID are presented, and the algorithmn and computational methods used to solve them are briefly outlined. A more detailed description then follows of the solution of the stability equation, and finally an example of some low current results with $q>1$ are presented.

3.2 *Choice of Model*

Chapter 2 showed how resistive instabilities are governed by plasma profiles and in particular the radial current profile. These profiles are transport–determined, and transport in turn is affected by the presence of instabilities. A full simulation of this interaction would require:

(i) a three dimensional simulation including several potentially unstable modes,

(ii) a self consistent evolution of the temperature profile,

(iii) a simulation on transport timescales,

for a study of how disruptive conditions might arise. However the saturation mechanism discussed in chapter 2, in which island widths depend on radial profiles only, presents us with the possibility of modelling in one dimension and not three. The transport across the complicated three dimensional flux surfaces of islands must then in this case be averaged to give an equivalent 1–D effect. Also with a 1–D model it is not prohibitively expensive on the computer to obtain equilibria with saturated islands, and it becomes possible to realise the aim of understanding the parametric behaviour of disruptions with radiation cooling and additional heating. The assumptions inherent in a 1–D description will not allow a precise prediction of plasma behaviour, but the results obtained reproduce many of the features observed in a recent 3–D simulation by Bondeson [23].

The model assumes a large aspect ratio cylindrical tokamak with standard tokamak

ordering introduced in section 2.2. It follows the "TRINIO" model conceived by Turner and Wesson [9], but with several additions and changes which are summarised here.

(i) A two fluid model is used whereas TRINIO is one fluid.

(ii) A realistic radiation loss term is included in the electron energy equation. Power loss profiles are obtained from a one dimensional inpurity transport model, and the effect of impurities on Z_{eff} and ohmic heating is consequently known.

(iii) Simple additional heating terms are included in the energy equations.

(iv) A criterion for ballooning mode stability is tested.

(v) The Kadomtsev model of the sawtooth oscillation can be included explicitly in the code. Alternatively the average effect of the sawtooth is represented, although in a different fashion to [9].

(vi) Non-uniform thermal conductivity is allowed for.

(vii) The first order term in the nonlinear growth equation (2.67) is included. Islands are not symmetric about r_s.

3.3 *Transport Equations*

The basic equations used are those introduced in chapter 1; eqs.(2.1) to (2.6). A large aspect ratio, low beta tokamak of circular cross-section is assumed [19] with B_z constant and quantities varying in radius and time only. Numerous experiments [26,28,48] have found that particle diffusion is anomalous with diffusion coefficient D in the range $0.5-1.0\ m^2s^{-1}$, but to obtain agreement with observed density profiles an anomalous inward particle flux is also required. To model tokamak density evolution it is therefore necessary to compute profiles with a poorly understood diffusion coefficient, and then "fix" it with an equally misunderstood pinch term. Therefore in TRID a deuterium plasma is assumed that is Gaussian in radial profile, and is constant in time. This assumption also obviates the need for a calculation of, or an analytic model for the neutral deuterium density, from which the particle source term can be calculated.

The plasma energy content is modelled by:

(i) Electron Energy Equation

$$\frac{3}{2}\frac{\partial}{\partial t} n_e k T_e = \eta j_z^2 - \frac{1}{r}\frac{\partial}{\partial r} r Q_e - \frac{3 m_e n_e k}{m_i \tau_e}\left[T_e - T_i\right] + H_e - P \qquad (3.1)$$

(ii) Ion Energy Equation

$$\frac{3}{2}\frac{\partial}{\partial t} n_i k T_i = -\frac{1}{r}\frac{\partial}{\partial r} r Q_i + \frac{3 m_e n_e k}{m_i \tau_e}\left[T_e - T_i\right] + H_i \qquad (3.2)$$

Advection terms in the energy equations have been neglected. Assuming quasi-neutrality the electron density n_e equals the background ion density n_i plus a contribution from any impurities that may be present, i.e. $n_e = n_i + \Sigma n_z z$. The source and sink terms on the right hand side of (3.1) are respectively ohmic heating, thermal conduction, equipartition, additional heating H_e, and impurity radiation loss P. Also omitted from eq.(3.1) are energy losses associated with ionization of the impurities, and the power needed to heat the resulting electrons. Mercier et al. [29] in a more complete simulation of TFR showed that line radiation losses typically 300kW and ionization losses much smaller at 30kW. The radiation term P in eq.(3.1) therefore slightly underestimates the impurity cooling; inclusion of this effect would be useful in further work.

The effects of additional heating and radiation are not discussed until chapters 5 and 6 respectively so the functional forms assumed for $H_{e,i}$ and P are not given until then. The total low-Z impurity density is found in chapter 6 to be at most just a few percent of the deuterium density, so it is reasonable to neglect contributions from impurities to the total plasma thermal energy. Bremsstrahlung radiation through free-free collisions of electrons with the bulk deuterium ions is assumed small in comparison to impurity radiation and is neglected. The resistivity is taken to be given by the classical Spitzer-Harm expression [24]

$$\eta = \frac{5.2\times10^{-5} \ln\Lambda}{A(Z)\, T_e^{3/2}(eV)}\ \Omega m, \quad \text{or } \eta \equiv \frac{\eta_{sp}}{A(Z)}, \text{ where} \qquad (3.3)$$

$$A(Z) = \frac{1.957}{Z}\left[0.29 + \frac{0.46}{(1.08+Z)}\right] \qquad (3.4)$$

If the electron-ion collision time is eliminated in favour of the resistivity then the equipartition term becomes

$$\frac{6 n^2 e^2 \eta\, k}{m_i}\left(T_e - T_i\right) \qquad (3.5)$$

Ampere's Law, Faraday's Law and Ohm's law are respectively:

$$\mu_0 j_z = \frac{1}{r}\frac{\partial}{\partial r} rB_\theta \ , \qquad \frac{\partial B_\theta}{\partial t} = \frac{\partial E_z}{\partial r} \ , \qquad E_z = \eta j_z \tag{3.6}$$

and these can be combined to give

(iii) Poloidal Magnetic Field Equation

$$\frac{\partial B_\theta}{\partial t} = \frac{\partial}{\partial r}\frac{\eta}{\mu_0 r}\frac{\partial}{\partial r} rB_\theta \tag{3.7}$$

This set of equations can be solved for the three unknowns T_e, T_i, and B_θ if the transport quantities and source terms can be given in terms of these variables in some way.

3.4 *Transport Coefficients*

Neoclassical transport theory [15] was formulated to take into account the geometry of magnetic fields in tokamaks and their effect on particle behaviour. Some predictions seem to be confirmed by experiment, such as the ion thermal conductivity being within a factor two of the neoclassical value. However both the cross-field particle diffusion and electron thermal conductivity appear to be one or two orders of magnitude greater than the theoretical values [25,26]. For this reason a semi-empirical transport model is employed where only the diagonal coefficients that couple the thermodynamic forces to the fluxes are taken. Where there is disagreement between theory and experiment, an anomalous value that scales according to experiment is added to the neoclassical value. Therefore the heat fluxes have the form

$$Q_e = -\left[K_e^{nc} + K_e^{an}\right]\frac{\partial T}{\partial r}e \ , \qquad Q_i = -K_i^{nc}\frac{\partial T}{\partial r}i \tag{3.8}$$

The neoclassical coefficients are derived in Hinton and Hazeltine [15], but the value used for K_i^{nc} is the modified version due to Bolton and Ware [27]:

$$K_{e,i}^{nc} = \frac{n_{e,i}\epsilon^{\frac{1}{2}}a_{\theta e,i}^2}{\tau_{e,i}} K_{2e,i}[\nu_{*e,i}, \epsilon] \tag{3.9}$$

where $\epsilon = r/R$, $a_{\theta e,i}$ is the poloidal electron/ion gyroradius

$$a_{\theta e,i} = \frac{v_{te,i}}{\omega_{e,i}}\frac{B}{B_\theta} \tag{3.10}$$

$\omega_{e,i}$ the cyclotron frequency $eB/m_{e,i}$, and $v_{te,i}$, the thermal velocity,

$$v_{te,i} = \left[\frac{2kT_{e,i}}{m_{e,i}} \right]^{1/2} \tag{3.11}$$

The electron−ion and ion−ion collision times are defined by

$$\tau_e = \frac{\left[4\pi\epsilon_0\right]^2 3m_e^{\frac{1}{2}} \left[kT_e\right]^{\frac{3}{2}}}{4(2\pi)^{\frac{1}{2}} e^4 Z^2 n_i \ln\Lambda} \quad , \qquad \tau_i = \frac{\sqrt{2}}{Z^2} \left[\frac{m_i}{m_e}\right]^{\frac{1}{2}} \left[\frac{T_i}{T_e}\right]^{3/2} \tau_e \tag{3.12}$$

The functions K_1, $K_{2e,i}$, and K_3 in eq.(3.9) are rational functions of the collisionality parameters $\nu_{*e,i}$ of order one that ensure K^{nc} is valid in all neoclassical collisional regimes. The collisionality parameters (ratio of trapped particle bounce frequency to collision frequency) are defined by

$$\nu_{*e,i} = \frac{\sqrt{2}rB}{B_\theta v_{te,i} \tau_{e,i} \epsilon^{3/2}} \tag{3.13}$$

There is no agreed theory for anomalous conduction so Turner and Wesson were motivated to choose the simplest empirical scaling consistent with experiment of K_e^{an}= constant. Other transport codes have often used a temperature dependence for K_e^{an} (eg. T_e^{-1} [26,28]; $T_e^{-3/4}$ [29]), but in TRID the choice [9] of constant thermal conductivity is also made. In section 5.5 the effect of a radially varying thermal conductivity is examined.

Radial transport in the presence of magnetic islands is now considered. Magnetic field lines near the separatrix connect plasma regions lying on opposite sides of the island. The radial flux through an island is thus determined, not by the perpendicular conductivity but by the much higher longitudinal conductivity. Typical classical values in a tokamak imply $K_{e\|} > 10^{12} K_{e\perp}$, for example, so the temperature would be expected to be equalised across an island extremely rapidly. This is implemented in TRID by defining the transport coefficients to be the sum of the background already defined, and a large enhancement between the island boundaries, so that:

$$K_e = K_e(r)\left[1 + K_1\left[1 - \left[\frac{r-r_c}{h}\right]^2\right]^{\alpha_1}\right] , \qquad \text{for } r_c - h < r < r_c + h \tag{3.14}$$

$$\text{where} \qquad r_c = r_s + \frac{1}{4} h^2 s \tag{3.15}$$

An identical expression holds for $K_i(r)$. If K_1 is made much greater than unity then profiles are flattened and the particular functional form for the enhancement will not be important; this is illustrated in section (5.4) with various choices for α_1. It will be set equal to 1 in subsequent chapters. To complete this set of transport equations the growth rate of each island is given by eq.(2.67), i.e.

$$\frac{dh}{dt} = 1.66\frac{\eta(r_s)}{\mu_0}\left[\frac{1}{2}\Delta(h) - \alpha_j h\right] \qquad (3.16)$$

3.5 *Boundary Conditions, Dimensionless Forms, Initialisation*

At $r=0$ the usual boundary conditions for odd and even functions hold, ie $B_\theta = 0$, $T_e' = T_i' = 0$. At the plasma edge a limiter is assumed to be present at $r=a$ followed by a highly resistive, cold, zero current region between $a<r<b$, where b is the radius of a perfectly conducting wall. The edge temperatures are fixed to constant, small values:

$$\begin{aligned} T_e(a,t) &= T_e(a,0) = 5eV \\ T_i(a,t) &= T_i(a,0) = 5eV \end{aligned} \qquad (3.17)$$

The total current (proportional to $1/q_a$) is taken to be either constant and fixed in time or else programmed in time according with a linear current ramp:

$$B_\theta(a,t) = B_\theta(a,0)(1+t/t_d) \qquad (3.18)$$

At $r=0$ and in the region $a<r<b$, $j_z = 0$, so the solution of eq.(2.51) is just

$$\psi_1 = C_1 r^m + C_2 r^{-m} \qquad (3.19)$$

where C_1 and C_2 are constants. At the conducting wall $\psi_1(b)$ must be zero so the boundary condition on ψ_1 at the limiter becomes (dropping the 1 subscript for ψ_1)

$$\frac{\psi_a'}{\psi_a} = -\frac{a}{m}\left[\frac{1 - \left[\frac{a}{b}\right]^{2m}}{1 + \left[\frac{a}{b}\right]^{2m}}\right] \qquad (3.20)$$

and it is easy to show that the condition on ψ at $r=0$ becomes

$$\psi = r\psi'/m \text{ as } r\to 0 \tag{3.21}$$

Before describing the solution of the transport problem a set of dimensionless variables and constants is introduced and all equations converted to dimensionless form. Any variable X has an associated dimensionless variable $\tilde{X}$ and normalisation X_0 where $\tilde{X}= X/X_0$ (note that if T_0 is measured in eV then $kT=\tilde{T} \times eT_0$). Therefore one can define the dimensionless variables:

$$\tilde{r}= r/a, \quad \tilde{t}= t/t_0, \quad \tilde{n}_e= n_e/n_D, \quad \tilde{n}_i= n_i/n_D, \quad \tilde{T}_e= T_e/T_0, \quad \tilde{T}_i= T_i/T_0, \quad \tilde{B}= B_\theta/B_0,$$

$$\tilde{j}= j_z/j_0, \quad \tilde{K}_e= K_e/K_0, \quad \tilde{K}_i= K_i/K_0, \quad \tilde{\eta}= \eta/\eta_0, \quad \tilde{P}= P/P_0, \quad \tilde{H}_e= H_e/P_0,$$

and if the following dimensionless constants are defined,

$$c_1= \frac{B_0^2}{\mu_0 n_D e T_0}, \qquad c_2= \frac{6\mu_0 n_D e^2 a^2}{m_i}, \qquad c_3= \frac{P_0 t_0}{n_D e T_0},$$

then substitution into the transport equations gives the basic equations for TRID (the tilde notation is now omitted for simplicity):

$$\frac{3}{2}\frac{\partial}{\partial t} n_e T_e = c_1 \eta j^2 + \frac{1}{r}\frac{\partial}{\partial r} rK_e \frac{\partial T_e}{\partial r} - c_2 n_e^2 \eta \left[T_e - T_i\right] + c_3 H_e - c_3 P \tag{3.22}$$

$$\frac{3}{2}\frac{\partial}{\partial t} n_i T_i = \frac{1}{r}\frac{\partial}{\partial r} rK_i \frac{\partial T_i}{\partial r} + c_2 n_e^2 \eta \left[T_e - T_i\right] + c_3 H_i \tag{3.23}$$

$$\frac{\partial B}{\partial t} = \frac{\partial}{\partial r}\left[\frac{\eta}{r}\frac{\partial}{\partial r}(rB)\right] \tag{3.24}$$

$$\eta = A(Z)^{-1} T_e^{-3/2} \tag{3.25}$$

$$\frac{dh}{dt} = 1.66\eta(r_s)\left[\frac{1}{2}\Delta(h) - \alpha_j h\right] \tag{3.26}$$

$$\frac{\partial^2\psi}{\partial r^2} + \frac{1}{r}\frac{\partial\psi}{\partial r} - \left[\frac{m^2}{r^2} + \frac{j'}{B(1 - \frac{n}{m}q)}\right]\psi = 0 \tag{3.27}$$

where $\eta_0= 5.2\times10^{-5}\ln\Lambda\ T_0^{-3/2}$, $t_0= \mu_0 a^2/\eta_0$, $B_0= aB_z/Rq_a(t=0)$, $j_0= B_0/\mu_0 a$, $K_0= n_D a^2/t_0$, and h is the island half-width defined in eq.(2.21).

TRID is initialized with a given safety factor profile which equals q_0 on axis, and q_a at the limiter:

$$q(r) = q_0[1 + [Q^{\beta_1}-1]r^{2\beta_1+\beta_2}]^{1/\beta_1} \quad , \quad Q \equiv q_a/q_0 \tag{3.28}$$

which also defines $B_\theta(r)$ and $j_z(r)$. The profiles are then a function of four parameters: the value of q at the axis and limiter, and two shape parameters β_1 and β_2. If $\beta_2 = 0$ then this parametrization becomes equivalent to that of [31]. The increased complexity here allows the temperature to be specified in a consistent way. At $t=0$, $T_i(r) = T_e(r)$ is assumed, no impurities are present so $Z_{eff}(r) = 1$, and the deuterium density profile is taken to be Gaussian with centre and edge densities typically $n_i(0) = 2n_D$, and $n_i(a) = 0.05n_D$:

$$n_i(r) = n_i(0) + (n_i(0)-n_i(a))\left[\frac{e^{-\sigma r^2} - e^{-\sigma}}{1 - e^{-\sigma}}\right] \tag{3.29}$$

In the limit of σ tending to zero, $n_i(r)$ has a simple quadratic dependence. The requirement of some specified average density n_D implies

$$\int_0^1 n_i(r) r dr = \frac{1}{2} \tag{3.30}$$

and allows a simple numerical solution for σ. To proceed further note that at equilibrium $\partial/\partial t = 0$, so Faradays law implies E_z is uniform, and from eq.(3.25) for η

$$T_e(r) = T_{e0}(j_z(r)/j_z(0))^{2/3} \tag{3.31}$$

$j_z(a)$ is evaluated from (3.31) and substituted into (3.28) to obtain a relation for β_2 in terms of β_1, T_{e0}, T_{ea}, q(0), and q(a) which completes the initialisation:

$$\beta_2 = 2\beta_1\left[\frac{1-(T_{ea}/T_{e0})^{3/2}Q}{1-Q^{-\beta_1}} - 1\right] \tag{3.32}$$

3.6 *Difference Scheme*

Given some unknown u(r,t) and it's value u^0 at $t=0$ the solution to

$$\frac{\partial u}{\partial t} = Lu \tag{3.33}$$

is required, where L is a nonlinear operator [32]. The difference scheme used is second order accurate in space and can be either fully or partially implicit. Since the equations are nonlinear it is necessary to iterate towards a solution at each timestep. Equation (3.33) becomes

$$u_i^{p+1} = u_i^n + \Phi\Delta t L u_i^{p+1} + (1-\Phi)\Delta t L u_i^n \tag{3.34}$$

u_ℓ^{p+1} is the (p+1)th iteration to u at mesh point i and timestep n+1, and Φ a measure of the implicitness. A nonlinear term such as $K_\ell^{p+1}\partial T_\ell^{p+1}/\partial r$ is linearized, replacing K_ℓ^{p+1} by it's value K_ℓ^p at the previous iteration. The equations for T_ℓ^{p+1} and T_i^{p+1} are coupled only through the equipartition term but serious numerical oscillation occurs if attempts are made to separate their solution. Therefore they are solved for simultaneously using the new T_ℓ^{p+1} to update resistivity. The poloidal field diffusion is then solved and finally all transport coefficients are updated before repeating the iteration cycle.

As an example of the difference scheme consider (3.22). The mesh spacing Δ is constant throughout so $r_i = i\Delta$ for i = 0..N, three-point centred differences are used, and defining $\nu_i \equiv \Phi\Delta t/(r_i\Delta^2)$ and $\mu_i \equiv (1-\Phi)\Delta t/(r_i\Delta^2)$, then:

$$\begin{aligned}
&T_{ei-1}^{p+1}\left[-\nu_i r_{i-\frac{1}{2}} K_{ei-\frac{1}{2}}^p\right] + T_{ei}^{p+1}\left[\tfrac{3}{2}n_{ei} + \nu_i\left(r_{i-\frac{1}{2}}K_{ei-\frac{1}{2}}^p + r_{i-\frac{1}{2}}K_{ei-\frac{1}{2}}^p\right) + \Phi\Delta t c_2 n_{ei}^2 \eta_i^p\right] + \\
&T_{ei+1}^{p+1}\left[-\nu_i r_{i-\frac{1}{2}} K_{ei-\frac{1}{2}}^p\right] + T_{ii}^{p+1}\left[-\Phi\Delta t c_2 n_{ei}^2 \eta_i^p\right] = \Phi\Delta t c_1 \eta_i^p \left[j_i^p\right]^2 + \\
&(1-\Phi)\Delta t c_1 \eta_i^n \left[j_i^n\right]^2 + \Phi\Delta t c_3\left[H_{ei}^p + P\left[T_{ei}^p\right]\right] + (1-\Phi)\Delta t c_3\left[H_{ei}^n + P\left[T_{ei}^n\right]\right] \\
&+ T_{ei-1}^n\left[\mu_i r_{i-\frac{1}{2}} K_{ei-\frac{1}{2}}^n\right] + T_{ei}^n\left[\tfrac{3}{2}n_{ei} - \mu_i\left(r_{i-\frac{1}{2}}K_{ei-\frac{1}{2}}^n + r_{i-\frac{1}{2}}K_{ei-\frac{1}{2}}^n\right) - (1-\Phi)\Delta t c_2 n_{ei}^2 \eta_i^n\right] \\
&+ T_{ei+1}^n\left[\mu_i r_{i-\frac{1}{2}} K_{ei-\frac{1}{2}}^n\right] + T_{ii}^n\left[(1-\Phi)\Delta t c_2 n_{ei}^2 \eta_i^n\right]
\end{aligned} \tag{3.35}$$

The differenced equations for T_e and T_i written in matrix form are

$$u_i = \begin{bmatrix} T_e \\ T_i \end{bmatrix}_i$$

$$A_i^p\, u_{i-1}^{p+1} + B_i^p\, u_i^{p+1} + C_i^p\, u_{i+1}^{p+1} = w_i^p \tag{3.36}$$

where w is a 2–vector and A, B, and C are 2×2 matrices, some of whose elements are found in eq.(3.35). An equation identical in form to eq.(3.36) results for B_θ but the matrices now become simple numerical coefficients. Equation (3.36) is solved using a simple recursive method to invert a block tridiagonal matrix; this is described in Appendix B.

When the implicitness parameter Φ equals 1/2 the differencing becomes the Crank–Nicholson scheme, which is second order accurate in time and is always stable for equations with one independent variable and any choice of timestep. However this does not guarantee numerical stability for the iteration over the three varibles in this work. Whitfield [33] has performed a local stability analysis for a similar set of equations and not surprisingly finds $\frac{1}{2} \leqslant \Phi \leqslant 1$ for stability. Tests of the method here have been carried out with no radiation or heating for various choices of Φ and Δt. For Φ close to $\frac{1}{2}$, serious oscillations during iteration, and non–convergence are observed, unless Δt is restricted to unnecessarily small values. For Φ close to 1 the solution is much better behaved and good agreement is obtained between runs with typical $\Delta t = 10^{-3}\tau_R$ and a tenth of this. The choice $\Phi = 1$ is therefore made in TRID, and Δt is taken to be of order $10^{-3}\tau_R$ which typically corresponds to $\Delta t = 1$ms for DITE parameters, and $\Delta t = 40$ms for JET. In fact the presence of strong radiation imposes strict limits on Δt. If an error e^p exists in the pth iteration then linearizing eq.(3.34), one obtains for the amplification factor

$$\frac{e^{p+1}}{e^p} = \Phi \Delta t \frac{\partial}{\partial u}\left[Lu\right]_t^p \qquad (3.37)$$

For stability $|e^{p+1}/e^p| < 1$, so for the particular case of the electron energy equation and considering just the radiation term, eq.(3.37) reduces to

$$\Delta t < \Delta t_{rad} = \frac{n_e}{\Phi c_3 \frac{\partial P}{\partial T_e}} \qquad \text{for all } 0<r<1 \qquad (3.38)$$

This limit can be very low for a strongly radiating plasma. Having ensured stability the timestep is additionally restricted to give a certain accuracy in the solutions:

$$\Delta t^{n+1} \leqslant \Delta t^n \; 0.05 \; \text{Min}[0.5(T_i^{n+1}+T_i^n)/(T_i^{n+1}-T_i^n)] \quad 0<i<N \qquad (3.39)$$

3.7 *Solution of the Stability Equation*

The thermal conductivity depends sensitively on islands widths, which must be obtained for each mode from solving (3.27). At the resonant surface r_s where $q=m/n$ this equation is singular so requires special considerations. Furth et al [34] are followed here. First substitute $r=r_s+x$ and perform Taylor expansions for B_θ, q and j':

$$\frac{d^2\psi}{dx^2} + \frac{1}{r_s}\left[1 - \frac{x}{r_s} + ..\right]\frac{d\psi}{dx} - \left[\frac{m^2}{r_s^2}\left[1 - \frac{2x}{r_s} + ..\right] + \frac{1}{x}\left[c_1 + c_2 + ..\right]\right]\psi = 0 \qquad (3.40)$$

Now defining $y=x/r_s$ and keeping leading terms this reduces to

$$\frac{d^2\psi}{dy^2} + \frac{d\psi}{dy} - \left[\frac{k_1}{y} + k_2\right]\psi = 0 \qquad (3.41)$$

where k_1 and k_2 are constants depending on values at r_s:

$$k_1 = \frac{-r_s\, j_s'\, q_s}{B_{\theta s} q_s'} \qquad (3.42)$$

$$k_2 = m^2 + k_1 r_s\left[\frac{j_s''}{j_s'} - \frac{B_{\theta s}'}{B_{\theta s}} - \frac{q_s''}{2q_s'}\right] \qquad (3.43)$$

If a formal solution of eq.(3.41) is assumed to be

$$\psi = \sum_{n=0} a_n y^{\alpha+n} \qquad (3.44)$$

then only one independent solution can be found (ie. roots of indicial equation differ by an integer). Therefore assume eq.(3.41) has solution

$$\psi(y) = u(y) + v(y)\ln|y|$$
$$u(y) = \sum_{n=0} a_n y^{\alpha+n} \qquad v(y) = \sum_{n=0} b_n y^{\beta+n} \qquad (3.45)$$

and making the substitution one finds:

$$\psi(y) = A_1\Phi_1(y) + \Phi_1(y)k_1\ln|y| + \Phi_2(y) \,, \quad y<0$$
$$\psi(y) = A_2\Phi_1(y) + \Phi_1(y)k_1\ln|y| + \Phi_2(y) \,, \quad y>0 \qquad (3.46)$$

where

$$\Phi_1 = y + \frac{1}{2}[k_1-1]y^2 + \ldots \qquad \Phi_2 = 1 + y^2\left[\frac{1}{2}k_2 - \frac{1}{2}k_1 - \frac{3}{4}k_1[k_1-1]\right] + \ldots$$

Use has been made here of the fact that ψ must be continuous at y= 0, and all that is required of ψ in evaluating $\Delta(h)$ is it's relative magnitude. This allows $\psi(r_s)$ to be set to one in eq.(3.46). Furth et al. neglected the k_2 and $d\psi/dy$ terms in eq.(3.41) and so their solution for ψ is incorrect. However the differences between their solution and eq.(3.46) first appear in terms of order y^2, and so for small y they are not significantly different.

A shooting method is used to determine the correct values for A_1 and A_2 that match the solution of (3.27) to the boundary conditions. The boundary condition (3.20) is converted into a function f of A_2 that for correct choice of A_2 will be equal to zero.

$$f(A_2) = \psi(A_2,a) + \left[\frac{1 - \left[\frac{a}{b}\right]^{2m}}{1 + \left[\frac{a}{b}\right]^{2m}}\right]\left[\frac{\psi(A_2,a) - \psi(A_2,a-\Delta)}{m\Delta}\right] \qquad (3.47)$$

Matching to the boundary conditions is then equivalent to finding the roots of $f(A_2)= 0$ and $\psi'(A_1, r= 0)= 0$ and for this the NAG Library routines [35] are fast and suitable.

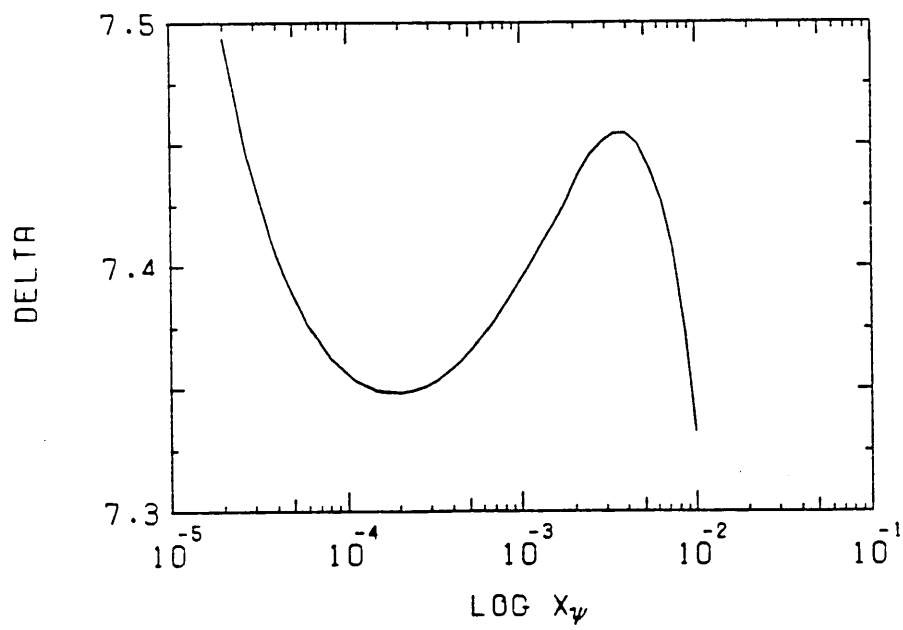

Figure 3.1 Graph of $\Delta(h=0)$ against x_ψ.

The initial values of ψ and ψ' close to r_s are calculated from the series solution (3.46) and depend on A_1 and A_2. The point of fitting is at values of y sufficiently small for (3.41) to be valid but not so small that the singularity causes difficulties.Figure 3.1 is a graph of $\Delta(h=0)$ for a typical DITE profile versus x_ψ on a logarithimic scale, where x_ψ is the distance from the singular surface. For $x_\psi < 2\times10^{-4}$ A_1 and A_2 become larger, it takes longer to find them and $\Delta(h=0)$ diverges as the singularity is approached. For large $x_\psi \geq 10^{-2}$ eq.(3.41) no longer holds, and for x_ψ within this range Δ varies slightly between 7.35 and 7.45. The choice $x_\psi = 2\times10^{-4}$ is used in all TRID simulations. From these two starting values for ψ and ψ', the stability equation is integrated from r_s to the centre and edge using a 4th order Runge-Kutta scheme and this gives $f(A_2,a)$ and $\psi(A_1,0)$.

Once ψ' is known the island width is advanced a timestep according to (3.26) which becomes, when differenced

$$h^{n+1} = h^n + 1.66\Delta t\left[\theta\eta_s^{p+1}\left[\Delta(h)^{n+1} - \alpha_j^{n+1}h^{n+1}\right] + (1-\theta)\eta_s^n\left[\Delta(h)^n - \alpha_j^n h^n\right]\right]$$
$$(1-\theta)\eta_s^n\left[\Delta(h)^n - \alpha_j^n h^n\right]\Big] \qquad (3.48)$$

In this instance $\theta = \frac{1}{2}$ is taken to preserve second order accuracy for h. An iterative method for solving eq.(3.48) failed, as h^{n+1} would fail to converge to a single value but would oscillate between two. Therefore h^{n+1} is found at each at each timestep by numerically solving for the roots of the equivalent nonlinear equation to eq.(3.48). Implicit in each evaluation for $\Delta(h)^{n+1}$ is an iteration scheme for s (upon which α_j depends), because the edges of the islands, r_1 and r_2, at which ψ' is to be evaluated also depend on s:

$$\begin{aligned} s &= \tfrac{1}{2}[\psi'(r_2) + \psi'(r_1)] \\ &= \tfrac{1}{2}[\psi'(r_s + h(1+\tfrac{1}{4}sh)) + \psi'(r_s - h(1+\tfrac{1}{4}sh))] \end{aligned} \qquad (3.49)$$

The effect of s on the island edges r_1 and r_2 is second order in h so rapidly converges after a few iterations. When r_2 exceeds a, eq.(3.31) provides $\psi'(r_2)$ in terms of $\psi'(a)$:

$$\psi'(r_2) = \psi'_a\left[\frac{x_2}{a}\right]^{m-1}\left[\frac{1 + \left[\frac{b}{r_2}\right]^{2m}}{1 + \left[\frac{b}{a}\right]^{2m}}\right] \qquad (3.50)$$

Turner and Wesson [9] set $\psi'(r_2)$ to $\psi'(a)$, so for example with $m=2$, $b/a=\infty$ and

$r_2/a = 1.05$, this corresponds to an underestimation of $|\psi'(r_2)|$ by 5%, which in turn implies an overestimation of Δ. Once the island intersects the limiter TRID predicts a slightly slower growth rate than [9].

The steps taken to obtain a solution for time t^{n+1} given a solution at t^n are summarised in figure 3.2. The calculation can be conveniently separated into two halves: (i) calculation of energy and field profiles for given island width and, (ii) calculation of new island widths. This differs from what is described in eq.(3.35) as the matrix elements multiplying $T\underline{p}^{+1}$ and $T\underline{p}^{+1}$ In (3.35) depend on K^p and hence h^p. Each iteration for T^{p+1} should involve a revaluation of h^p, but this can be a long and time consuming process, especially if many modes are considered. Therefore comparisons have been made with simulations with one h evaluation per timestep, and with simulations where several evaluations were made. The differences in island size are a few percent, while the saturated widths are of course independent of the number of h evaluations. At the completion of a timestep the conservation of energy can be checked. The total energy is not a variable in TRID so this check provides a good guide to the behaviour of the numerical scheme.

In figure 3.2 there are many facilities for adjusting the timestep, which is confined to a preselected range, typically $(0.01\Delta t_{max}, \Delta t_{max})$. Δt is reduced if,
(i) the radiated power losses are large,
(ii) the field and energy solutions haven't converged after a specified number of iterations,
(iii) the change in solution over a timestep exceeds the accuracy requirement and,
(iv) the change in h exceeds Δh_{max} (typically 0.02a).
If $\Delta t < \Delta t_{min}$ then the run is terminated. The run is also terminated if the conditions for a disruption as described in chapter 4 are met.

3.8 *Low Current Equilibria*

This section presents the results of running TRID from some initialisation to a steady state in which saturated islands are present. "Low-current" means the value of q_a is chosen sufficiently high to ensure that q always remains above one everywhere so that the m=1 mode nevers occurs. This situation is described in the next chapter. Table 3.1 contains all the initial plasma parameters, which will be the default values chosen, unless otherwise stated. The machine dependent parameters are for either the DITE [36], or JET [6] experiments.

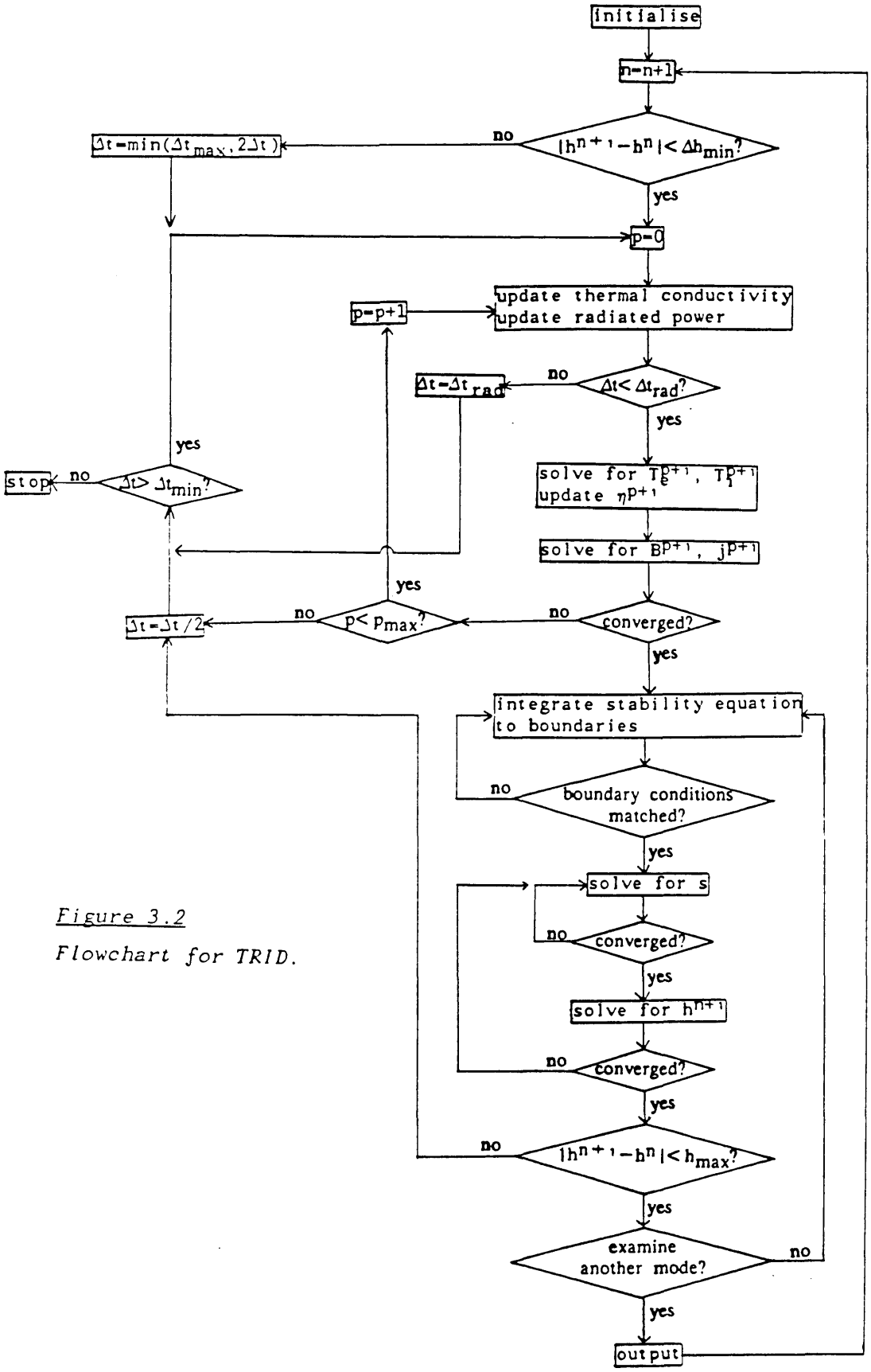

Figure 3.2

Flowchart for TRID.

Table 3.1 Initial data for TRID code

Background electron thermal conductivity	K_e	$5\times10^{19}m^{-1}s^{-1}$	
Enhancement of K	K_1	100	
Shape of enhancement	α_1	1	
Average deuterium density	n_D	$3\times10^{19}m^{-3}$	
Edge density	$n_i(0)$	$0.05n_D$	
Central density	$n_{i(a)}$	$2.0n_D$	
Edge temperature	T_{ea}, T_{ia}	5eV	
Effective charge	Z_{eff}	1.0	
Conducting wall radius	b	∞	
Initial profile factor	β_1	1	
		DITE	JET
Major radius	R	1.17m	3.0m
Minor radius	a	0.26m	1.2m
Toroidal magnetic field	B_Z	1.34T	3.0T

Figure 3.3 has been produced by TRID simulation of DITE with initialisation $T_{e0}=350eV$, $q_a=4.5$, and $q(0)=1.4$. In figure 3.3(a) the positions of the inner and outer edges of the m/n=3/1, 2/1, and 3/2 islands have been plotted as a function of time. The 2/1 island quickly reaches a saturated size of about 0.1a and then remains stable at this size, but gradually shifts inward as the plasma resitively evolves towards equilibrium. However as q(0) increases above 1.5 the resonant surface for the 3/2 mode shifts inwards, and the corresponding island decays and finally disappears. All other modes for this particular case were always stable. It is frequently found sufficient to follow evolution of just these three modes. The increased energy required for the line-bending of higher m modes, as described in section 2.6, is indeed sufficient to either completely stabilise the mode, or else to produce very small islands whose size is negligible in comparison to the 2/1 and 3/2 islands.

Figure 3.3(b) is the energy-checking diagnostic, with $\Delta t=0.5ms$ and number of grid points N=150. The solid line is the change per timestep in the total integrated plasma energy, i.e. $(U^{n+1}-U^n)/\Delta t$, where

$$U^n = \int_0^1 \left[\frac{3}{2}\left[n_e T_e^n + n_i T_i^n\right] + c_1 B_\theta^{2n}/2\right] r dr \qquad (3.51)$$

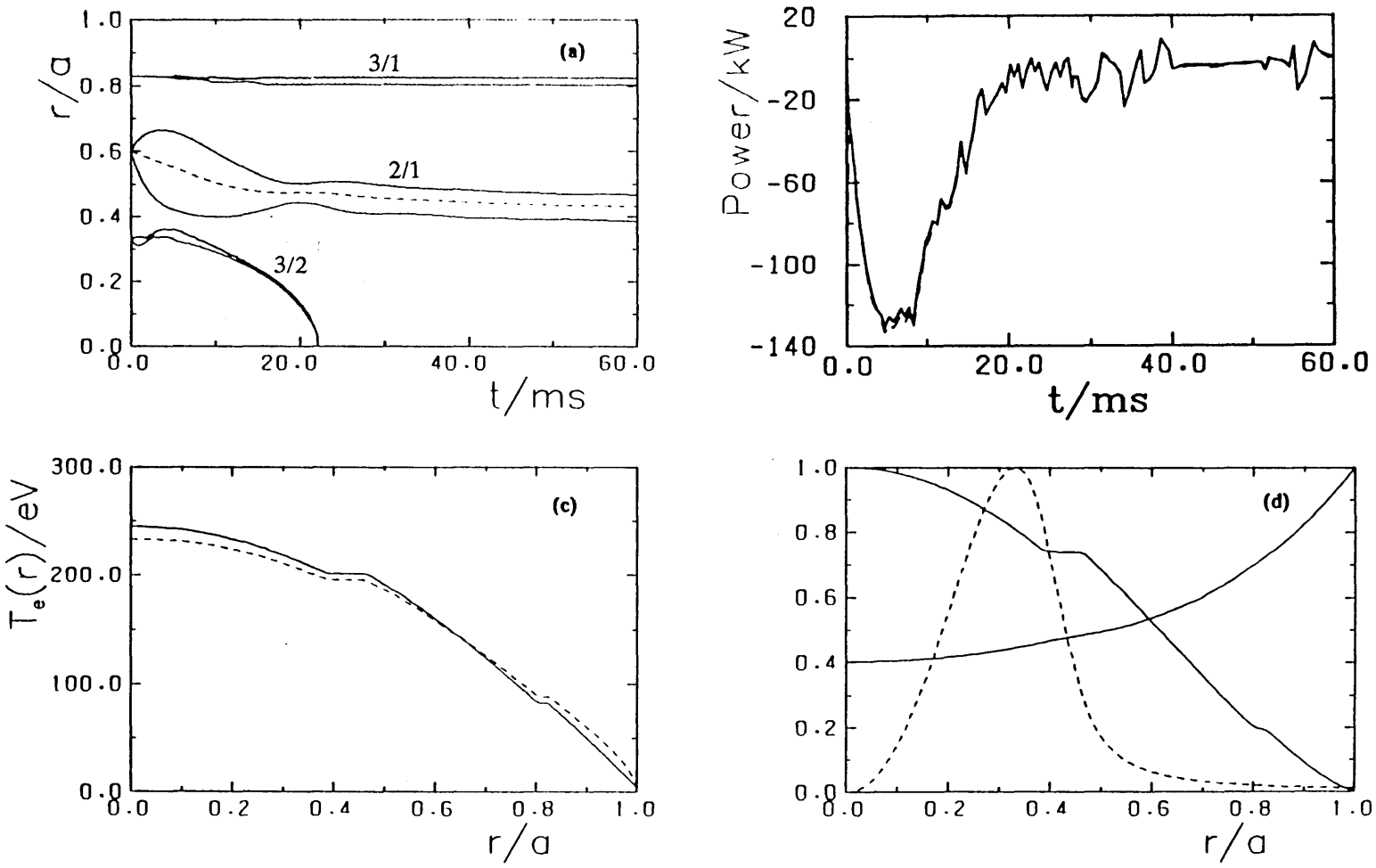

Figure 3.3 ***DITE evolution towards an equilibrium with q_a=4.0. (a) The radial extent of the 3/1, 2/1 and 3/2 islands. (b) The rate of change of total plasma energy (solid line), and the total energy flux into the plasma (dashed line). (c) Radial profiles of the equilibrium (t=60ms) electron temperature (solid line) and ion temperature (dashed line). (d) The equilibrium current density, safety factor, and perturbed helical flux for the 2/1 mode (dashed line).***

and the dotted line the flux S of energy into the plasma which should be equal to eq.(3.51), and is in fact coincident and not easily visible in the figure.

$$S = \left[c_1 E_z B_\theta + K_i \frac{\partial T_i}{\partial r} + K_e \frac{\partial T_e}{\partial r}\right]_{r=1} + \int_0^1 c_3 (H_e + H_i - P) r dr \qquad (3.52)$$

The agreement between the two is such that $(\Delta U - S)/U \leqslant 5 \times 10^{-4}$, with the maximum when islands are largest. A relation such as this can also be used in TRID to impose limits on Δt. Figures 3.3(c) shows the electron temperature and ion temperature (dashed line) at equilibrium, while (d) shows normalised current, safety factor, and the perturbed helical flux for the 2/1 mode (dashed line). The island is visible as a step in the current and temperature profiles.

It was pointed out in [20] how the initialisation chosen affects the transient behaviour of the islands. A particularly unstable example in [20] showed islands covering 37% of the radius soon after beginning the simulation, while the saturated equilibrium contained only one island with width $h_{21} = 0.03a$. Tests are also made with TRID with different initialisations for a JET plasma with $q_a = 4.0$ and $T_e(0) = 1000eV$. Such a study shows which particular characteristics of the current profile lead to strong island growth. The island behaviour is found to be quite insensitive to the initial $T_e(0)$, but initial growth rates depend strongly on q(0) and β_1 in eq.(3.26). Figure 3.4(a) shows contours in $q(0) - \beta_1$ space of j'_{zs}, the current gradient at the $q = 2$ surface, and (b) plots contours of the linear growth rate $\Delta(h = 0)$ of the 2/1 mode. Figures 3.4(c) and (d) show the corresponding current and q profiles at the four corners of (b) where q_0 and β take the following values:

(1): $q_0 = 1.0$, $\beta_1 = 0.0$;

(2): $q_0 = 1.8$, $\beta_1 = 0.0$;

(3): $q_0 = 1.8$, $\beta_1 = 4.0$;

(4): $q_0 = 1.0$, $\beta_1 = 4.0$.

The growth rate varies from $\Delta = 6$ for $q_0 = 1.0$, to $\Delta = 240$ at (3). Maximum instability corresponds to profiles with high q_0 and also very flat q(r) near the axis (β_1 large), which cause r_{s21} to be located in a region of steep current gradient. The transient island behaviour for cases (1) and (3) are compared in figures 3.5(a) and (b) respectively. h_{21} is plotted as a function of time in (c) for all four initialisations. The same saturated width, $h_{21} = 0.045a$, is of course achieved in all four cases, but for (3) it is initially 2.5 times greater than for (1). At lower current, evolution of the plasma from profiles similar to (3) could result in island overlap and interaction with the wall [31,37]. This is an artificial situation as (3), with such strong island growth, is clearly not close to equilibrium, and such profiles would not arise naturally during a discharge,

except possibly with other influences present (eg radiation). Ohmic heating will cause a greater peaking of axial current than in (3), and so current profiles corresponding to (1) and (4) in figure 3.4(c) are more likely. Although (1) and (4) have the same linear growth rate, figure 3.5(c) shows that (4) experiences much less nonlinear stabilization and h_{21} is 60% greater at t= 0.45s. This is due to the initially flat current profile outside the q= 2 surface. Such profiles might be expected with large radiation losses from the edge, so this would be a destabilizing influence (see Chapter 6). TRID simulations are henceforth initialised with profiles closest to equilibrium, e.g. $\beta_1 = 1$ and q(0) close to 1. The dynamics of island growth when q_0 is less than one are examined in the next chapter.

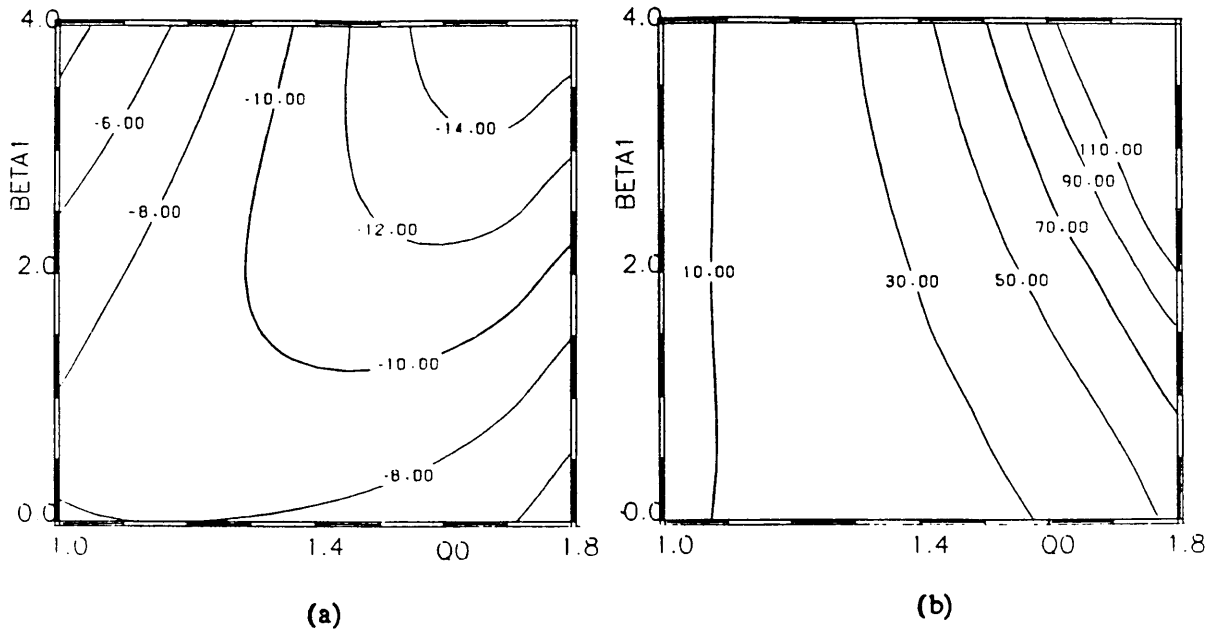

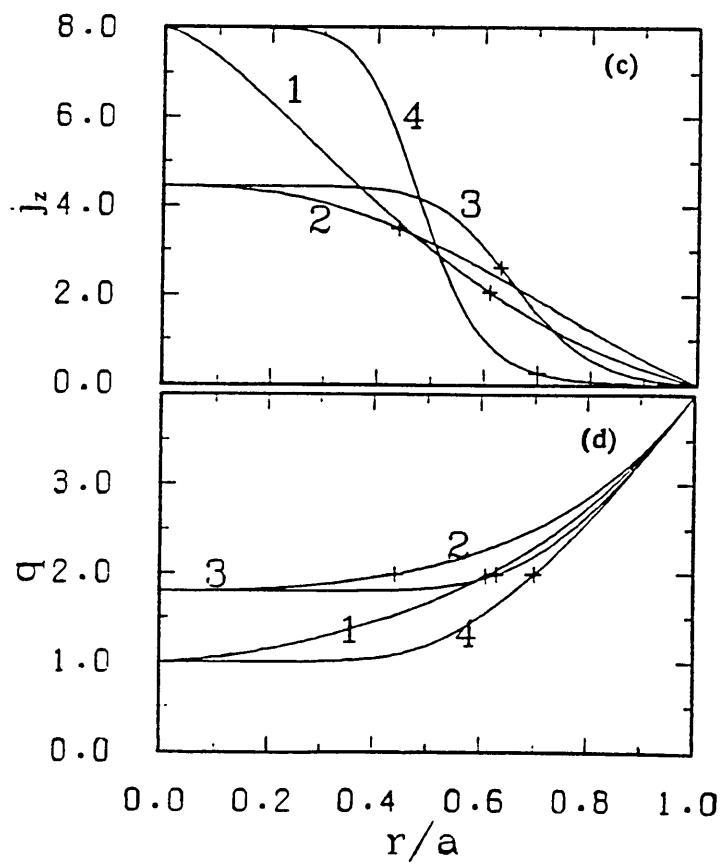

Figure 3.4 (a) Contours of j'_{zs}, the current gradient at the 2/1 resonant surface, as functions of q(0) and profile factor β_1. (b) Contours of initial growth rate $\Delta(h=0)$ for the 2/1 island. (c) The current profiles corresponding to the four corners of (a), i.e. (1): $q_0=1.0$, $\beta_1=0.0$; (2): $q_0=1.8$, $\beta_1=0.0$; (3): $q_0=1.8$, $\beta_1=4.0$ and; (4): $q_0=1.0$, $\beta_1=4.0$. (d) The corresponding safety factor profiles for (c).

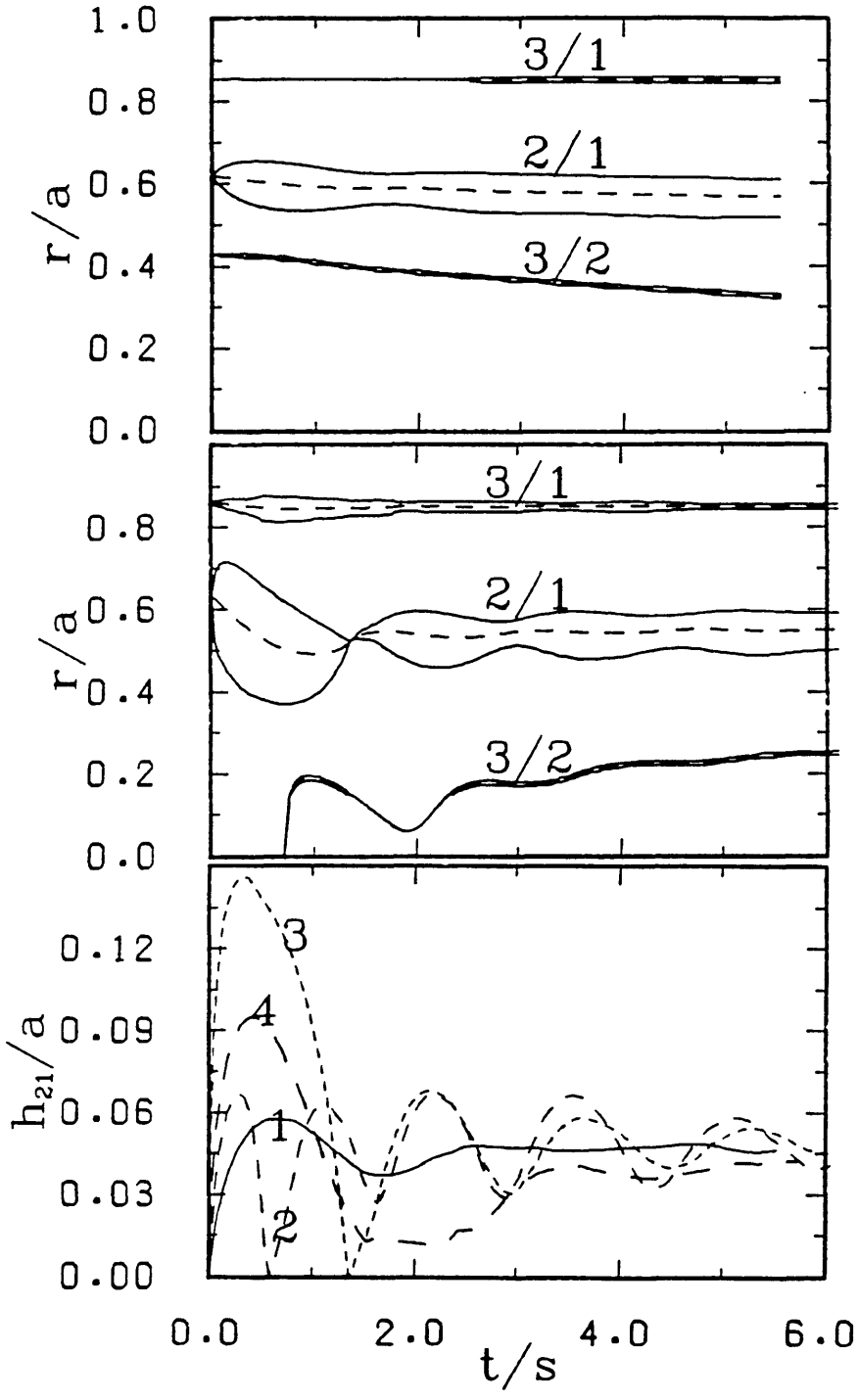

Figure 3.5 The radial extent of the magnetic islands as functions of time, for (a): initialisation (1) of figure 3.4(c) and, (b): initialisation (3). The transient behaviour of the 2/1 island width for all four initialisations is shown in (c).

CHAPTER FOUR

SAWTEETH AND DISRUPTIONS

4.1 *Introduction*

The simulations presented in the previous chapter will not accurately describe tokamak behaviour because the sawtooth oscillations that will occur when q drops below 1 near the axis have been neglected. This chapter presents the experimental observations that characterise sawteeth, and then reviews the Kadomtsev theory that seeks to explain them. In TRID a sawtooth collapse is taken to be triggered by a m=1 resistive mode growing to large size, and the post-collapse fields to be given by the Kadomtsev prescription. Discrepancies between the Kadomtsev theory and more recent sawtooth observations are also noted and new theories for the sawtooth are discussed. It is shown that a time-averaging of the effect of the sawtooth on transport still provides an adequate description. Finally the interaction between the sawtooth and the m=2 island is interpreted as a disruption.

4.2 *Early Experimental Observations*

Sawtooth oscillations in the soft X-ray emission of the ST tokamak were first observed by von Goeler in 1974 [38], and since then a wealth of experimental data shows that they are common to all tokamaks [39]. It can be shown for all tokamaks that the onset of sawtooth activity coincides with the safety factor on axis falling to unity. Features common to the oscillations observed in early small machines, and to oscillations in low-current ohmically heated discharges of larger machines include:

(i) A slow ramp phase during which the temperature and density near the centre increase linearly by about 10% and a few percent respectively.

(ii) A rapidly growing oscillation emerges at the end of the ramp phase and is a precursor to the rapid collapse of temperature that follows. Analysis indicates that the oscillations are consistent with the rotation of an m=1 mode.

(iii) The oscillation ceases when it's amplitude is comparable with the change occuring during the slow rise phase; the temperature and density rapidly collapse, achieving near flat profiles.

In small tokamaks the repetition time τ_S of the sawtooth is 1-5 ms, the collapse

time $\tau_c \leqslant 100$ μs, and the growth rate of the precursor oscillations $\approx 3ms^{-1}$. Figure 4.1(a) shows the precursor oscillations followed by rapid collapse in the line integrated density in a JET discharge [40]. Figure 4.1(b) shows the electron temperature profiles just before, and just after the collapse phase.

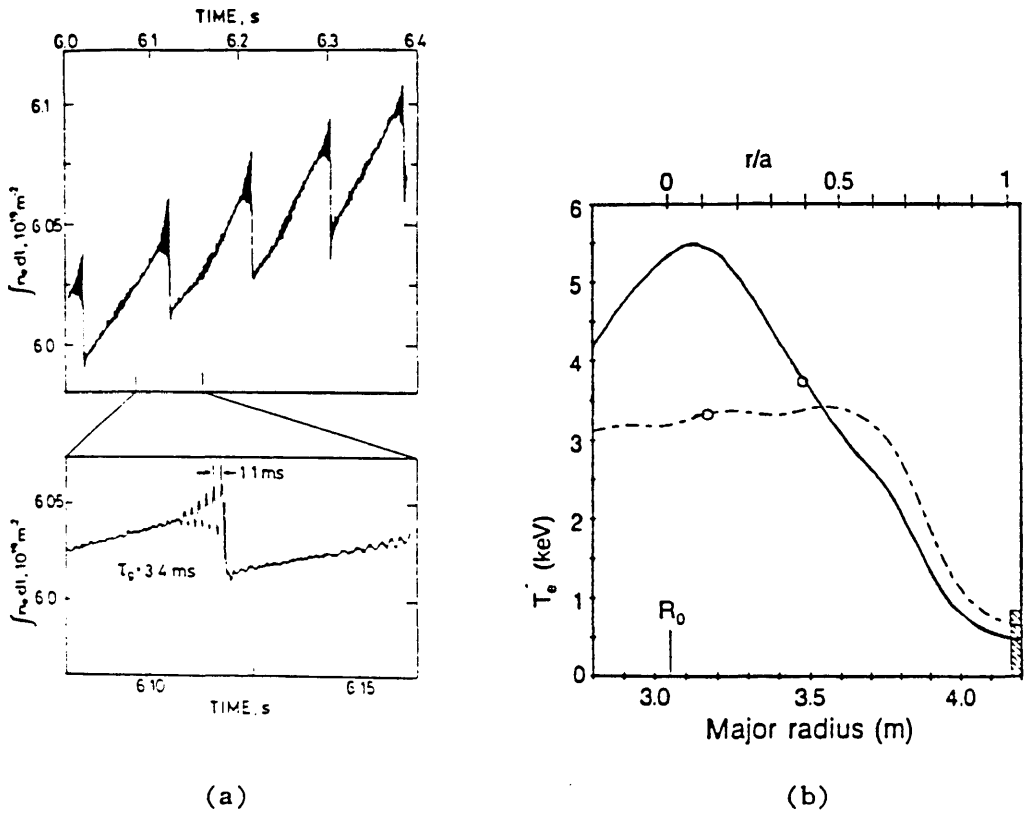

Figure 4.1 (a) Sawtooth oscillations in the line integrated density during the current-ramp phase of an ohmically heated discharge in JET [40]. (b) Peaked and flattened electron temperature profiles prior to, and succeeding a sawtooth collapse in an additionally heated JET plasma [42].

4.3 *The Kadomtsev Model*

The starting point for an explanation was that it appeared it was the m=1 precursor growing to large size that initiated a collapse, but the obvious assumption that it might be an unstable ideal MHD internal kink mode was first discarded. Von Goeler et al [38] showed that it's growth rate was approximately seven times greater than that of the precursor, and furthermore Rosenbluth et al [41] showed in the low beta limit that it should saturate at a much lower amplitude than was observed.

However Kadomtsev [10] observed that further evolution was possible with resistivity present.

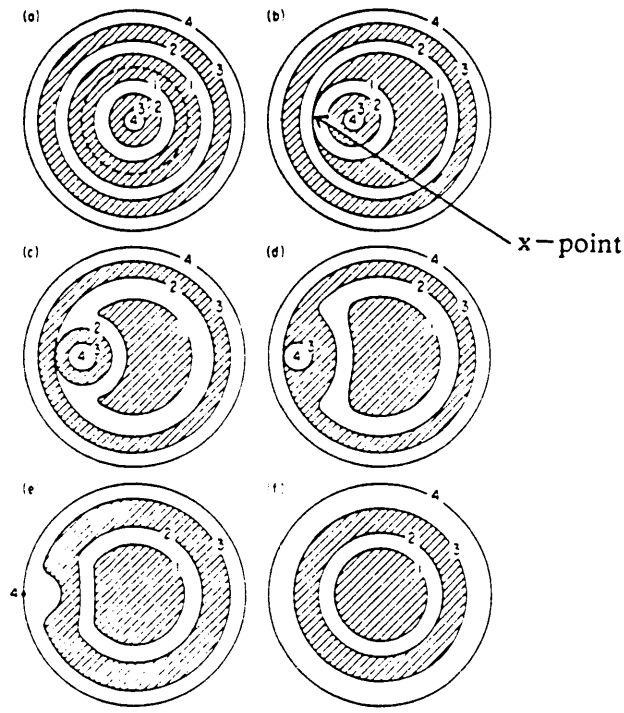

Figure 4.2 Sequence showing the rearrangement of flux contours expected with the Kadomtsev model for reconnection of the m=1 mode. (Taken from White [75]).

His now famous reconnection model for the collapse phase is now briefly reviewed with the aid of figure 4.2. The first figure shows the initial helical flux contours and position of a q= 1 surface dotted in, if a monotonically increasing profile is assumed. At some time an initial small amplitude ideal m= 1 perturbation is triggered. This displaces the central region and reconnection begins at the x–point. The two surfaces labelled 1 with the same ψ connect to form one surface. The subsequent evolution of the flux inside this surface does not involve resistivity so the value of ψ and the toroidal flux inside the surface are conserved. The process occurs with the other surfaces until the o–point is expelled through the x–point and the contours have returned to an axisymmetric state. Figure 4.3 shows the initial and final forms for the helical flux. Given ψ_i just before collapse, the final form ψ_f is obtained from the relations expressing conservation of toroidal flux, and the requirement that reconnection be between regions of equal helical flux, i.e.

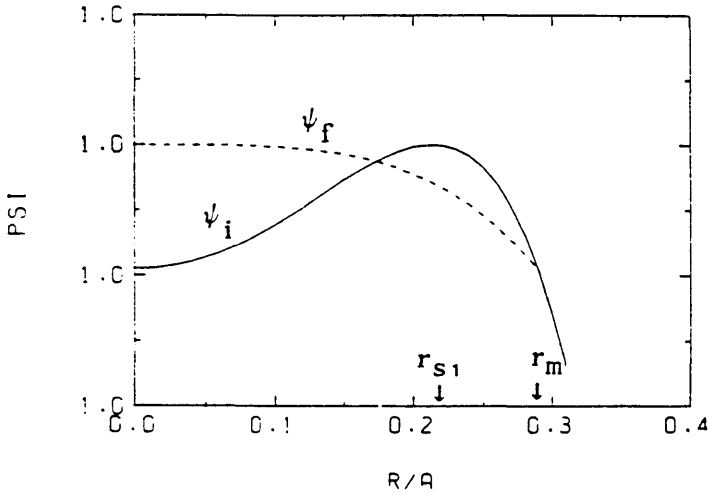

Figure 4.3 *Helical flux ψ_i before sawtooth collapse (solid line), and flux ψ_f after a Kadomtsev reconnection (dotted line).*

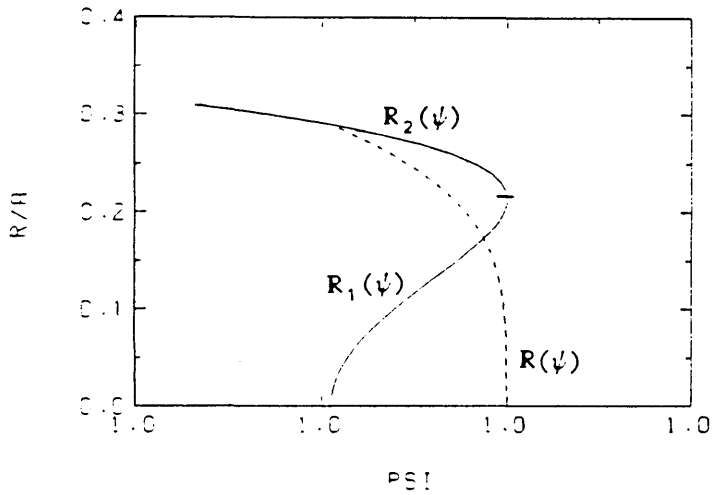

Figure 4.4 *Inverted helical flux before and after collapse. Portions of the curve labelled R_1 and R_2 define terms in equation (4.3).*

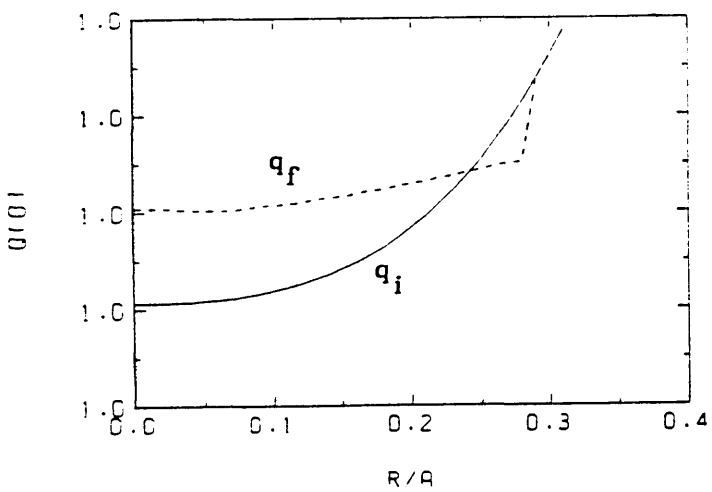

Figure 4.5 *Initial and final safety factor profiles for a Kadomtsev reconnection*

$$r_1 dr_1 + r_2 dr_2 = r dr$$

$$d\psi = \frac{\partial \psi_i}{\partial r}\Big|_{r_1} dr_1 = -\frac{\partial \psi_i}{\partial r}\Big|_{r_2} dr_2 = -\frac{\partial \psi_f}{\partial r}\Big|_{r} dr \qquad (4.1)$$

A more transparent form for the prescription that is used in TRID to obtain figure 4.3, can be seen if it is inverted and $R_1(\psi)$, $R_2(\psi)$ and $R(\psi)$ are defined as being those parts of the curve indicated in figure 4.4. It can be noted that

$$\frac{dR_2}{d\psi} = \left[\frac{\partial \psi_i}{\partial r}\Big|_{r_2}\right]^{-1} \qquad (4.2)$$

and substituting similarily for R_1 and R into eq.(4.1)

$$R^2(\psi) = R_2^2(\psi) - R_1^2(\psi) \qquad (4.3)$$

To find the reconnected profiles in TRID the initial helical flux is inverted, $R(\psi)$ is calculated using eq.(4.3) and then this is inverted to obtain the final helical flux, and consequently $B_\theta(r)$, $q(r)$ and $j_z(r)$. The initial and final profiles for q_f are illustrated in figure 4.5. q_f is now above one everywhere and essentially flattened out to some mixing radius r_m defined by $\psi_i(r_m) = \psi_i(0)$. Outside r_m the profiles are assumed to remain unchanged. Kamdotsev calculates r_m for the special case of a quadratic current profile and finds $r_m = \sqrt{2} r_{s_1}$, but here, with this general computational method for arbitrary transport-determined profiles, r_m is less than this: typically in the range 1.20-1.30 times r_{s_1}.

Simultaneously with the reconnection, all quantities tied to the field lines, such as temperature and impurity ion density, are redistributed, subject to the constraints of conservation of particles and energy. These constraints are insufficient to determine the mixed profiles and additional information is needed. The Kadomtsev model would imply hollow profiles after reconnection but if mixing were turbulent then a flattening of profiles would be expected. Experimentally, flat T_e profiles are frequently reported [42]. 3D numerical simulations of the reduced MHD equations [43,44,45] also produce flat profiles, so therefore TRID also assumes a flattening of T_e and T_i out to $r = r_m$. In this respect TRID is consistent with other transport simulations of sawteeth [46,47]. The small amount of magnetic energy released during reconnection will also additionally heat the electrons, but in practice is small enough to be negligible. Thus:

$$T_{ef} = \frac{\int_0^{r_m} \left[n_e T_{ei} + \frac{1}{2}\left[B_{\theta i}^2 - B_{\theta f}^2 \right] \right] r dr}{\int_0^{r_m} n_e r dr} \qquad (4.4)$$

Once the collapse is completed, stability is restored with $q>1$ everywhere and the plasma enters the ramp phase, relaxing back towards a steady state in which heating and energy losses are balanced. The core of the plasma heats up through ohmic heating and the energy deposited near the mixing radius diffuses away, giving rise to the heat pulse observed. As the central region heats up, so the current on axis is able to increase, allowing q to drop below one and instability to develop again.

The collapse phase of the JET sawtooth oscillation in figure 4.1 takes approximately $100\mu s$, while DITE collapse times are also of comparable duration. The collapse time τ_c can be estimated by [48]

$$\tau_c \approx \left[\frac{r_s^3 \mu_0^{1.5} \rho^{0.5}}{2\eta B_\theta} \right]^{\frac{1}{2}} \qquad (4.5)$$

With the parameters of Table 3.2 and $r_{s_1} = 0.35a$, then for DITE one finds $\tau_c = 97\mu s$, but for JET this increases to $\tau_c = 3.2ms$. The Kadomtsev model therefore gives correct predictions for τ_c for the early, smaller tokamaks, but it fails to explain the rapidity of collapse for plasmas of JET dimensions.

Another problem with the initial formulation of this model is that the trigger for a sawtooth collapse, and hence the sawtooth period, is undefined. After collapse the q profile, which is greater than 1 everywhere must evolve to one in which $q<1$ throughout the region inside r_{s_1} since q is assumed monotonic at collapse. However if it were an ideal mode causing the collapse then instability would be expected as soon as q became equal to one, and not at some much later unspecified time. Numerical simulation by Sykes and Wesson [49] and analytic work by Bussac et al. [50] showed that the $m=1$ ideal mode might be stabilised by toroidal effects, for sufficiently low poloidal beta. They also concluded that even in the large aspect ratio limit that the cylindrical result of ideal instability would not apply. Study therefore turned to the possibility of marginal stability of the ideal mode, and instability due to a resistive mode. Reconnection leading to Kadomtsev-prescribed profiles would not occur during the nonlinear phase of an ideal mode, but would occur continuously during the linear and nonlinear development of an $m=1$ magnetic island. This modification to Kadomtsev's model was proposed by Jahns et al [51] and has the advantage that the

plasma becomes unstable as soon as q drops below one, and not at some arbitrary trigger time.

4.4 *Resistive m=1 Mode*

Coppi et al. [52] derived a dispersion relation for the growth rate of a m=1 internal mode, in which the ideal and resistive modes are just different limits of this dispersion relation. A more complete analysis was made by Waddell et al. [53] that included equilibrium diamagnetic flows and the Hall (or diamagnetic) term in Ohm's law. In the limit of a stable ideal m=1 internal kink, the growth rate of the resistive m=1 tearing mode, modified by diamagnetic drifts is

$$\gamma(\gamma+i\omega_{*i})(\gamma-i\omega_{*e}) = \gamma_T^3 \qquad (4.6)$$

A discussion of the derivation of eq.(4.6), and definition of the various quantities in it, is contained in Appendix D. Waddell et al. [43] in their simulation find that the m=1 mode continues to grow at approximately the linear rate γ, even as it grows to large size. Jahns et al. [51] therefore assumed an m=1 island to grow linearly until collapse so

$$h_1(t) = h_1(0)\ \exp\left(\int_{t_0}^{t} \gamma(t)\ dt\right) \qquad (4.7)$$

and then carry out a Kadomtsev collapse instantaneously when the m=1 island extends to the axis. They additionally assume $\gamma << \omega_{*e,i}$ implying $\gamma = \gamma_T^3/\omega_{*e}\omega_{*i}$, but it is found here that this limit is not applicable, so the full expression eq.(4.6) is used for γ. Both however imply a reduction in growth due to diamagnetic terms. In [43] it is shown that the m=1 precursor does indeed grow at a slower rate than predicted by γ_T alone and so if this theory is to predict the correct repetition time then diamagnetic and finite gyroradius effects cannot be ignored. The initial size of the m=1 island $h_1(t_0)$ is assumed to be the thickness of the tearing width ϵ_1, at time t_0, when q first reaches 1.

Immediately after collapse when profiles are flat, the growth rate which is proportional to the shear squared, will be low but would continously become greater as the profiles steepened. Jahns et al. [51], assuming a linear increase in T_e, and neglecting variation in $\omega_{*e,i}$ and r_{s1}, derive an island growing like:

$$\ln \frac{h_1(t)}{h_1(0)} \approx \frac{1}{\omega_{*e}\omega_{*i}\tau_A^2\tau_R} \int_{t_0}^{t} \left[\alpha_{s0} + \alpha_{s1} t^2\right]^2 dt \qquad (4.8)$$

If α_{s1} dominates then a t^5 dependence will be apparent in (4.8) and $h_1(t)$ will be small for almost all the duration of it's growth. The assumed linear growth should therefore be correct for much of this time and the effect of the m=1 island on the transport and the equilibrium profiles will only be apparent as h_1 rapidly approaches r_{s1} and would take the form of a fast collapse.

Figure 4.6(a) illustrates the position of $r_{s1}(t)$ and $h_1(t)$ over a few sawtooth periods obtained with TRID, for a DITE plasma with q_a= 3.0, Z_{eff}= 2, and no m>1 modes present. Only a single q=1 resonant surface is observed. Figure 4.6(b) shows shows the corresponding electron temperature on axis . Beginning with the initialisation of section 3.5, the sawtooth, after the first few oscillations, settles into a steady pattern with period 4.6ms, and amplitude $\Delta T_e(0)/T_e(0)$= 9%. The ion temperature exhibits identical behaviour. If the simulation is repeated with hydrogen the steady-state sawtooth period is 2.1ms. As γ_T goes as $m_i^{-1/2}$, the period, and also ΔT_e, are less for a hydrogen plasma. Near the end of the ramp phase some saturation of $T_e(0)$ is observed in figure 4.6(b) as thermal conduction starts to become comparable to ohmic heating. This suggests that if TRID is to model truly linear sawteeth then the axial thermal conductivity should be reduced, or that the triggering condition is possibly leading to too large a value for τ_{saw}. Section 4.6 shows that if the zone of instability extends to greater radius then the period and flattening of the ramp are less. It can be concluded that for DITE-like discharges the Kadomtsev model for collapse, triggered by an unstable m=1 magnetic island, seems to provide a good description for the sawtooth, reproducing many of the characteristics observed experimentally. Discrepancies and other models are discussed in section 4.5.

Equation (4.8) derived by [51] implies that $\ln(h_1(t)/h_1(0))$ goes like t^5 for large α_{s1}/α_{s0}, and like t in the opposite limit. This has been examined in figure 4.7 by plotting the log of this quantity against ln(t) for the DITE sawteeth of figure 4.6. At the beginning of each ramp-phase, when ΔT is near linear, the t^5 behaviour is apparent. However the exponent of this power law for γ steadily decreases throughout the ramp, but even just prior to collapse, it's minimum value is about 2.4. The m=1 island therefore remains very small during most of the ramp phase, and so should continue to grow linearly during this time.

If there were any hollowness in the current density during the ramp phase then

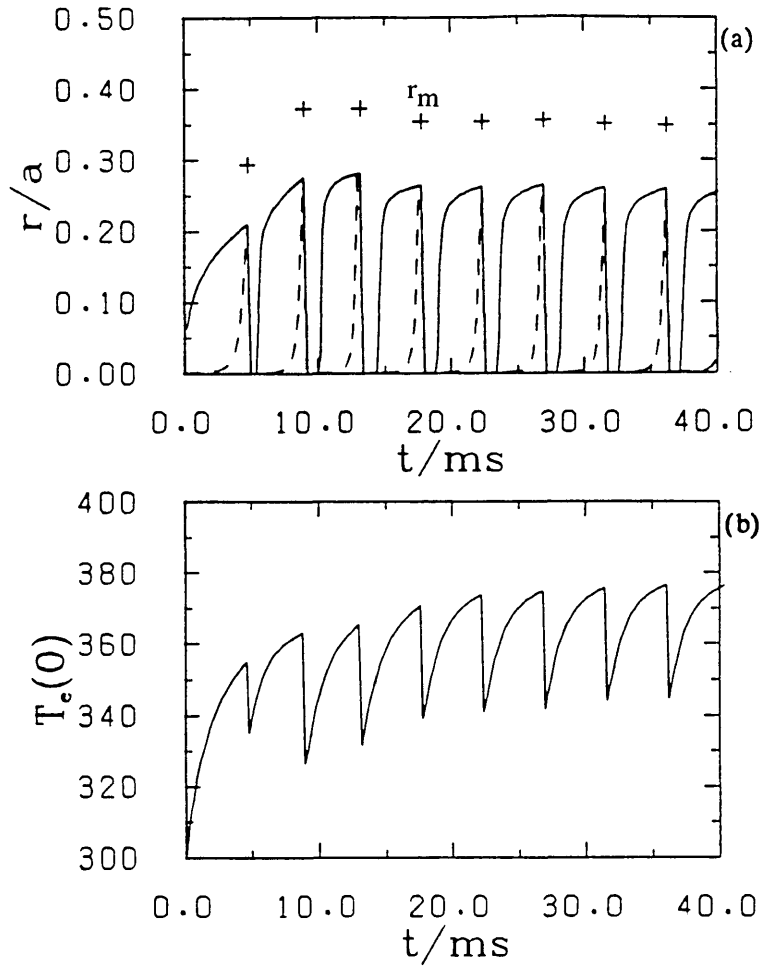

Figure 4.6 (a) Position of the q=1 singular surface (solid line), and size of the m=1 island (dotted line), for a DITE simulation with q_a=2.9 (b) Axial electron temperature variation corresponding to (a).

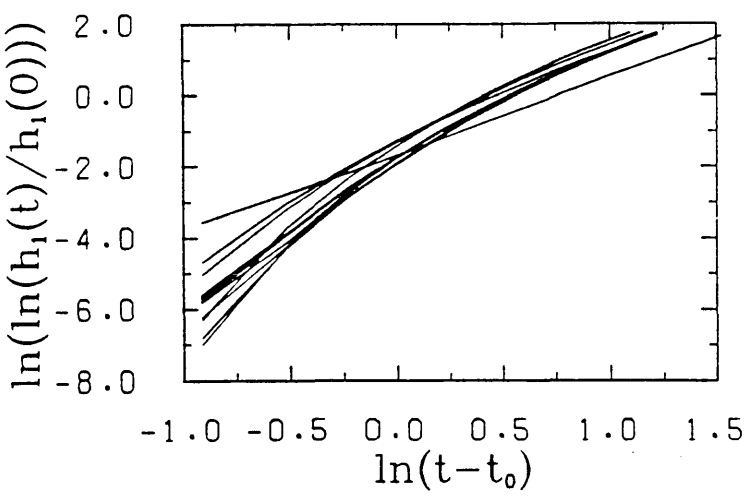

Figure 4.7 Graph of $\ln(\ln(h_1(t)/h_0(t)))$ against $\ln(t)$ for the sawteeth of figure 4.6. Gradient varies during m=1 growth, and changes from being initially between 4 and 5, when ΔT_e is linear, to about 2.4 prior to collapse.

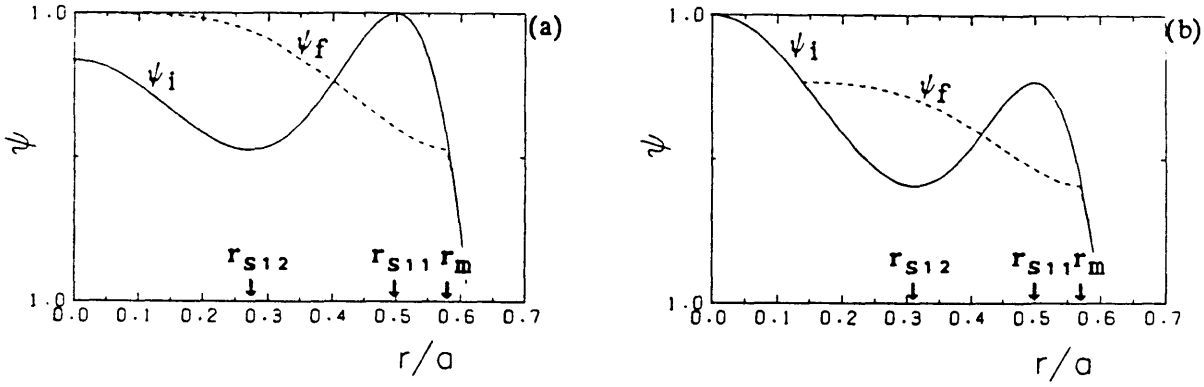

Figure 4.8 *(a) Initial helical flux $\psi_i(r)$ (solid line) for two q=1 resonant surfaces with $\psi_i(0)<\psi_i(r_{s11})$. Dashed line is the reconnected flux $\psi_f(r)$ after a Kadomtsev collapse, triggered when the m=1 island equals r_{s11}. (b) The same profiles as (a) but with $\psi_i(0)>\psi_i(r_{s11})$, in which case the collapse does not extend to the axis.*

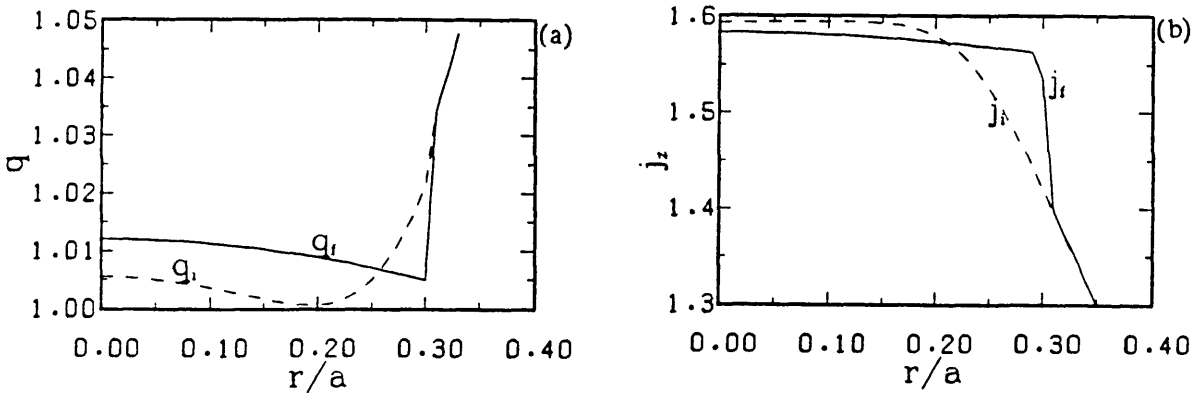

Figure 4.9 *(a) Typical pre- and post-collapse safety factor profiles predicted by the minimum energy state sawtooth model for a JET plasma with r_m=0.3a and q_a=2.9. (b) Corresponding current profiles.*

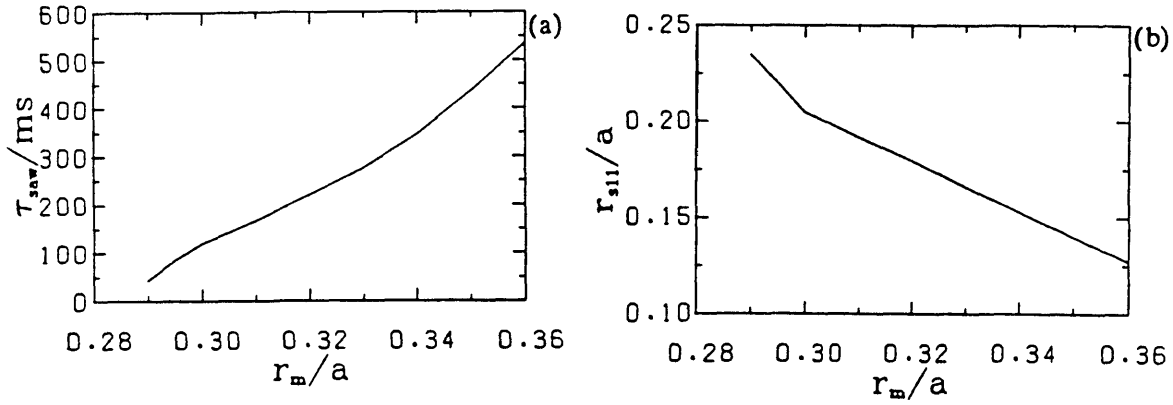

Figure 4.10 *The steady-state minimum energy state sawtooth period (a), and position of the q=1 resonant surface (b), as a function of mixing radius, for a JET discharge with q_a=2.9.*

two q=1 surfaces would be expected and partial reconnection extending only part-way to the axis could occur. Figure 4.8 shows the two possible helical flux profiles for such a current distribution, and the corresponding profiles following collapse. Pfeiffer [54] has adapted the simple Kadomtsev prescription to allow for such a case but used a specified trigger time for collapse. In the TRID simulations a m=1 island is allowed to grow about the outer surface and reconnection is triggered when either:

(i) $\psi(r_{s11})>\psi(0)$ and $h_1=r_{s11}$ (figure 4.8(a)), or;

(ii) $\psi(r_{s11})<\psi(0)$ and $h_1=r_{s11}-r_{s12}$ (figure 4.8(b)).

An m=1 island would also be expected to grow about the inner surface r_{s12} but this lies in a hotter region for a peaked temperature profile, and as the resistive growth $\gamma_T \approx T^{-\frac{1}{2}}$, it's growth rate will be less than the island at larger radii, and so is neglected. In case (ii) reconnection does not disturb the profiles on axis, so collapse of the core temperature is not acheived. The plasma then continues to resistively evolve until the next full or partial reconnection. Pfeiffer [54] has succesfully modelled double-sawtooth oscillations observed in the Doublet III tokamak. In the simulation of figure 4.6 no hollowness is observed, but it is found later that when the m=2 mode is growing, the rapid inward diffusion of current observed can give rise to these sort of profiles.

4.5 *Other Sawtooth Models*

Before applying the sawtooth model just described to a large tokamak some generalexperimental observations of sawtoothing in high current discharges in JET are presented [40] that vary in several respects from those already described in section 4.2.

(i) Part way through the ramp phase a partial collapse is observed that does not disturb the plasma core. Such compound sawtooth are frequent, and seem to be a characteristic of large tokamaks. The partial reconnection model of the previous section could account for this.

(ii) Generally no precursor oscillations precede collapse. Post-collapse successor oscillations with probable m=1 structure are often observed that decay away in ≈10ms.

(iii) "Monster" sawtooth collapses of the temperature profile, with greatly extended period are frequently observed during additionally heated discharges.

These differences, and in particular the lack of a precursor, imply that two different forms of instability are operating in these two regimes. Wesson [55] re-examined the possibility of an ideal mode being responsible. The rapidity of onset of the instability without precursor could possibility be attributed to inertial growth

rates. Reconnection would occur after the collapse phase at the beginning of the ramp phase giving rise to successor oscillations. However Bussac et al [50] showed ideal modes in toroidal geometry would be stable for sufficiently small poloidal beta β_p, whereas in JET sawtooth activity occurs for β_p much less than this critical value. Bussac et al assumed a simple parabolic profile for j_z, which still has significant shear inside the singular surface, so Wesson [55] recalculated the critical β_p with a piecewise definition of j_z with very small shear, consistent with actual experimentally derived shear. He found that the critical β_p tends to zero as q(0) tends to one; this implies ideal instability as soon as q drops below one anywhere within the plasma. However with $1-q< \epsilon$, the rigid shift trial function for the ideal m=1 instability is now no longer valid in minimising the potential energy. Wesson replaced the rigid shift displacement with a convective type flow termed a "quasi-interchange" shift. This appeared to be in agreement with experimental eigenfunctions derived from X-ray emission on JET. However evidence against this form of instability is present in that [56] calculates the switch-on time for the quasi-interchange to be three orders of magnitude slower than required by the experimental evidence. This model may therefore provide many of the answers to sawtoothing in large tokamaks but is not amenable to implementation in our 1D code. The shape of the profiles after collapse is not determined, and a mixing radius for temperature flattening is not well defined, beyond being approximately the radius of the singular surface.

Ward [48] takes a different approach. He assumes that the plasma will become ideally unstable whenever q drops below one anywhere, as shown by Wesson, but no attempt is made to model the specific form of instability. However in [48] it is pointed out that, over the short collapse time of the sawtooth, the total helicity $H \equiv \int A.B dV$ within the collapse region must be essentially constant as it evolves on resistive timescale. Using this constraint of constant helicity, and also using the constancy of the vector potential A on the surface of a closed system, Woltjer [57] had earlier shown that the minimum magnetic energy state of a closed system corresponds to one with a force-free field, i.e.

$$\nabla \times B = \mu B \qquad (4.9)$$

with μ constant and $\nabla p = 0$. The net result of the sawtooth collapse is assumed in [48] to produce such a minimum energy state inside some mixing radius r_m, while outside the profiles are unchanged. Inside r_m the post-collapse profiles are therefore given by eq.(4.9) which becomes Bessel's equation in cylindrical geometry. With the constraints on H and A at $r = r_m$ this can be solved for the post-collapse fields $B_{\theta f}$ and B_{zf},

with all arbitrary constants determined. It is found that

$$B_{zf}(r) = C_m J_0(\mu r) \ , \qquad B_{\theta f}(r) = C_m J_1(\mu r)$$
$$C_m = \mu A_{\theta i}(r_m)/J_1(\mu r_m) \tag{4.10}$$

and the constant μ is found from the iterative solution of $H_i = H_f$;

$$H_i = 4\pi^2 a^2 R \frac{C_m^2 a r_m}{\mu^2}\left[\frac{\mu r_m}{2}\left[J_0^2(\mu r_m) + J_1^2(\mu r_m)\right] - J_0(\mu r_m)J_1(\mu r_m)\right] \tag{4.11}$$

If a state of maximum entropy is also attained then $\nabla T = 0$ [48] and so the post–collapse temperature profiles are also flattened as with the Kadomtsev model. The total magnetic energy is decreased much more than with the Kadomtsev prescription. The toroidal energy is in fact increased here (minimum toroidal magnetic energy corresponds to B_z = constant), but the extra freedom with non–constant B_z allows a much greater relaxation of poloidal energy.

It is possible to implement this collapse in TRID, but as the cylindrical approximation requires B_z constant, the redistribution of B_z and it's resistive evolution is not followed. Figure 4.9 shows typical pre– and post–collapse q and current profiles, with evolution of B_θ only, for a JET plasma with $q_a = 2.9$, no other islands present and r_m chosen equal 0.3a. The q_f has negative shear out to $r = r_m$ and then during the ramp phase the plasma heating causes the current to peak, but away from the axis, q reaches one and the collapse triggered again. This model is unsatisfactory as r_m is still arbitrary; detailed knowledge of the instability, as with the Kadomtsev model, is necessary to predict r_m. The chosen r_m determines the minimum $q_f(r)$ and thus τ_{saw}, the time for current diffusion to drop q to one, also depends directly on r_m. Ward obtained agreement between experimental τ_{saw} on JET and a theoretical prediction from this model. This is now shown to be somewhat fortuitous.

In a JET plasma with $q_a = 2.9$, r_m is specified, and TRID has been run toward equilibrium until steady–state sawteeth with constant τ_{saw} are observed. Figure 4.10 plots, as a function of r_m/a, the sawtooth period, and the position of the $q = 1$ surface. As r_m increases the minimum q_f becomes greater, the current peaks closer to the axis and τ_{saw} is a strongly increasing function of r_m, varying from near zero to 600ms for r_m varying between 0.28a and 0.36a. This heating time of course also depends on the thermal conductivity, Z_{eff}, and the total current. However the arbitrarines of r_m and the fact that toroidal modelling of the redistributed $B_z(r)$ is

required makes the minimum energy state collapse unsatisfactory for TRID. The Kadomtsev prescription although possessing limitations is the sawtooth model implemented on TRID.

4.6 *Averaged Sawtooth Effect*

Chapter 5 is concerned with the parametric variation in size of the steady-state 2/1 island, in which case detailed knowledge of the sawtooth is not necessary, and must be averaged so a true steady-state can be found. In fact the question of whether the post-collapse Kadomtsev profiles and τ_{saw} are predicted correctly need no longer concern us. Whatever the instability producing the collapse, the average effect of flattening the temperature and preventing q from dropping below one should be the same. This is achieved in TRID by enhancing the thermal conductivities $K_{e,i}(r)$ a large amount if a q=1 surface at $r=r_{s_1}$ should arise. This enhancement is over a region from r=0 to $r=r_m$ ($>r_{s_1}$) and has the form

$$K_e(r) = K_{e0}(r)\left[1 + \frac{K_1}{K_0}\left[1 - \frac{r^2}{r_m^2}\right]^2\right] , \qquad r<r_m \qquad (4.12)$$

As with eq.(3.14) and demonstrated in section 5.4 the particular functional form is irrelevant with the choice $K_1=100K_0>>K_0$. Eq.(4.12) serves to keep $T_{e,i}(r)$ flat in $(0,r_m)$, and also q(0) is kept very close to 1 (typically 0.995). This is because as soon as q falls below 1 the flattening of T_e stops the resistivity increasing and further peaking of current is prevented. No further enhancement of η is necesary to achieve this, unlike Turner and Wesson [9], where only an averaged sawtooth was modelled, and both an enhancement of K_e, similar to eq.(4.12), and an additional enhancement of resistivity was made. They also assumed a quadratic profile for current was always present before collapse, and so assuming the Kadomtsev prescription r_m was always taken as $r_m=\sqrt{2}r_{s_1}$. However from both experiment and the following TRID simulation the profiles are known to be much flatter, so r_m is significantly less than this. The curves in figure 4.11 are from a DITE simulation with only sawteeth present, but one in which a very slow current ramp is applied, so that at any time the sawteeth are almost steady with constant τ_{saw} and r_m. The period and ratio r_m/r_{s_1} are plotted as functions of $1/q_a$ in (a) and (b), and as functions of r_{s_1}/a in (c) and (d). Important features to note here are:

(i) For low current and r_{s_1} the mixing radius $r_m=1.4r_{s_1}$, which agrees with quadratic-like profiles being present near the axis. As r_{s_1} increases r_m/r_{s_1} decreases,

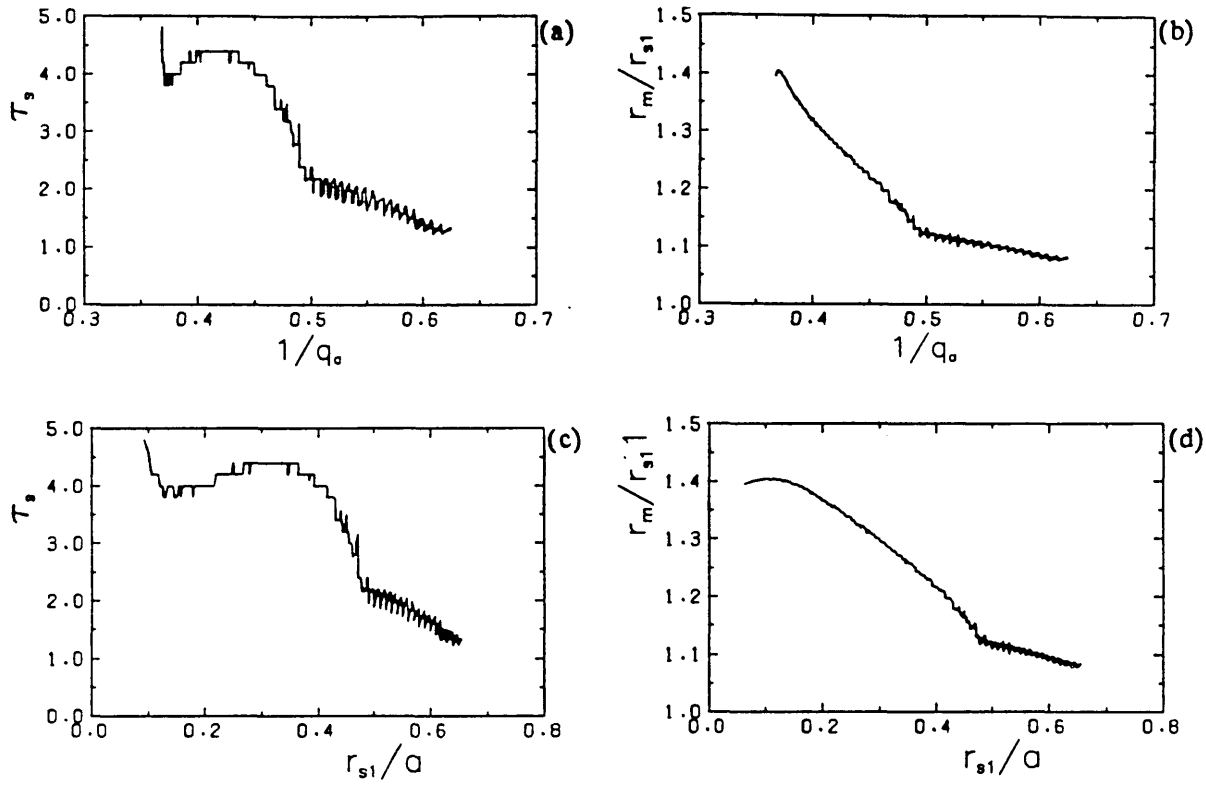

Figure 4.11 *(a) The steady state sawtooth period as a function of $1/q_a$ (current), for DITE parameters, with triggering of a Kadomtsev collapse by an m=1 resistive mode growing to large size. (b) The ratio of the mixing radius to r_{s1}, the position of the q=1 resonant surface, as a function of current. (c) Same as (a) but plotted as a function of r_{s1}. (d) Same as (b) but as a function of r_{s1}.*

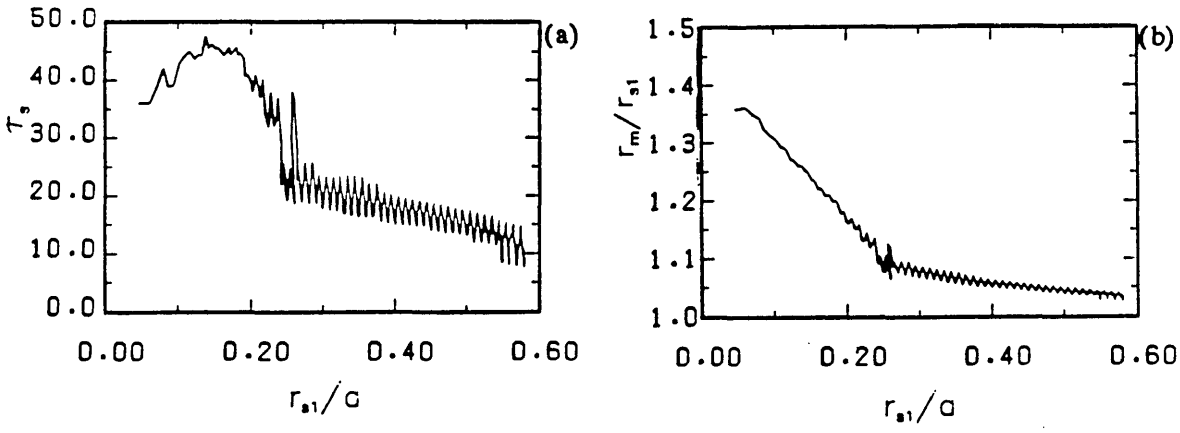

Figure 4.12 *(a) The steady state JET sawtooth period as a function of r_{s1}, for the Kadomtsev collapse triggered by the m=1 mode. (b) The steady state JET mixing radius, as a function of r_{s1}.*

so for $r_{s1} > 0.55a$, $r_m < 1.1 r_{s1}$.

(ii) The period τ_{saw} peaks for r_{s1} in the range (0.3a,0.4a) and then begins to decrease as r_{s1} becomes larger. The linear m=1 tearing growth rate γ_T goes as $\alpha_s^{2/3} \tau_R^{-1/3} \tau_A^{-2/3}$, and the larger shear, and the smaller temperature and density of resonant surfaces at larger radii account for the decrease in τ_{saw}.

(iii) A change in behaviour is evidenced by the change in the slope of both curves near $r_{s1} = 0.5a$. Observation of the q profiles shows for r_{s1} less than this that q is monotonically increasing with only one q=1 surface present, while above $r_{s1} = 0.5a$ q has an off–axis minimum with q(0)>1, and reconnection of helical flux profiles as in figure 4.8(a) now occurs.

Figure 4.12 plots the same sawteeth quantities as in figure 4.11, but for a JET plasma. The steady–state mixing radii of figures 4.11 and 4.12 are used for r_m in eq.(4.12) when an averaged sawtooth model is implemented. Two simple piecewise curves for r_m are fitted, as functions of r_{s1}, to figures 4.11(d) and 4.12(b), i.e. for DITE

$$\begin{aligned} r_m/r_{s1} &= 1.4 && 0<r_{s1}<0.1, \\ &= 1.411 + 0.026 r_{s1} - 1.316 r_{s1}^2 && 0.1<r_{s1}<0.48, \\ &= 1.240 - 0.235 r_{s1} && 0.48<r_{s1}, \end{aligned} \qquad (4.13)$$

and for JET

$$\begin{aligned} r_m/r_{s1} &= 1.450 - 1.424 r_{s1} && 0<r_{s1}<0.26 \\ &= 1.130 - 0.164 r_{s1} && 0.26<r_{s1} \end{aligned} \qquad (4.14)$$

An interesting numerical instability was observed with the averaged–sawtooth model and is discussed in Appendix C. It's effect is to limit Δt to small values, typically less than 1.0ms for DITE if the enhancement is large.

4.7 *Disruption: An Interaction Between Sawteeth and m≥2 Islands*

The results of combining both explicit modelling of Kadomtsev sawteeth and m≥2 island evolution are shown for in figure 4.13 for a standard DITE discharge with $q_a = 2.6$. Only the 2/1 and 3/2 islands are found to be unstable, and the positions of their inner and outer edges (solid lines), the resonant surfaces (dashed lines), and the sawtooth mixing radii are shown in figure 4.13(a). A dynamic equilibrium is rapidly attained with steady oscillation of both the saturated island sizes, and the changes this

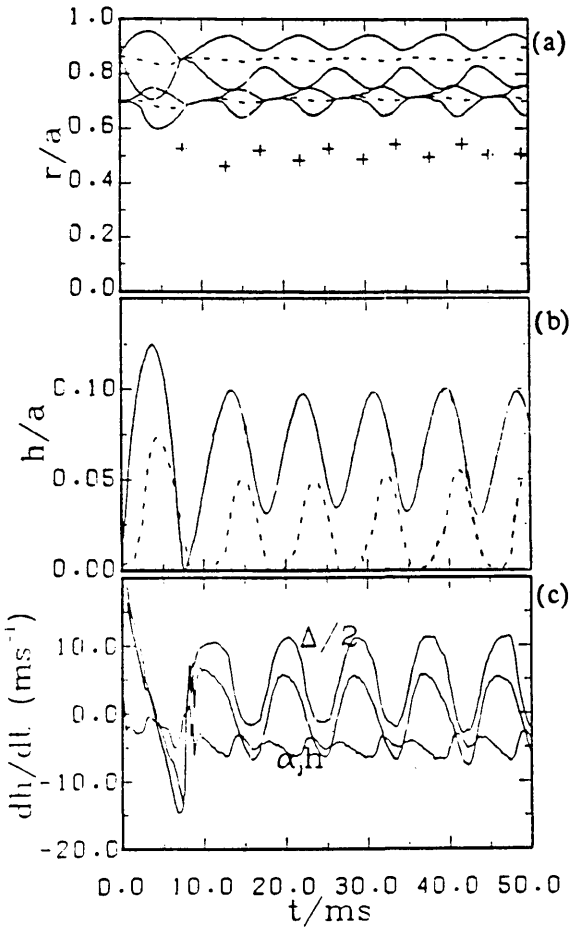

Figure 4.13 *(a) The behaviour of the 2/1 and 3/2 island regions (solid lines) after initialisation of a DITE plasma with q_a=2.6. Dashed lines are resonant surfaces, and crosses the positions of sawteeth mixing radii. Dynamic equilibrium is rapidly attained.*
(b) Island half widths h_{21} (solid line), and h_{32} (dashed line).
(c) Central curve is the growth rate of the 2/1 island. The contributions from the zero order term Δ/2, and first order term $\alpha_j h$, are also shown.

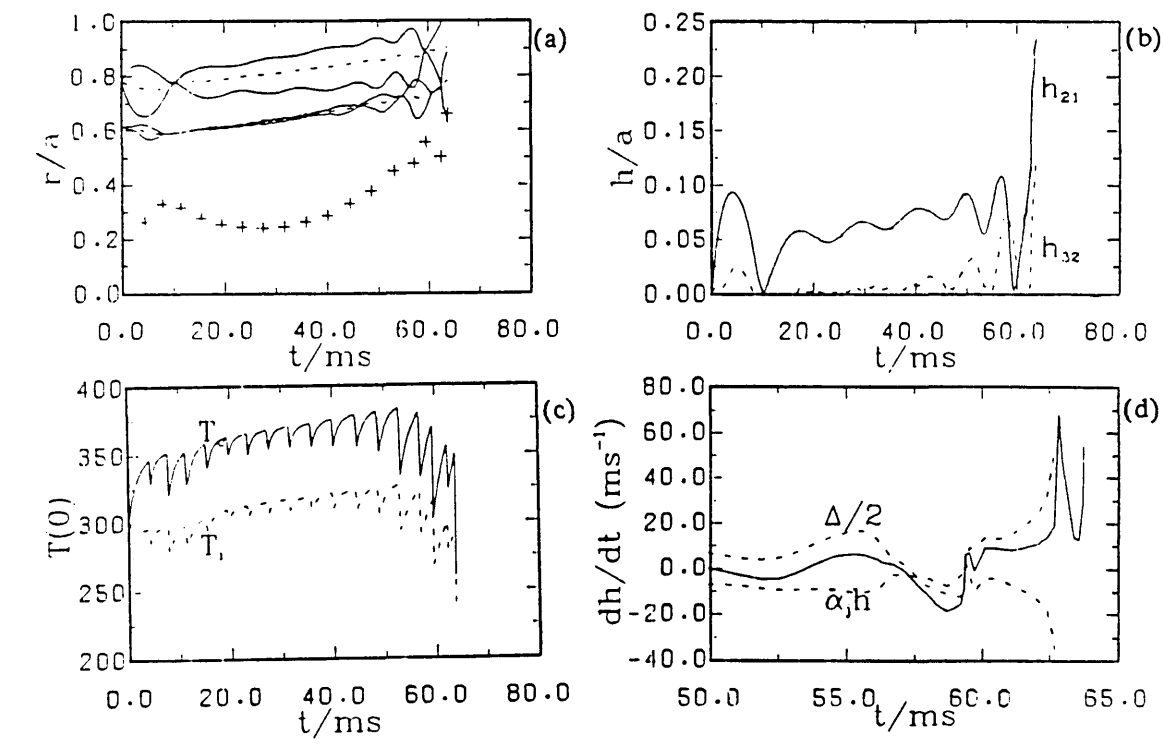

Figure 4.14 *(a) Island regions for the 2/1 and 3/2 modes, and also the sawtooth, for a current ramp simulation with $q_a(t=0)$=3.1 and t_d=230ms. (b) Island sizes. (c) Axial electron and ion temperatures. (d) Growth rate of the 2/1 island (solid line) from t=50ms until termination of the simulation when r_m intersects the 2/1 island.*

makes to the current profile also induce oscillation in r_m. The h_{21} oscillation leads h_{32}, which in turn leads r_m. As the 2/1 island grows this steepens the current gradient inside the $q=2$ surface, especially at the $q=1.5$ resonant surface of the 3/2 mode, and the 3/2 mode is destabilised, while it is the additional profile−flattening from the 3/2 island that stabilises the 2/1 island and causes the oscillation. With no 3/2 mode present and $q_a=2.6$, h_{21} is observed to grow without bound from initialisation, and the subsequently described disruption occurs. At lower current, with only a 2/1 mode permitted, no disruption takes place, a damped oscillation of h_{21} always occurs and a steady−state is eventually reached as in figure 3.5. With both modes present there is a critical safety factor $q_a \approx 2.85$, above which similar damped oscillation of the islands is seen, and below which the interaction between the modes is strong enough to give the oscillations of figure 4.13(a). The average value and amplitude depend strongly on the transport coefficients K_e and η.

In the simulation in figure 4.14 a linear current ramp (eq.(3.18)) is applied with $q_a(t=0)=3.1$ and a doubling time t_d for the current of 230ms. Initially the lower current means the islands are more deeply embedded within the plasma, so there is more current outside the resonant surfaces and the 3/2 mode is completely stabilised, while the 2/1 mode does begin a relaxation oscillation, as in figure 4.13, but of smaller amplitude. The resonant surfaces move out toward the limiter with increasing current and h_{21} gradually grows larger. As current tries to diffuse into the centre, the restriction of axial current due to the steady sawteeth present there means the mixing region moves outwards, and an increasing proportion of plasma is involved in the sawteeth. At $t=55$ms the 2/1 mode drives the 3/2 mode unstable for the first time, and the subsequent flattening of current causes h_{21} to then decay significantly. However at $t=59$ms, corresponding to the second to last sawtooth, there is a sudden increase in h_{21} growth (which eventually also drives h_{32} unstable). This occurs because r_m at this time is close to the outer islands. Directly after collapse the 2/1 mode therefore experiences a large j_z' inside $q=2$, and as the mode is now also close to the wall, there is little stabilising effect from the outer region current.

The growth rate for the 2/1 island (middle curve) is plotted in figure 4.14(d), along with the contributions to it proportional to $\Delta/2$ and $\alpha_j h$. After $t=62.5$ms these are not included on the scale of figure 4.14(d). At this time the island intersects the limiter and it rapidly cools to the edge temperature, so η_s, a factor in the growth rate, increases sharply. After intersection with the limiter the growth rate actually decreases, while still remaining positive. The noise in dh/dt at 59ms is associated with h_{21} going to zero, and arises because of the suddenness of the change in j' and j''

when the profile flattening is removed. Increasing the number of grid points gives a smoother response for dh/dt when h is small.

The net result of $m \geq 2$ island growth to large size is a restriction on the amount of current able to flow in the outer region, and this, along with the sawtooth restricting the axial current means the next sawtooth collapse has a mixing radius that intersects the inner edge of the 2/1 and 3/2 islands. This interaction between the hot interior and the cool exterior regions gives a large drop in $T_e(0)$ from 350eV to 255eV. Prior to this final collapse the preceding few sawteeth have increased significantly in size as the mixing radius has moved outwards towards the cooler island regions. The collapse at t= 59ms when h_{21} is also large, gives a 21% change in $T_e(0)$ and could be interpreted as a minor disruption. The magnetic signals associated with the perturbed fields $B_{\theta 1}$ and B_{r1}, with mode number m, are [58]:

$$\left.\frac{B_{\theta 1}}{B_\theta}\right|_a = \frac{1}{\psi_s}\left.\frac{\partial \psi}{\partial r}\right|_a \frac{B_{\theta s}}{B_{\theta a}} \frac{h^2}{4} \frac{q_s'}{q_s} \quad , \quad \left.\frac{B_{r1}}{B_\theta}\right|_a = \frac{m\psi(a)}{a\psi_s} \frac{B_{\theta s}}{B_{\theta a}} \frac{h^2}{4} \frac{q_s'}{q_s} \qquad (4.14)$$

i.e. they are proportional to h^2. Therefore this simulation reproduces both the temperature collapse and the growth of the $B_{\theta 1}$ precursor in figure 1.1 prior to disruption. It is also unlikely that the plasma would easily recover after such a violent sawtooth that essentially provides a thermal short-ciruit across the whole plasma. For these reasons this interaction between the 2/1 island and the sawtooth has been taken to be equivalent to a disruption, and at this point the simulation is then terminated.

4.8 *Influences on Disruptive Behaviour*

Figure 4.15(a) and (b) show the island behaviour, and T(0) for an identical simulation to figure 4.14, but with the averaged sawtooth model of section 4.6. The agreement between the two is very good. Hopcraft and Turner [59] also simulated a current-limited disruption but differing from figure 4.14 in some respects. Prior to disruption in [59] three large oscillations in h_{21} are observed, in which the island grows to large size before decaying to zero. h_{32} is destabilised each time and r_m also responds in an oscillatory manner. These were interpreted as "minor" disruptions. The islands in the TRID simulation exhibit much more stable behaviour, until just prior to disruption. The difference in island behaviour can be explained by the additional stability provided by the $\alpha_j h$ term in eq.(2.67), while the deficiences in the sawtooth averaging of [59] also contribute to the extra instability.

In [59] the 3/2 island is more unstable, attaining a much larger size. It's inner edge at disruption is inside the 2/1 island, and it hastens the creation of a thermal short-circuit. In figure 4.14, h_{32} is always much less than in [59] and, near disruption, the inner edges of both the islands are coincident. The actual role of the 3/2 mode in disruption is shown in the TRID simulation of figure 4.15(c). The current-limited disruption of figure 4.14 is repeated, but without the stabilising influence of the 3/2 mode. Little oscillation in h_{21} is seen and disruption occurs as early as t= 54ms. The 3/2 mode does have a role in delaying disruption, but it is strong instability of the 2/1 island, and subsequent interaction with the sawtooth that explains the initiation of disruption.

Hopcraft and Turner [59] used a faster current ramp while simulating disruption, so now a comparable doubling time for the current, t_d= 100ms, is used to obtain figure 4.15(d) with all other parameters unchanged from section 4.7. The faster ramp enables q_a= 2.37 to be reached before disruption, to be compared with q_a= 2.44 at the time of disruption with the slower ramp. The islands exhibit no oscillatory behaviour, and rapid growth of h_{21} is initiated not by sawtooth current-steepening, but by actual contact of the island with the limiter.

Turner and Wesson [9] also neglected the first order term in the nonlinear growth equation (3.26). Figure 4.15(e) and (f) show the effect of such a neglect in TRID in an identical simulation to the oscillating islands of figure 4.13. After initialisation less than 4ms elapse in (e) before the islands, which grow continuously, overlap and interact with the sawtooth. The role of α_j is further investigated in section 5.2.

Figure 4.15(f) plots the same island structure as (e), but on an expanded scale just prior to collapse, and illustrates how several partial sawtooth collapses of section 4.4 occur before a full collapse extending to the axis provides the thermal quench. At t= 2.9ms the peaking of current, caused by diffusion of current from the outer region (where the m= 2 island has restricted the current), causes a second q= 1 surface to arise at position r_{s12} in figure 4.15(f). It is not until t= 3.3ms that the helical flux has evolved sufficiently so reconnection to the axis can occur.

Finally for this section figure 4.16 demonstrates the plasma behaviour when a large number of modes are included. Once again the simulation of figure 4.14 is repeated, but only for 50ms before being restarted with many extra modes switched on. In order of decreasing radius from r= a they are: m/n= 2/1, 5/3, 3/2, 4/3, 5/4,

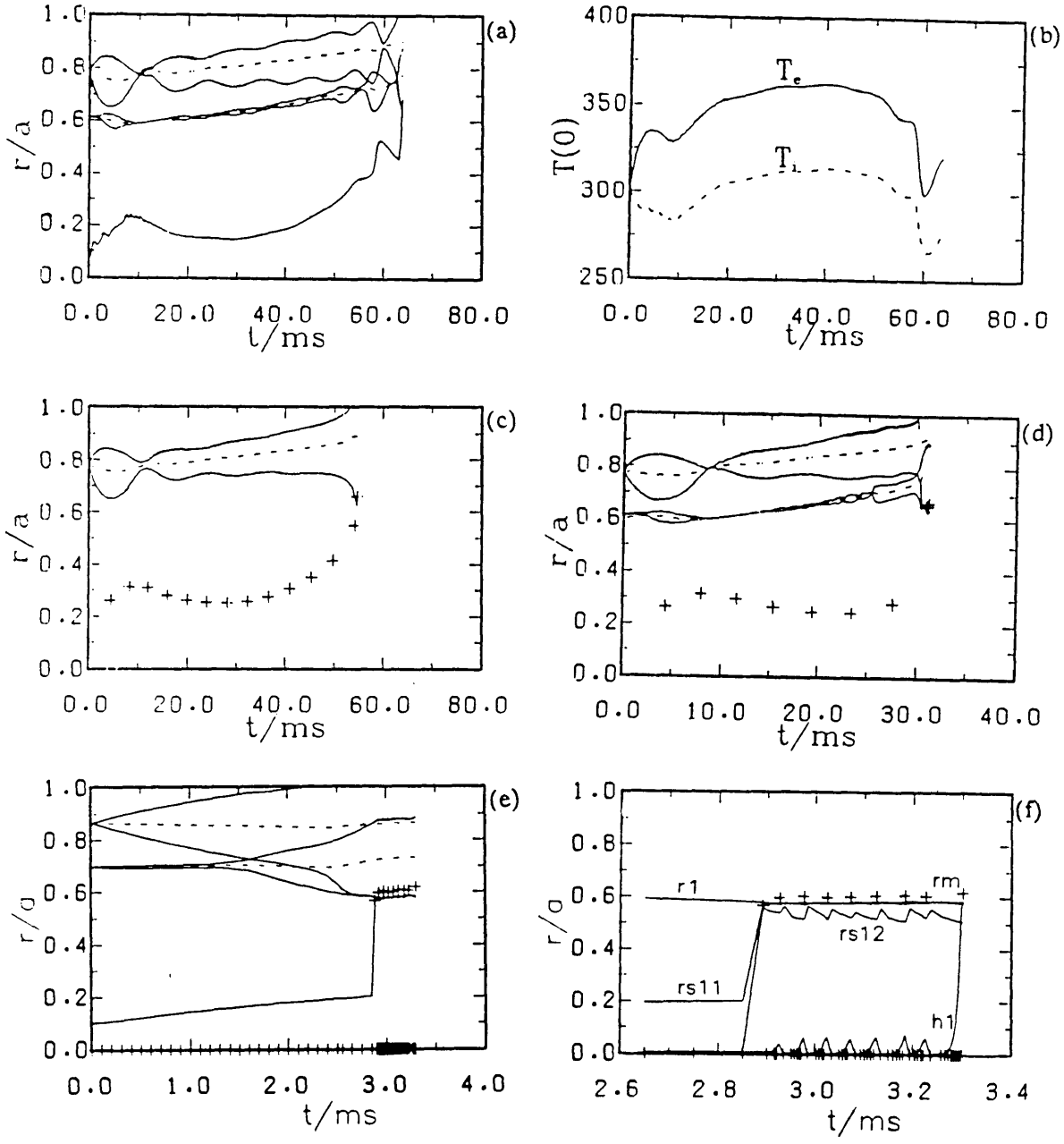

Figure 4.15 *All simulations here are identical to the current ramp simulation of figure 4.14 but investigations of different models and conditions are made. (a) and (b) show the island regions and the axial temperatures respectively, when the average sawtooth model of section 4.6 is used. (c) The 3/2 mode is excluded but otherwise this is an identical simulation to figure 4.14. (d) The doubling time of the current is reduced to 100ms. (e) The first order term in eq.(3.26) is excluded. The islands grow without bound and intersect the sawtooth after only 3.3ms. (f) Expanded timescale for (e) prior to disruption. Two resonant surfaces r_{s11} and r_{s12} arise, and several partial reconnections occur before collapse to the axis is achieved.*

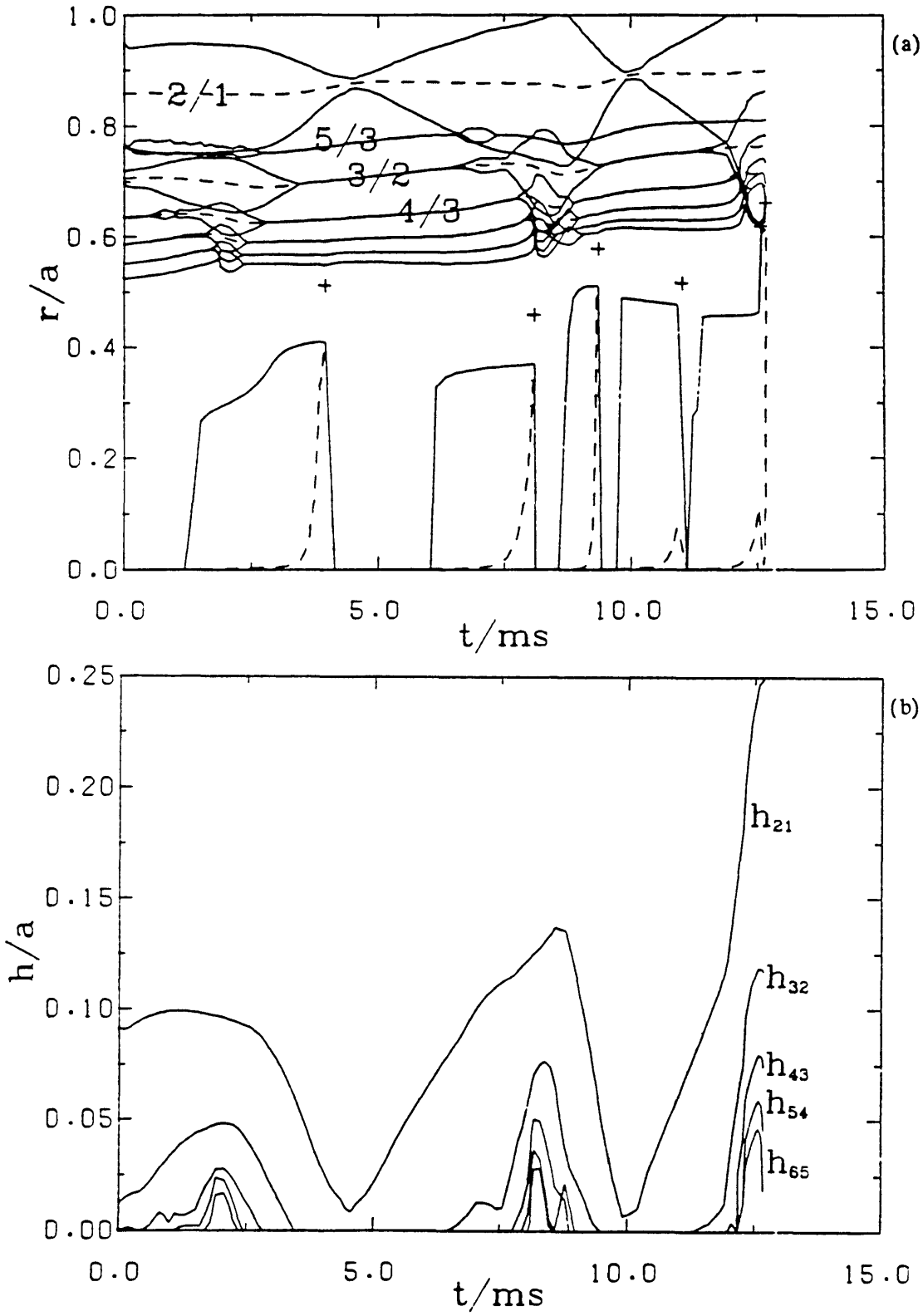

Figure 4.16 *The simulation of figure 4.14 is restarted from t=50ms with a large number of extra modes whose resonant surfaces in order of decreasing radius in (a) are: m/n=2/1, 5/3, 3/2, 4/3, 5/4, 6/5, 7/6. Also included in (a) is the dynamical behaviour of the island regions, the sawtooth mixing radii (crosses), the q=1 surface, and the size of the m=1 island. (b) plots the actual island widths.*

6/5, 7/6. Figure 4.16(b) plots several of the island widths. Tests including modes outside the range $1 \leqslant m/n \leqslant 2$ show they are not strongly excited. The steepening of the current gradient inside $q=2$ at $t=6.8$ms and $t=11.7$ms now not only excites the 3/2 mode, but initiates an sequence of unstable high m and n modes. The main constituents in the cascade are the Fourier components with $m=n+1$, whose respective resonant surface are located successively deeper within the plasma. The higher the mode number, the later the onset of instability, although the delay between high−m modes tends to zero for large m. The sawtooth at 7.5ms does not intersect the islands which then decay due to flattening of the current, but the next sequence of island growth at higher current does produce a total overlap of modes, and disruption.

This behaviour can be characterised as an inwardly accelerating "shock−front" and was first reported by Bondeson [23] using a 3D code that solved the reduced equations in cylindrical geometry with finite differences in the radial direction and Fourier expansion in the θ and z directions (although this TRID simulation was made concurrent with, but independent of [23]). The surprising feature here is that TRID should reproduce exactly the same dynamic behaviour, and this underlines the dominant effect of the zero−order current on tearing mode stability, and shows how the TRID quasilinear model with transport enhancement can be trusted to represent dynamic island behaviour. However the critical requirement to initiate disruption is the growth of the 2/1 island, and so in the parametric analyses of Chapter 5, which seek to discover the causes of disruption, it is necessary to examine only the saturated 2/1 island size to find disruption limits. All following time−dependent disruption simulations, for reasons of clarity and computational economy, will show just the 2/1 and 3/2 (and sometimes 3/1) modes, but it must be remembered that associated with each disruption there is the cascade to short wavelength modes and the inwardly propagating shock observed here.

CHAPTER FIVE

PARAMETRIC STUDIES

5.1 *Introduction*

The previous chapter showed the 2/1 island size is critical in determining the stability of the plasma to disruption. The saturated island size will vary as plasma quantities such as current, thermal conductivity, and additional heating, to name just a few, are varied. This chapter is therfore concerned with the parametric variation in island size, and in particular, in determining what changes in plasma conditions are instrumental in initiating or preventing disruption.

To this end it is apparently just necessary to run TRID for a long time to determine plasma quantities for each point of a parametric variation. However it has been shown in figure 4.14(a) for example, that steady-state equilibria are not always attained, and in fact the 2/1 island and plasma as a whole often undergo a relaxation oscillation. The approach here therefore has been to adapt TRID so that the plasma evolves toward an equilibrium containing island-flattened profiles, but with h_{21} a specified quantity. A succession of these equilibria are then found for h_{21} increasing from 0 to 0.16a. Only that case for which dh/dt= 0 corresponds to a true saturated equilibrium. This process must be repeated over the whole range of parametric variation, but is not too consuming as the perturbed flux now does not have to be evaluated at every timestep, and as only the final equilibrium is of interest then relatively large timesteps can be used (possible with an implicit code).

This equilibrium code is henceforth referred to as "SAT". The sawtooth in SAT is represented by it's averaged effect, and the other modes (3/2, 3/1 etc) can not be included. This is not a real disadvantage as for reasons already discussed, it is sufficient to study only the 2/1 mode when examining disruption criteria. If there exists no equilibrium with a saturated island (dh/dt$>$0 for all h) then this is taken to represent a disruptive plasma and h_{21} is set equal to 0.2, the outer edge of the island intersects the limiter, and r_m and the inner island edge are set equal.

In section 5.2 the current-limit is reviewed, section 5.3 examines the influences of a shaped thermal conductivity, and section 5.4 investigates how the position of a conducting wall can be critical in providing stability. In section 5.5 both the

time-dependent behaviour of additionally heated profiles, and the response to parametric variation of the additional heating is studied. The last section examines the possibility that high-n ballooning mode instability could be present, especially with the high pressure gradients prior to disruption.

5.2 *High-Current Equilibria*

From calculations with the TRINIO code Wesson et al. [4] deduced a catastrophe model to explain the current-limited disruption. This was done taking only the zero-order term in the Rutherford island growth equation, so that saturation corresponds to $\Delta(h)=0$. This section examines the effect of the first-order term in eq.(3.26) on this model. It will be shown that the catastrophe model still holds, although a significantly more optimistic current-limit results, so the following results provide both a summary and an extension to the catastrophe model.

Figure 5.1(a) plots the growth rate dh/dt, from a SAT calculation of a DITE plasma, as a function of saturated island width h_{21} for several values of q_a. The intercept of each curve with the dh/dt=0 axis provides the saturated island width. As q_a decreases this increases, and by $q_a=2.70$ the growth rate curve develops a turning point with a second, unstable solution for the saturated island size. At some critical current between $q_a=2.70$ and $q_a=2.68$ the minimum of this curve will just touch the axis, and if the current is raised infinitesimally above this then equilibrium with a saturated island no longer exists. The island would grow spontaneously without limit, for an apparently infinitesimal change in plasma quantities, and disruption would result.

Comparison between the inclusion and exclusion of α_j is made in figure 5.1(c), which plots the saturated island size as a function of $1/q_a$, and in figure 5.1(d) which shows the radial extent of r_m and the 2/1 island. The dashed lines correspond to the $\alpha_j=0$ case. A significant result of this comparison is the saturated width for low current, which for $\alpha_j\neq0$ is almost constant at 0.06a whereas for $\alpha_j=0$ it is 65% to 75% greater. This contradicts [18], where the first-order term was shown to be of negative sign, and inclusion of α_j predicted larger saturated widths. This can be attributed to the dominance of the j_a' and j_a'' terms in eq.(2.68), as the zero-order current was not flattened by the island in ref. [18]. In TRID, once an island grows then the gradient terms in eq.(2.68) can be neglected and α_j is equal to

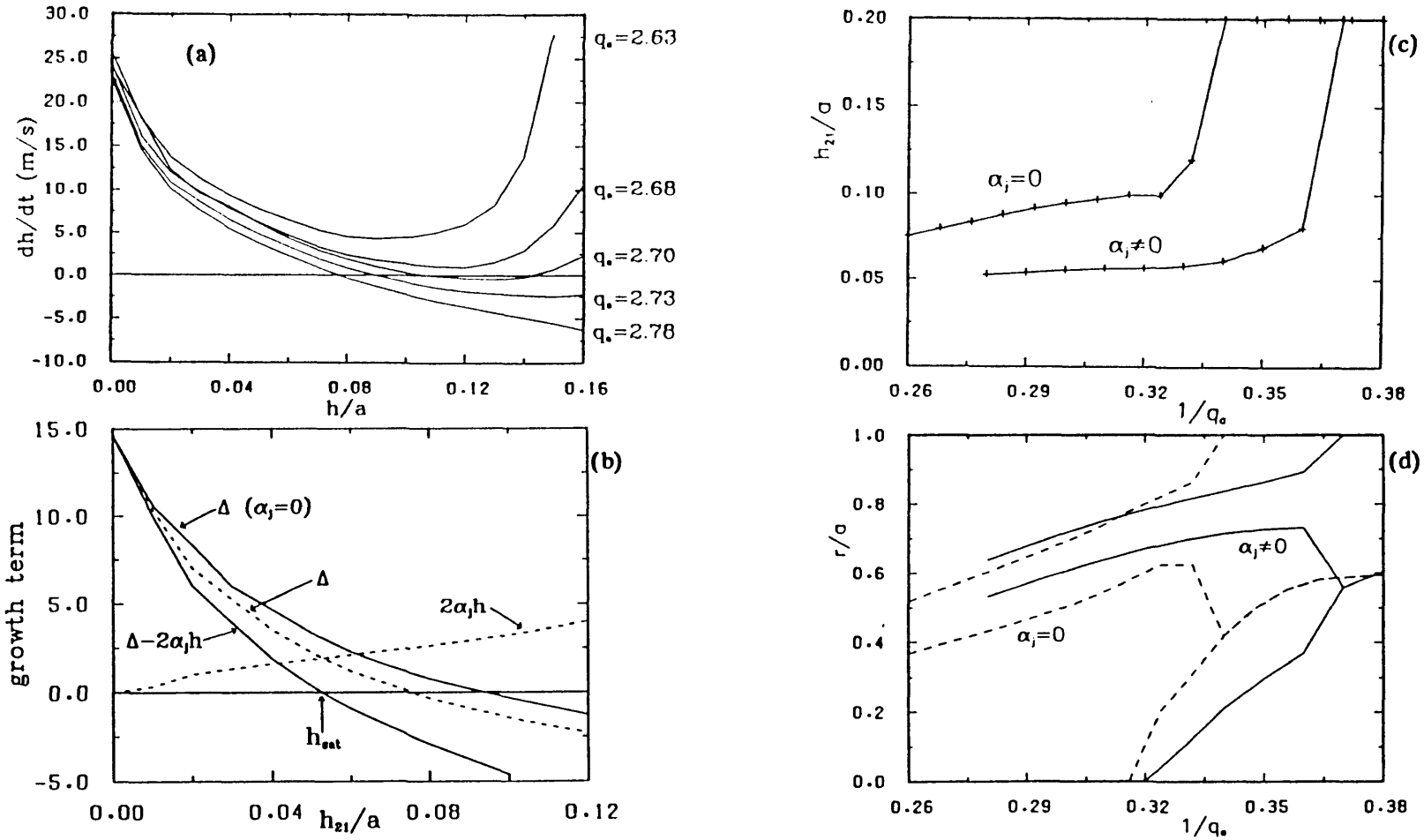

Figure 5.1 (a) Calculated graphs of 2/1 growth rate at equilibrium, versus specified island size, for several values of q_a. Intercept of the curves with the dh/dt=0 axis give the true saturated island width. (b) Dotted lines are $\Delta(h)$ and $2\alpha_j h$ as functions of h, for q_a=3.2. Subtraction of these terms gives the solid line with corresponding h_{sat}=0.052a. The other solid curve is $\Delta(h)$ with α_j and s neglected. (c) Saturated island size h_{21} as a function of $1/q_a$. Comparison is made between neglect ($\alpha_j h$=0) and inclusion of the first order term. (d) The corresponding 2/1 island and sawtooth regions for (c).

$$\alpha_j = \left[\frac{m^2}{r_s^2} - \frac{s}{r_s}\right] \qquad (5.1)$$

and so is necessarily positive and stabilizing. The reason for such a large reduction in h_{21} when $\alpha_j h$ is included becomes apparent when the two terms in the expression (2.68) for nonlinear island growth are plotted, as in figure 5.1(b), as functions of h. The dotted lines show the relative sizes of Δ and $2\alpha_j h$, and their subtraction gives the solid curve that implies $h_{sat} = 0.052a$. At this point of saturation $r_s = 0.71a$, $\Delta(h) = 2.0$, $s = -7.6$, and $\alpha_j = 18.5$; typical values for these quantities. One can verify that α_j is given by eq.(5.1). The other solid curve in figure 5.1(d) is $\Delta(h)$ calculated neglecting α_j and s, and is shifted to the right, relative to the dotted $\Delta(h)$ curve. This is because with $s \neq 0$ the island is then asymmetric about r_s. $\psi_1'(r_2)$ is little changed but $|\psi_1'(r_1)|$ is less and so $\Delta(h)$ is reduced, and enhancement of the island stability, in addition to that from the first order term, is obtained. The current-limit in figure 5.1(c), predicted to zero order is 3.0, while to first order this is reduced to $q_a \approx 2.70$. The effect on this limit of altering the position of the conducting wall is examined in the next section.

5.3 *Conducting Wall*

In section 2.5 it was demonstrated how the presence of a perfectly conducting wall strongly stabilizes the linear growth of the resistive tearing mode. The saturated size of magnetic islands would therefore be expected to be diminished as the relative position b/a of the wall approached 1. Figure 5.2(a) plots h_{21} against $1/q_a$ for three values of b/a. For $1/q_a$ up to ≈ 0.33, h_{21} is the same (0.05a) in all three cases. The island at these low currents is deeply embedded in the plasma away from the wall and so the potential energy available for driving the mode completely dominates the wall stabilization. With no conducting wall ($b/a = \infty$) the width rapidly grows as current increases and the current-limit of the previous section is reproduced. For the other extreme of $b/a = 1$ the island is made continously more stable as current increases so by $1/q_a = 0.43$ no 2/1 instability is present, and the TRID model would predict no disruption. For the intermediate case of $b/a = 1.2$ the island at first becomes more unstable as q_a decreases below 3, but the wall stabilization becomes relatively more important at higher current as the island approaches the wall, and the island is stabilized.

Most present-day tokamaks operate with a poorly conducting wall, equivalent to

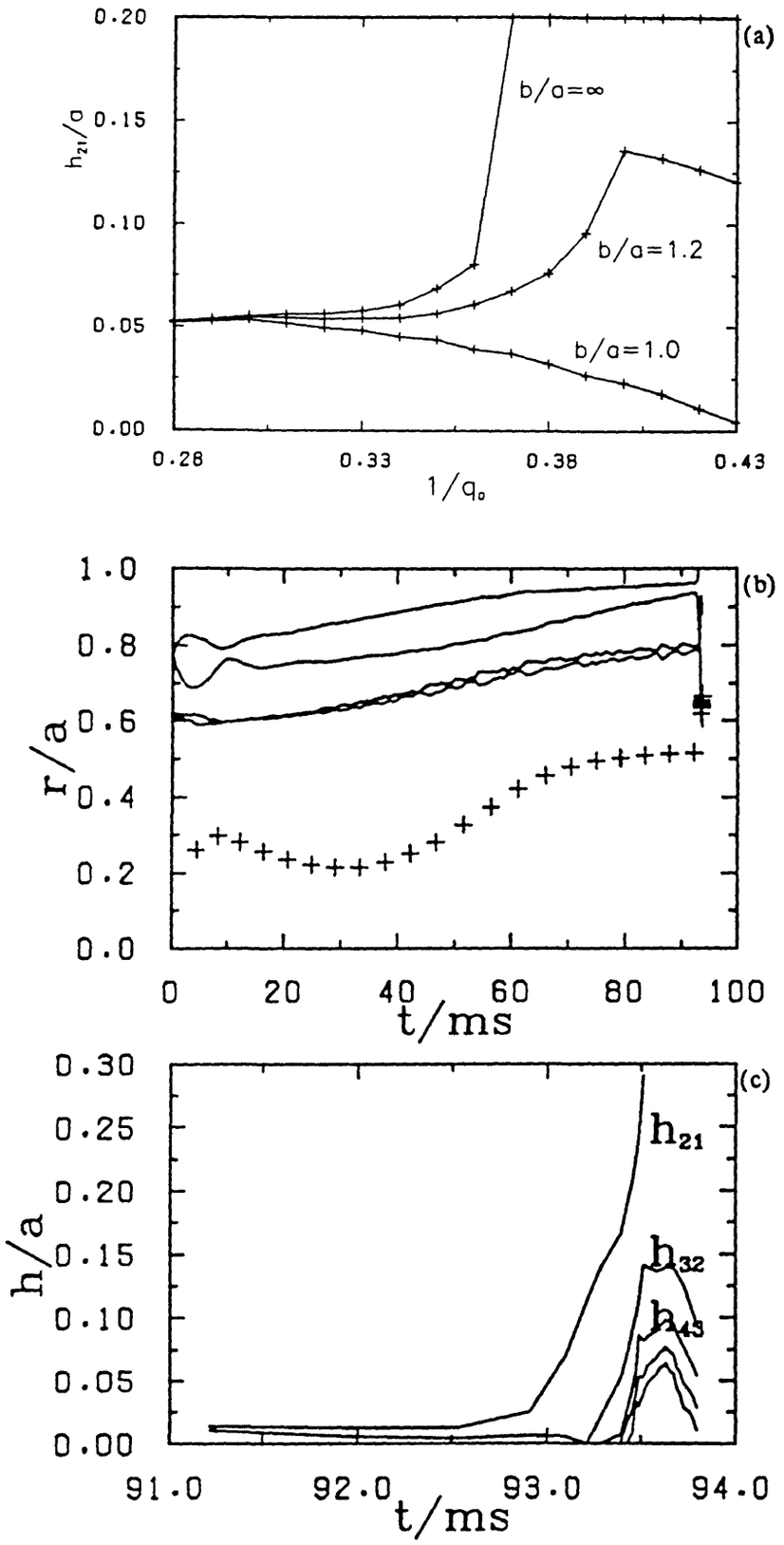

Figure 5.2 *(a) Saturated island width h_{21} as a function of $1/q_a$, for three positions of the conducting wall.*
(b) The current ramp simulation of figure 4.14 is repeated, with a poorly conducting wall at b=1.05a, but with wall stabilization while r_s<0.95a. (c) The island widths for (b).

$b=\infty$, but the q−limit predicted here, although reduced from 3.0 to 2.7 by the inclusion of α_j, can still not be reconciled with experimentally observed current−limits. JET for example [42] reports a q−limit of 2.0±0.1 over a wide range of operating conditions, although it operates with a closely−fitting, but only partly conducting wall that would be expected to provide only minimal wall stabilization. This problem appears to have been solved in some recent work by Persson and Bondeson [60], in which the effects of an equilibrium poloidal plasma rotation are considered. At the resonant surface the perturbed field must rotate with the plasma, and if the frequency of rotation is much greater than the inverse resistive time−constant of the wall then the perturbed field will not be able to diffuse through the wall, which will then appear conducting. As the current is increased the saturated width would then follow the b/a= 1 curve of figure 5.2(a).

The 2−D numerical simulation of [60] that solves the reduced equations with equilibrium rotation, but no resistivity evolution, shows what happens as the resonant surface reaches the poorly conducting wall. The mode in this resistive region is able to decouple from the the rotation; it's rotation slows and the flux begins to diffuse through the wall. As the mode rotation decreases, wall stabilization becomes less, the flux at the wall increases, and the mode becomes ever more unstable, Eventually the simulation showed locking of the mode to the wall, allowing it to appear non−conducting and precipitating rapid 2/1 growth. It was suggested that if the outermost region of the plasma was highly resistive, then mode−locking and growth would occur when the q= 2 surface entered this region, giving rise to the observed q−limit just above 2, but this has yet to be demonstrated.

A simple modelling of this scenario is possible in one dimension with TRID if it is assumed there is a highly resistive region between r_r and a, and also that a poorly conducting wall is now located at r= b, but while r_s lies inside the resistive region it appears conducting. When r_{21} enters this region the mode is assumed to rapidly lock, and stabilization disappears so b increases to infinity. This can be modelled, redefining b and the edge resistivity by

$$b = b\exp\left[\alpha_r\left[\frac{r_{21}-r_r}{1-r_r}\right]\right] , \qquad r_{21} > r_r \tag{5.2}$$

$$\eta = \eta_{sp}\exp\left[\alpha_r\left[\frac{r-r_r}{1-r_r}\right]\right] , \qquad r > r_r \tag{5.3}$$

Figure 5.2(b) repeats the current ramp simulation of figure 4.14 but with b= 1.05a,

$r_r = 0.95a$ and $\alpha_r = 7$ (so $\eta(a) = 10^3 \eta_{sp}$). The 2/1 island now becomes progressively smaller as current increases until r_s exceeds r_r when stability is lost and it grows explosively. This can be seen more clearly in figure 5.2(c) which plots several island widths on an expanded timescale near the point of destabilization. Other modes are also driven unstable, and the outer region current diffuses inwards, so that the sawtooth mixing radius intersects the cold region after several partial reconnections. The current at disruption is equivalent to $q_a = 2.20$, but this depends on the arbitrary choice of $r_r = 0.95a$ made here.

It appears from this short review of [60] that the high-current limit disruptions of chapter 4 must be doubted. However, as illustrated in figure 5.2(a), the saturated island size is independent of any conducting wall for q_a down to 3.0, and so parametric dependencies demonstrated subsequently are valid for q_a greater than this. Similarly, simulation of density-limit, high-q disruptions in Chapter 6 can be expected to give a valid description of tokamak behaviour.

5.4 *Thermal Conductivity*

It is necessary to be sure the particular form chosen for the enhancement of transport across an island, ie eq.(3.14):

$$K_e(r) = K_{e0}(r)\left[1 + K_1((r-r_c)/h)^2\right]^{\alpha_1} \qquad (5.4)$$

does not influence island stability and size. Using SAT, figure 5.3(a) plots the saturated 2/1 island width versus the relative transport coefficient K_1/K_0 for a DITE plasma, with $q_a = 3.3$, flat background electron thermal conductivity ($K_{e0}(r) = K_0$), and α_1 chosen equal to 2. With $K_1 = 0$ and thus no transport-consistent modification of the zero-order current profile then quasilinear saturation alone would predict a large 2/1 island of size 0.14a, but as K_1 becomes larger this rapidly decreases to the constant value of 0.055a.

Figure 5.3(b) plots the saturated width versus the shaping factor α_1 for three values of K_1. As α_1 increases the shape of the enhancement becomes increasingly spike-like and this explains the increase in saturated width h_{21} for large α_1. The current gradient is now no longer reduced so much, especially near the island edges, resulting in slightly larger islands. However for large K_1 and small α_1 corresponding to strongly flattened profiles then h_{21} is independent of K_1 and α_1. Such strong

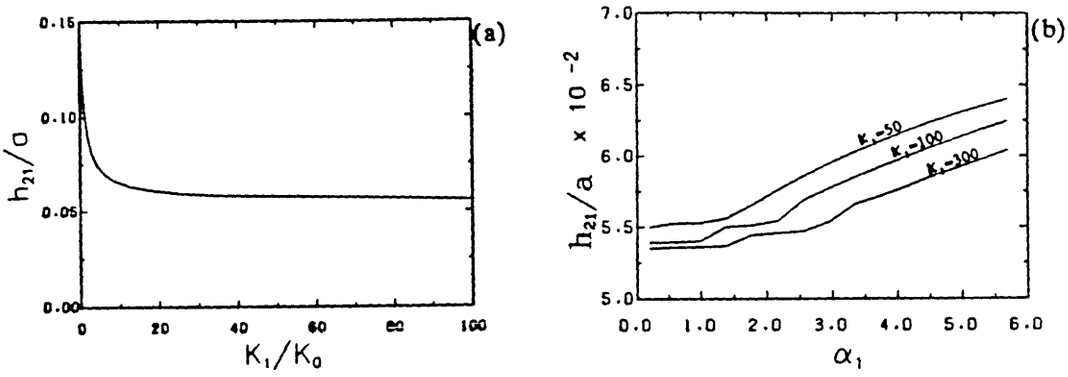

Figure 5.3 *(a) Saturated island width h_{21} as a function of island thermal conductivity enhancement K_1, for a DITE plasma with q_a=3.3. (b) h_{21} as a function of α_1, the shape factor of the enhancement, for three values of K_1.*

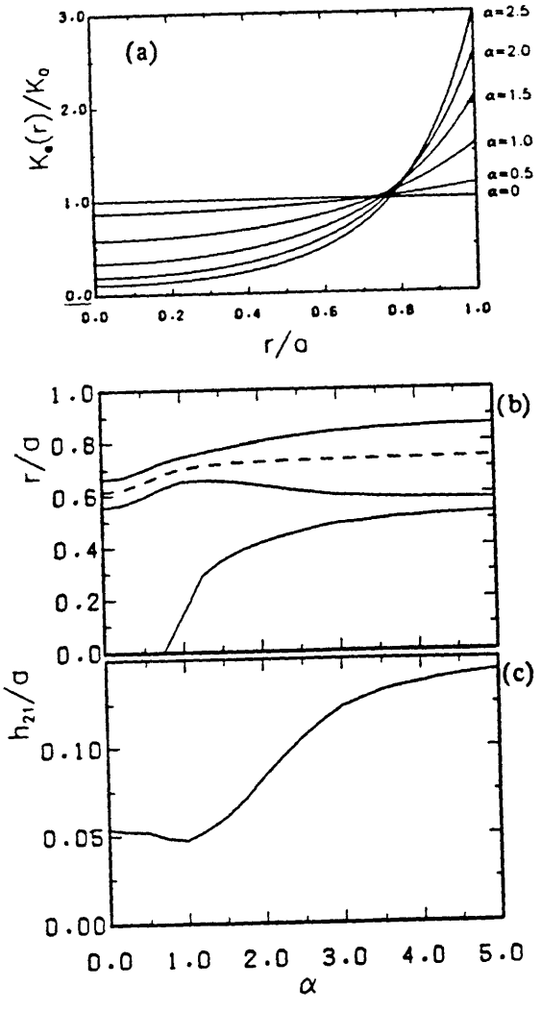

Figure 5.4 *(a) The background electron thermal conductivity profile given by eq.(5.5), for increasing α. (b) The 2/1 island and sawtooth regions, as functions of the thermal conductivity shape α. (c) The saturated island width corresponding to (b).*

modification would indeed be implied by $K_{||} \approx 10^{12} K_{\perp}$, so all previous and future numerical experiments use $K_1 = 100 K_0$ and $\alpha_1 = 1$.

The effect of a non-constant anomalous electron thermal conductivity is now investigated with SAT. The general form

$$K_{e0}(r) = C T_e^{-\nu} \tag{5.5}$$

where C and ν are variable, is introduced by Roberts [61]. $\nu = 0$ corresponds to the Alcator scaling used until now, while ν between 0.5 and 1.0 gives a better fit to other devices [62,63]. K_e is generally an increasing function of radius. However eq.(5.5) is a function of two free parameters, C and ν, which would provide an unduly complicated dependency of h_{21} on $K_{e0}(r)$. The approach here therefore has been to parametrise $K_{e0}(r)$ also as an increasing function of r, but in terms of a single parameter α, and to require: (i) $K_{e0}(r)$ to be constant for $\alpha = 0$, and (ii) the average value of $K_{e0}(r)$ to be constant; i.e.:

$$K_e(\alpha=0, r) = K_0 \tag{5.6}$$

$$\int_0^1 K_e(\alpha, r) r dr = \frac{1}{2} K_0 \tag{5.7}$$

If $K_{e0}(r)$ going as $\exp(\alpha r^2)$ is chosen, then eqs.(5.6) and (5.7) imply:

$$\frac{K_{e0}(r)}{K_0} = \frac{1 + \alpha\left[e^{\alpha r^2} - 1 \right]}{e^{\alpha} - 1} \tag{5.8}$$

and this has been plotted in figure 5.4(a) for several choices of α.

It should be emphasised that eq.(5.8) is a convenient, arbitrary choice for K_e that does not have a theoretical basis, but it should qualitatively represent a variety of experimentally derived scaling laws and analytic expressions, and give some general information on how h_{21} scales with increasingly steep conductivity profiles. Other one-parameter scalings for $K_e(r)$ (eg power-law dependence) were also investigated and very similar island behaviour was seen. Figure 5.4(b) shows the sawtoothing region r_m and the radial extent of the 2/1 mode as a function of α, while figure 5.4(c) plots the saturated island width, for a DITE plasma with $q_a = 3.5$. Increasing gradient of K_e allows more peaking of axial current, reduces the outer region temperatures and current gradients, and shifts the resonant surfaces out to higher radii. This has the

effect of moving the plasma from equilibria with no sawtoothing and small 2/1 islands to equilibria with sawtoothing influencing half the plasma radius and containing much larger saturated islands. The extreme case of $\alpha=5$ (with $K_e(a)/K_e(0)=760$) is unlikely to be realised in practice. It can be concluded that discharges with strongly varying anomalous electron thermal conductivities are much more unstable to tearing mode activity, with larger saturated islands obtained compared with flat thermal conductivity profiles.

5.5 *Additional Heating*

The electron and ion energy equations (2.1) and (2.2) contain additional heating terms which have been parametrised with the following Gaussian form:

$$H_{e,i}(r) = H_0 \exp\left[-\left[r-r_H\right]^2/2\sigma^2\right] \qquad (5.9)$$

with $\sigma^2 = h_w^2/(8\ln 2)$ and $P_H = 4\pi^2 R a^2 \int_0^1 r H_{e,i}(r)\,dr$

Thus $H_{e,i}(r)$ is given in terms of three parameters: (i) r_H, the position of peak applied power; (ii) h_w, the full heating width at half maximum power, and; (iii) P_H, the total additional power delivered to the electrons or ions.

Figure 5.5 plots the results of a ray-tracing calculation of the ion cyclotron resonant heating (ICRH) in a typical JET plasma [64]. Practically all the coupled power is transferred to the 10% H minority species present, and is then redistributed by collisions to give the electron and deuteron power deposition profiles in figure 5.5. The additional heating of electrons is very localised and is described well by eq.(5.9) with $h_w \approx 0.05a$. The same ray-tracing model has been compared directly with experimentally measured electron deposition profiles in JET, and good agreement is found [65].The FWHM in these comparisons were ≈60cm for on-axis heating, and ≈20cm for off-axis heating. These widths are determined by plasma quantities, and for large tokamaks can be very small, although the position of heating and total applied power can be freely varied. Parametrization with eq.(5.9) therefore provides a reasonable approximation to experimental ICRH deposition profiles, sufficient to model the effect of heating on islands.

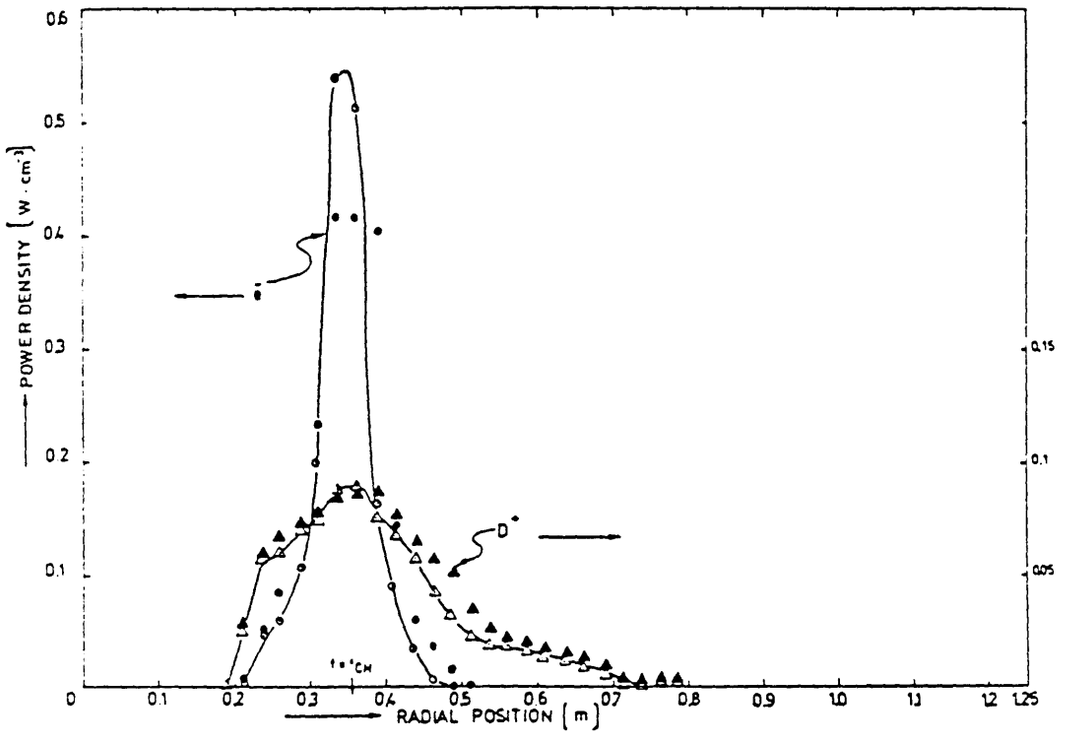

Figure 5.5 A ray–tracing calculation of the electron and deuteron power deposition profiles in a JET plasma [64].

It is proposed that if the local temperature and current gradients were sufficiently altered by additional heating then island growth could be stabilized and disruption prevented. Alternatively the heating could have an adverse effect on island stability. This question has been examined in figure 5.6, where P_H and r_H have been systematically varied in SAT. The resulting saturated island edges, resonant surfaces and mixing radii plotted in figures 5.6(a) to (d), as a function of r_h for four different choices of P_H, while (e) and (f) show the corresponding island widths and axial electron temperatures. These calculations are for a DITE plasma with $q_a = 3.5$ and additional electron heating only is assumed, with $h_w = 0.1a$. The dashed lines correspond to the case of zero heating, in which case no sawtoothing is present, and $r_{s\,2\,1} = 0.61a$. The main effects of electron heating can be summarised by:

(i) If heating is on axis then sawtoothing is initiated. The $q=2$ surface is shifted outwards and the 2/1 island reduced in size. As P_H increases so the sawtoothing region gets larger but $h_{2\,1}$ does not change.

(ii) For $r_H > 0.3a$ the sawtoothing disappears, due to the ability of the plasma to carry more outer region current. However the 2/1 island shifts inwards and becomes larger increasing it's saturation width to more than double it's original size for $r_H = 0.4a$. This radius of maximum destabilization corresponds to heating at the inner edge of the

island. The island is efficient at transporting applied energy away from the core so the amount the axial temperature increases by is greatly reduced.
(iii) If sufficient heating is applied outside the island then the outer region can increase enough so that q(0) becomes greater than 2 and no island is then present. Almost all the the additional energy supplied is lost to the wall and $T_e(0)$ is not raised significantly.

Unanswered by figure 5.6 is the question of what happens if even more power than 250kW is applied. Does the 2/1 island keep growing and finally intercept the sawtooth as seems to be suggested by figure 5.6(d). This is not the case. In figure 5.7 the heating centre r_H has been fixed at 0.1a in (a) and (b), and r_H= 0.4a in (c) and (d), while the total applied power has been scanned in SAT. It is observed in both situations that h_{21} attains some constant saturated width for large P_H, independent of P_H. For r_H= 0.4a this occurs for P_H> 300kW and equals 0.115a.

Motivated by these simulations of the saturated island behaviour, the transient island response is now examined for two heating positions: r_H= 0.4 with results in figures 5.8(a) to 5.8(c), and and r_H= 0.1 in figures 5.8(d) to 5.8(f). Once again a DITE plasma with q_a= 3.5 and electron heating only is simulated. A 250kW heating pulse is switched on instantaneously at t= 40ms after initialisation and switched off at t= 90ms. The dashed line corresponds to quantities evolving with no applied heating. In the case of r_H= 0.4a the immediate effect is to drive the 2/1 mode unstable and it attains a large maximum width of 0.15a in figure 5.8(b). After the end of heating the island undergoes a relaxation oscillations back to it's original size. The 3/2 mode is also followed in figure 5.8(a) and is also observed to go unstable but only reaches a maximum size of 0.036a before the current diffuses away from the axis and q(0) rises above 1.5. After heating the q= 1.5 surface is restored with the mode never growing. Figure 5.8(c) for comparison shows the island behaviour when heating is continuously applied and not switched off after 90ms. Large amplitude oscillations result where the maximum h_{21} is in the range (0.12a,0.14a) which agrees with the predicted saturation width in figure 5.7(d).

The axial heating case of figures 5.8(d) to (f) models what is more commonly achieved experimentally, and like experiment, giant sawteeth result. The spikes of figure 5.8(d) are the m= 1 islands, while the crosses are the sawtooth mixing radii. Between collapses the axial heating is much greater than for the ohmic case, so the electron temperature peaks much more and the subsequent collapse in T_e much greater. There is also a saturation of $T_e(0)$ during the ramp phase, compared with the

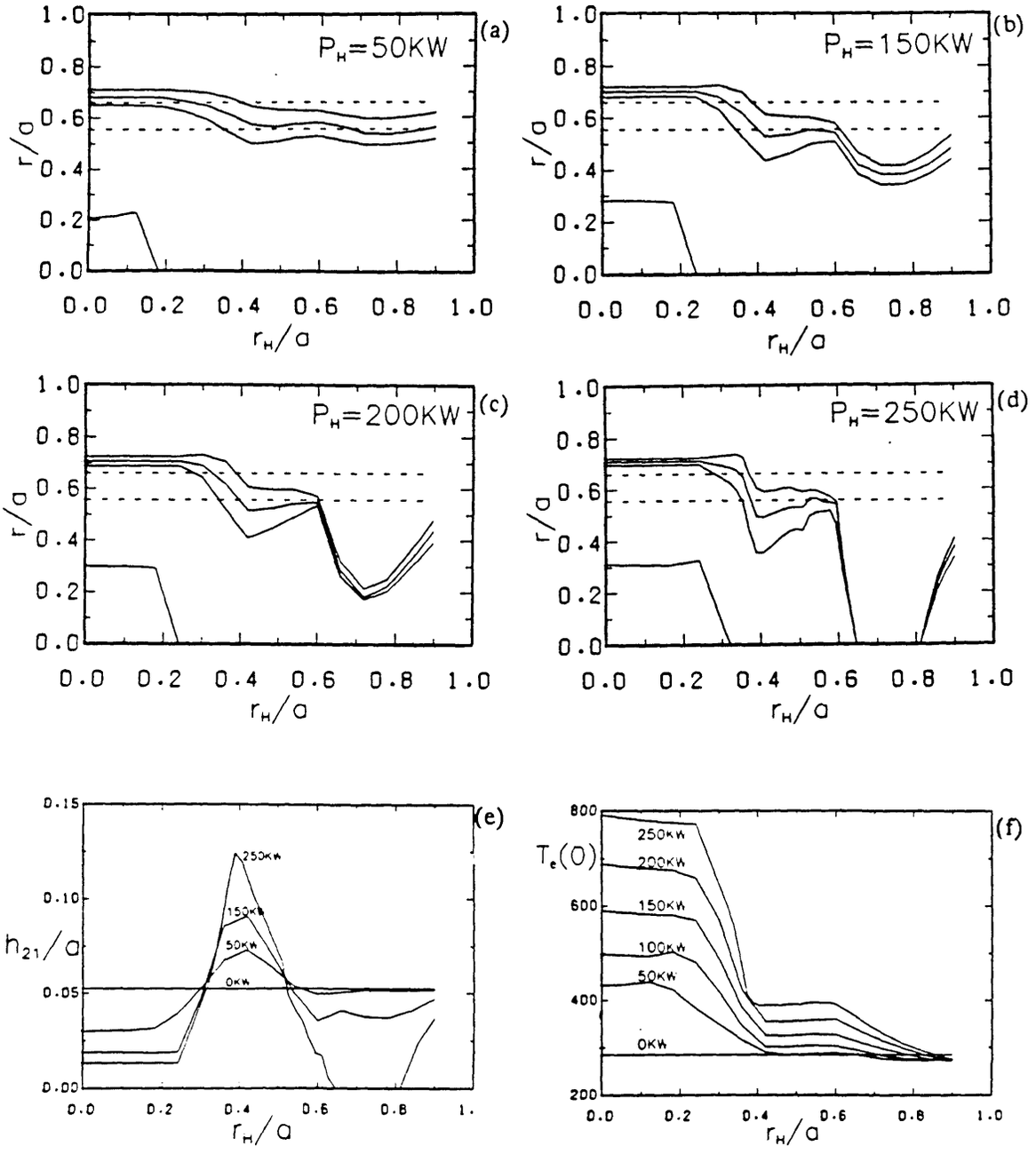

Figure 5.6 (a)–(d) The regions occupied by the saturated 2/1 island, and the sawtooth (solid lines), as a function of r_H, the position of additional Gaussian electron heating, for four choices of total applied power: 50, 150, 200, and 250kW. A DITE plasma with q_a=3.5 is modelled. Dashed lines represent the 2/1 island when no additional heating is present. (e) The 2/1 island half-width h_{21} as a function of r_H, for several choices of total applied power. (f) The corresponding axial electron temperature.

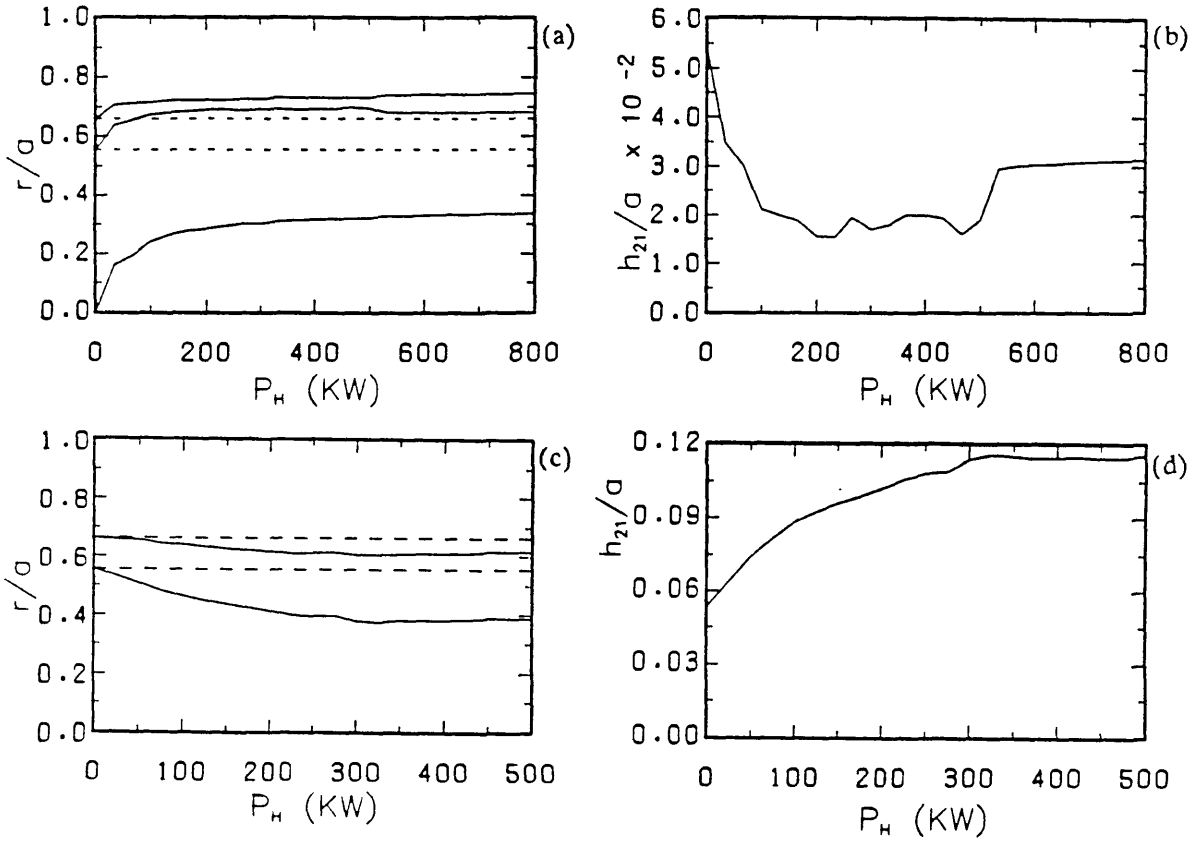

Figure 5.7 (a) and (b): The heating centre is fixed at r_H=0.1a while P_H varies between 0 and 800kW, for a DITE plasma with q_a=3.5. (a) presents the island and sawtooth regions, and also the island position for no heating (dashed lines). (b) shows the saturated width h_{21} as a function of P_H. (c) and (d): Same as above, but r_H now equals 0.4a.

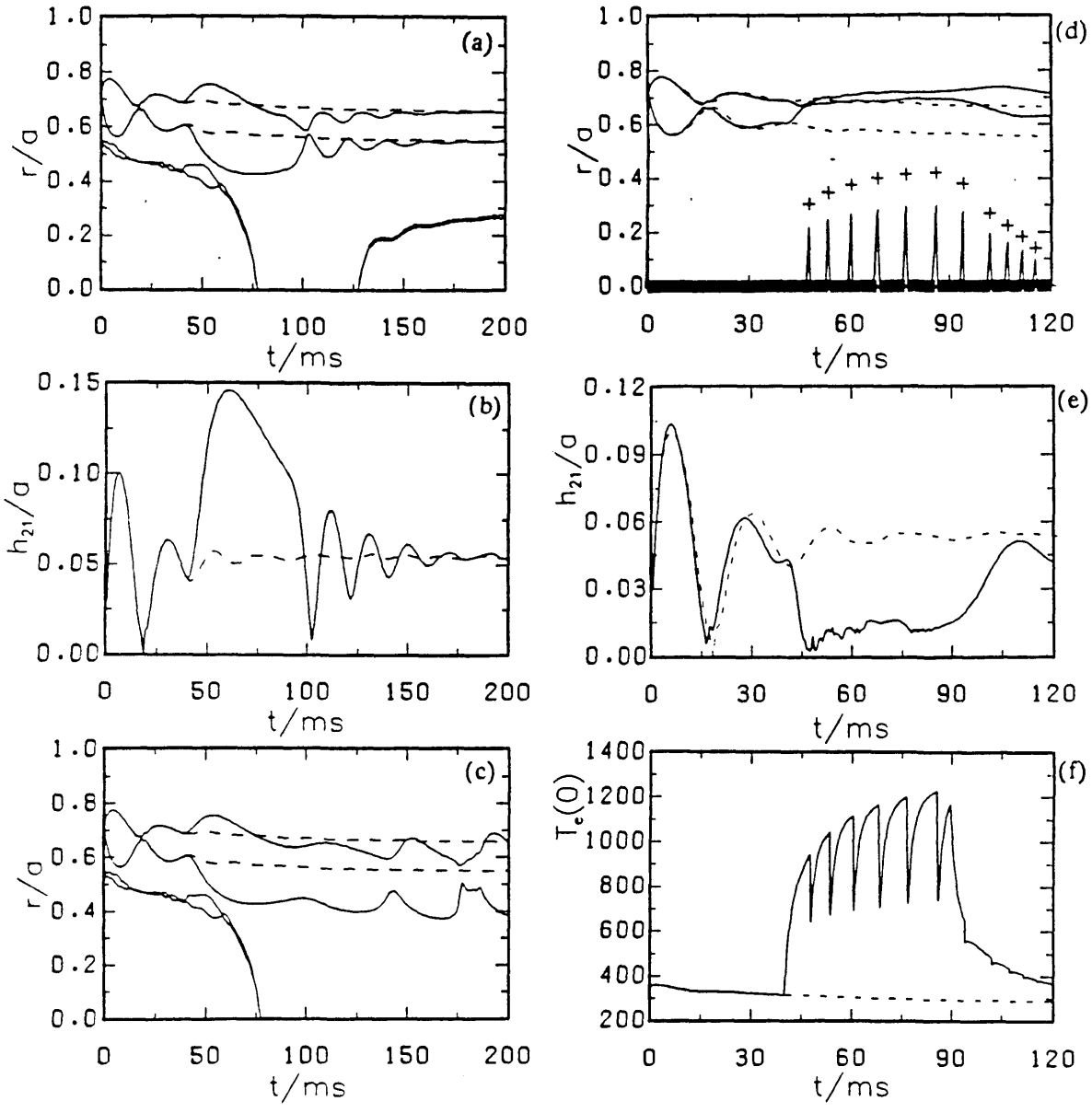

Figure 5.8 *(a) Time dependence of the 2/1 and 3/2 islands for a DITE plasma (q_a=3.5), with a 250kW heating pulse, centred at r_H=0.4a, switched on at t=40ms, and turned off at t=90ms. (b) The transient 2/1 island size of (a). Dashed line shows evolution without heating. (c) Island behaviour for an equivalent simulation to (a), but the heating is continuously applied, and not switched off at 90ms. (d) An equivalent simulation to (a) but the heating is now centred at r_H=0.1a. Spikes are the m=1 island, and crosses the Kadomtsev mixing radii. (e) Transient behaviour of h_{21} for the simulation of (d). (f) Giant sawteeth are observed in the axial electron temperature during the simulation in (d).*

linearly increasing $T_e(0)$ of the ohmic ramp phase. This is attributable to the large heat–flow associated with the steep temperature gradients of the additionally heated plasma prior to collapse. The sawtooth period is increased here to 9ms from the 4ms of figure 4.6, and this is because the sawtooth collapse with heating present is more violent and leaves q(0) much greater than 1, compared to the sawtooth collapse without heating. The plasma therefore takes longer to diffuse to a state with $q<1$. During the heat pulse the 2/1 island moves outward to a region of lower current gradient and the saturated size of 0.015a is consistent with figure 5.7(b). After heating the sawtooth gradually diminishes and disappears, and the islands revert to their original size.

5.6 *Heating in JET*

DITE is a small tokamak which with present–day thermal conductivities will never achieve the 10keV necessary for fusion. SAT is now used for plasmas of JET dimensions to examine island dependencies and to see to what extent the results of figures 5.7 and 5.8 will scale up to larger plasmas. Figures 5.9(a)and (b) therefore give the island and sawtooth regions, and the island size as a function of applied heating position r_H, for $q_a= 3.5$, total applied power= 4MW and heating width $h_w= 0.1$a. The solid lines as before correspond to electron heating only, while the dashed lines are with no electron heating, but the same Gaussian profile for ion heating $H_i(r)$ in the ion energy equation. Figure 5.9(c) shows the axial temperature for the electron–heating, and figure 5.9(d) with ion heating. Considering now the $H_e(r)$ case, the 2/1 island and the sawtoothing region behave identically to the DITE plasma, but with the position of r_H for maximum h_{21} now equal to 0.45a. If ion heating is applied it's influence on the islands is indistinguishable from H_e for small r_H, but becomes less drastic as r_H moves away drom the axis. The maximum h_{21} is 0.09a compared with 0.12a for H_e, and it is not until $r_H= 0.7$a that the mode is completely stabilized by heating driving q(0) above 2.

Figure 5.10 plots the same quantities as in figures 5.9(a) and (b), but here r_H is fixed at 0.1a, while the total power applied has been scanned to 8MW. There are no qualitative differences between these JET results and the DITE results of figure 5.7(a), and the island sizes are the same for both H_e and H_i.

As SAT simulations use the averaged sawtooth model, the temperatures obtained in figures 5.9(c) and (d) also correspond to an averaged temperature. With axial

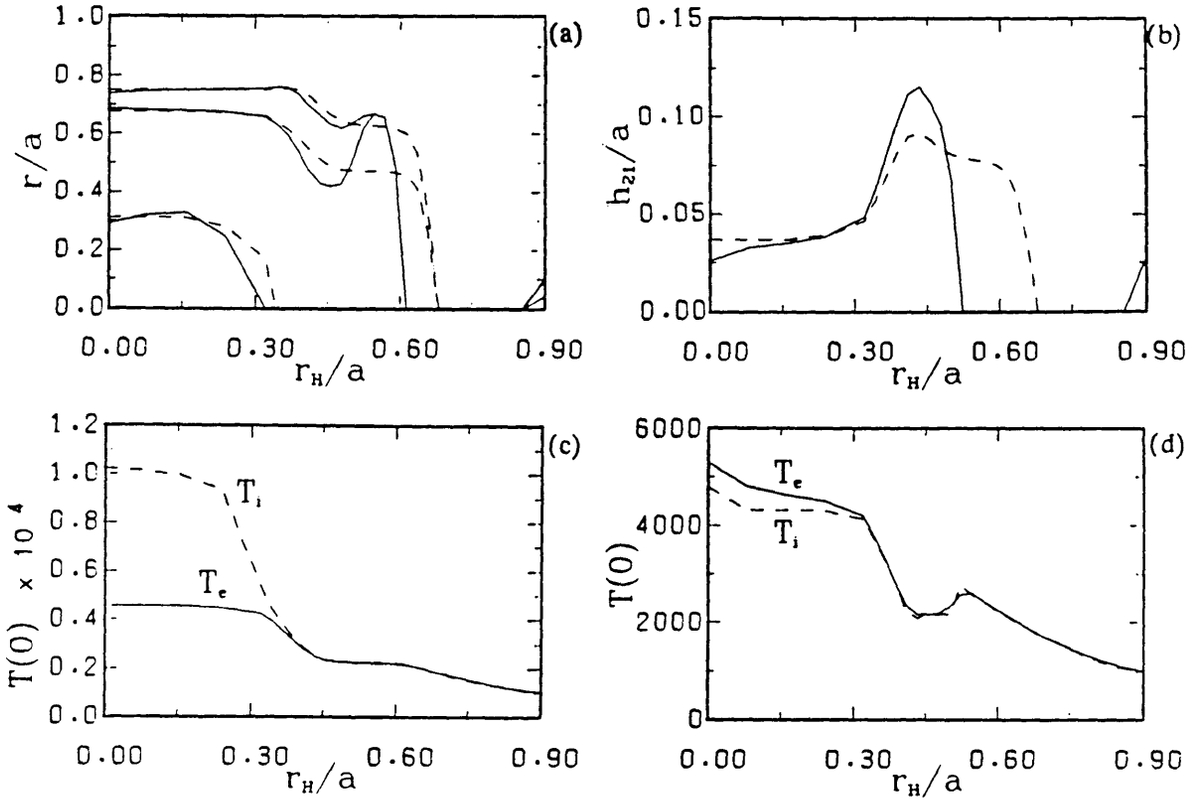

Figure 5.9 (a) Response of the island and sawtooth regions to additional heating of a JET plasma with q_a=3.5, for P_H=4MW and r_H varying between 0 and 0.9a. Solid lines are for electron heating only, and dashed lines for ion heating only. (b) 2/1 island sizes calculated in (a). (c) Axial electron and ion temperatures for applied H_e. (d) Axial temperatures for applied H_i.

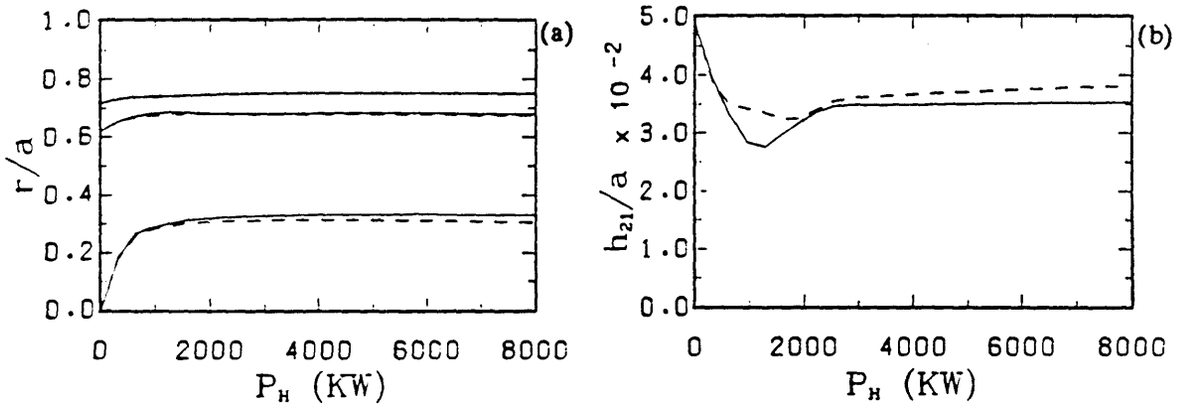

Figure 5.10 P_H is varied between 0 and 8MW for a JET plasma with q_a=3.5, and r_H=0.1a. (a) shows the island regions, (b) the magnitude of h_{21}. Solid lines are for electron heating, and dashed lines for ion heating.

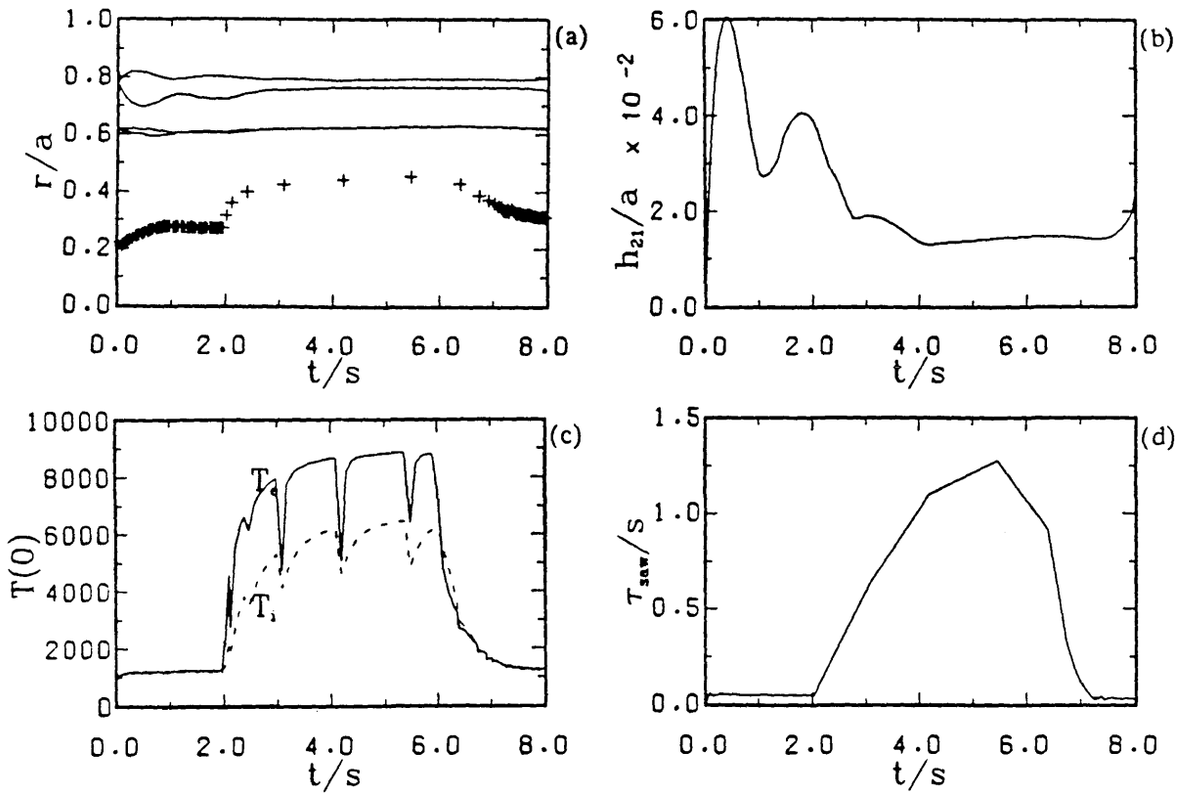

Figure 5.11 *Transient behaviour of a JET plasma (q_a=3.5) for 4MW of electron additional heating centred at 0.1a, and applied between 2 and 6s. (a) to (c) show respectively the island regions, the island size h_{21}, and the axial temperatures. (d) plots the sawtooth period as a function of time. τ_{saw} increases from 55ms to 1.25s with the TRID sawtooth model*

heating, "monster" sawteeth in fact result and determine the actual peak temperatures achieved. Figure 5.11 presents such a JET simulation with $q_a = 3.1$ and with a electron-heating pulse of 4MW, centred at $r_H = 0.1a$, applied between t= 2s and t= 6s. The peak T_e between collapse increases to 9keV, the sawtooth period increases from 55ms to 1.25s, and there is a small reduction in h_{21}.

The conclusion from this study of heating effects on island growth can be summarised by:

(i) Heating on axis, or well inside the q= 2 resonant surface gives rise to giant sawteeth and a reduction in saturated size of the 2/1 island.

(ii) Heating at or just inside the resonant surface strongly destabilizes the island. Saturated sizes 2.5 times greater are observed.

(iii) Heating outside the island can allow q(0) to rise above 2 and so remove the 2/1 mode.

5.7 *Ballooning Mode Investigation*

In the simulation of Bondeson [23], large sawteeth, as previously seen in section 4.7, were observed, with $T_e(0)$ dropping from 245eV to 155eV. In TRID this behaviour is termed a disruption, while [23] on the other hand continued simulation that showed the "shock-front" stopping, and recovery of the plasma to give further giant sawteeth. Bondeson proposed that at the shock-front prior to disruption, the steep pressure gradients found there would be strongly unstable to ideal ballooning modes. These modes are excluded from [23] as toroidal and pressure driven effects are neglected in reduced MHD. The effect of a ballooning instability would be to rapidly erode these steep gradients and bring about strong interaction between the hot central region and the cold island-dominated exterior, giving the total thermal quench and broadening of current that [23] did not give.

Hopcraft et al. [20] tested for high-n localised ballooning mode instability in TRINIO using a criterion due to Lortz and Nührenberg [66]. This criterion is:

$$S_b > \gamma_1 \alpha_b^2 \text{ for stability, where:} \qquad (5.10)$$

$$\gamma_1 = \frac{3}{4}(1+1/\sqrt{2}) = 1.28 \qquad (5.11)$$

$$S_b = rq'(r)/q(r) \qquad (5.12)$$

$$\alpha_b = \frac{-2Rq^2\mu_0 p'}{B_z^2} \qquad (5.13)$$

and is valid for circular flux surfaces in the limits $\epsilon = r/R \to 0$, $S_b \to 0$, and $\alpha_b \to 0$ and so is strictly correct near the axis. No instability was reported in [20], which is somewhat surprising as eq.(5.10) predicts instability for shear S_b going to zero.

This section also tests for ballooning instability but uses both eq.(5.10), and also an alternative criterion [67]. The explicit modelling of the sawtooth, and the two fluid nature of TRID give more realistic profiles of shear S_b and pressure gradient α_b, and so give quite different results to [20]. This criterion obtained from analytic solution for the ballooning mode eigenfunction, valid for large aspect ratio and circular cross-section, is given by:

$$F[S_b,\alpha_b] \equiv S_b^2 + 2\alpha_b\left[\epsilon\left[1-\bar{q}^2\right]-\frac{7}{4}\left[1-\frac{5}{7}S_b^2\right]e^{-1/|S_b|}\right] - \frac{3}{2}S_b\alpha_b^2 > 0 \qquad (5.14)$$

For $\epsilon \to 0$ and $S_b \to 0$, this reduces to a quadratic; $S_b > 1.5\alpha_b^2$, which gives a greater chance for ballooning instability than eq.(5.10). Figure 5.12(a) is a repeat of the current-limit disruption simulation in figure 4.14, but only the island evolution after t= 50ms is plotted (t= 0 in fig. 5.12(a)). The points labelled "x" correspond to the sawtooth mixing radii, the additional solid line inside r_m is the q= 1 surface, while the shaded areas bounded by "+" show regions of the plasma that fail to satisfy eq.(5.14). With steady sawtoothing until 55ms there is always a low-shear region between the axis and some radius inside q= 1 that can be expected to be ballooning mode unstable. After 55ms, when both r_m and the island regions are large, a second narrow region of instability arises. This is not due to steep pressure gradients, but in fact corresponds to a second low-shear region arising as a result of the sawtooth redistribution of profiles. When eq.(5.10) is used as a ballooning criterion, similar regions to those in figure 5.12 are observed, although they are generally larger in size.

Figure 5.12(b) plots $F(S_b,\alpha_b)$ at t= 57.5ms as a function of r. The outer ballooning-unstable region is clearly visible where F< 0. F is also less than zero for r< 0.12a this is not evident on this scale. After the sawtooth collapse at 58ms the axial ballooning-unstable region disappears, and this is because the post-collapse q profile now evolves into one with slight negative shear in this region. The narrow region at 0.42a has approximately zero shear so F< 0. Just prior to the final sawtooth collapse another narrow (two grid points here) ballooning-unstable region at 0.59a can be observed. This still does not arise through large $|p'|$, but appears because a small

partial sawtooth collapse occurs at this time, flattening q(r) here. It is conceivable that instability at this time could then speed interaction between the inner and outer plasma as earlier proposed. However the hypothesis of [23] that ever increasing $|p'|$ would lead to ballooning instability is not borne out by TRID, as all instances at which it is predicted here are for low-shear, post-collapse q profiles. These profiles of course depend delicately on the Kadomtsev prescription, and the doubts concerning the sawtooth mechanism must therefore apply to these predicted ballooning mode regions.

It can be concluded from this section that:

(i) Steep pressure gradients when islands are large do not initiate ballooning instability.

(ii) It is the particular form of the post-collapse q(r) profile that is critical in determining ballooning instability.

(iii) With the Kadomtsev prescription, narrow, low-shear ballooning-unstable regions inside the $q=1$ surface arise that could hasten the interaction between the hot, inner region, and the cool, island-dominated outer plasma. Larger ballooning unstable regions are predicted on axis during steady sawtoothing.

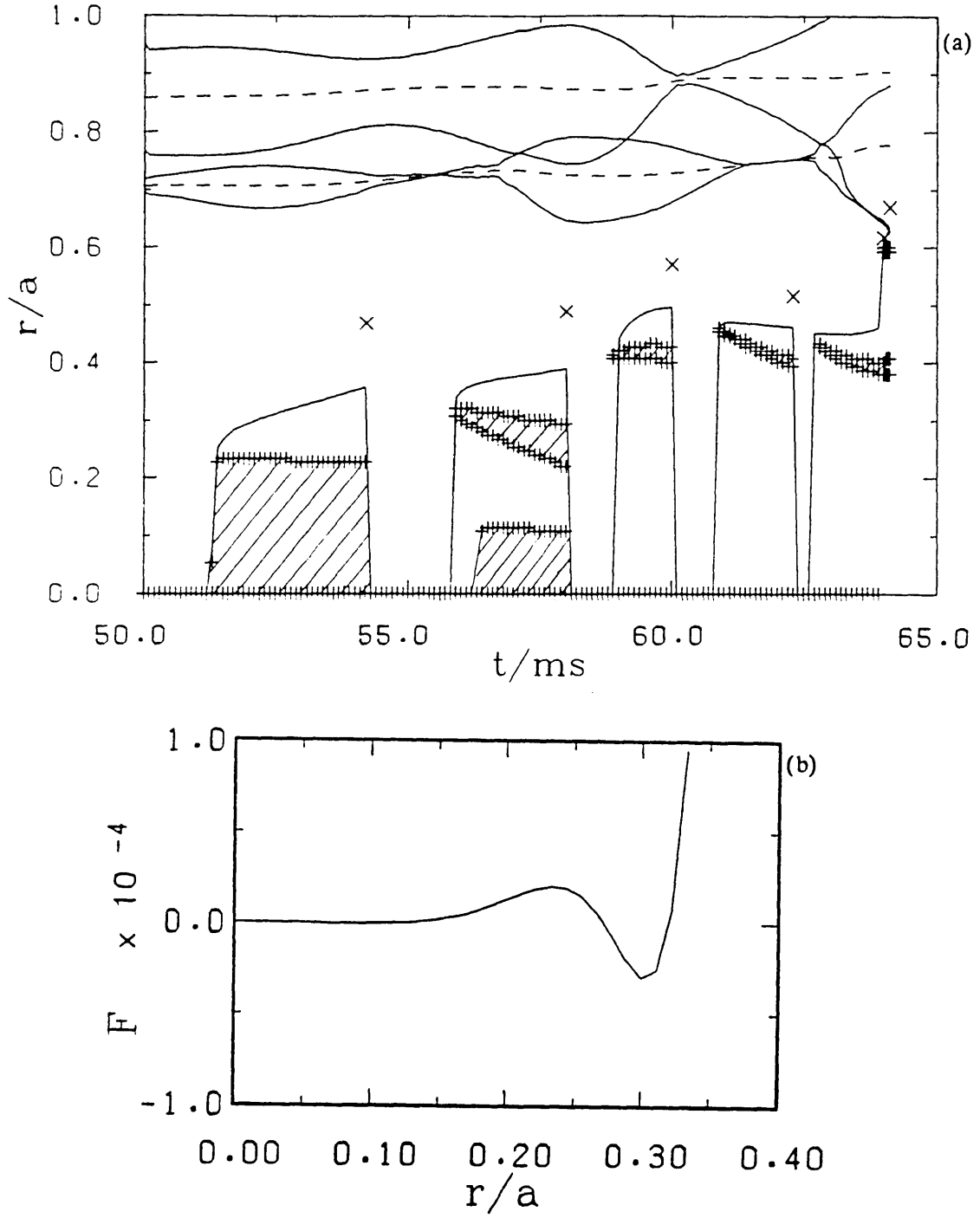

Figure 5.12 (a) A repeat of the simulation in figure 4.14, starting from t=50ms. The ballooning criterion eq.(5.11) is tested, and shading shows the predicted regions of ballooning instability. (b) The radial dependence of $F(S_b,\alpha_b)$ at t=57.5ms. Instability corresponds to F<0.

CHAPTER SIX

RADIATION AND DISRUPTIONS

6.1 *Introduction*

No present–day tokamaks operate free from impurities, and impurity radiation generally accounts for between 50 and 100% of the electron energy loss [68]. In this chapter a hydrodynamic–coronal model is implemented in TRID to give the radiation losses from oxygen impurities. Sudden impurity influx, and density–ramp simulations are made and radiative contraction of the outer plasma is observed prior to disruption. A simple fitted profile for the radiated loss is used to examine the variation in density limit with current under various assumptions, and good agreement between the resulting Hugill diagram and experimental density limits is obtained.

6.2 *Hydrodynamic–Coronal Model for Tokamak Impurity Radiation*

A hydrodynamic–coronal model for the impurity ions is used in TRID to calculate the radiation loss term P(r) in eq.(3.22). It is similar to Roberts [68] but is not steady–state. In low density tokamak plasmas the rates of radiative decay to lower levels are much greater than the collisional rates of excitation, so coronal equilibrium is set up with a balance between collisional ionization and recombination processes. The radiated power for each ionization stage of the impurity is a combination of four processes:

(i) Bremsstrahlung radiation produced when an electron makes a free–free transition when colliding with an ion.

(ii) Radiative recombination radiation due to radiative capture of a free electron into a bound state.

(iii) Dielectronic recombination radiation produced when a free electron with energy just below threshold for excitation of a bound electron collides with an ion. The excitation still occurs but the once free electron has insufficient energy for escape and is also captured. The excited and captured electrons radiatively decay to lower levels.

(iv) Line radiation produced from the spontaneous radiative decay of excited ions into their ground state.

All the above processes give rise to a radiation intensity that is given as the product of the electron density, the impurity density, and some atomic coefficient depending on ionization state z and temperature. Formulae for the various terms are given in [69]. It will be found later that the dominant term contributing to radiation cooling is the line radiation from the lower ionized states that are localised in the cooler plasma edge. The expression for the power density emitted as line radiation is given by:

$$P_l = 1.6\times10^{-19} n_e n_z \sum_j Q_j \Delta E_j \quad Wm^{-3} \tag{6.1}$$

where Q_j is the excitation-rate coefficient and the summation extends over the transitions given in [69].

The impurity ion distributions $n_z(r)$ in eq.(6.1) are now calculated. Numerous experiments [68 and refs. therein] on different machines have shown that an anomalous impurity transport is necessary to account for measured radiation losses. Therefore for a particular impurity species, a system of diffusion equations in cylindrical geometry for the $n_z(r)$ is solved:

$$\frac{\partial n_z}{\partial t} = \frac{-1}{r}\frac{\partial}{\partial r} r\psi_z + n_e\left[S_{z-1} n_{z-1} - S_z n_z - \alpha_z n_z + \alpha_{z+1} n_{z+1}\right] \tag{6.2}$$

ψ_z is the radial flux of impurity ions of charge z, and S_z and α_z are the ionization and recombination rates (given in [69]), and are strong functions of electron temperature. Uncertainties in the atomic coefficients are expected to give rise to a factor of two inaccuracy in the power profiles. There are nine coupled equations in this system in the case of oxygen (and 27 for iron for example). It is assumed in TRID simulations that oxygen is the only impurity present. It is usually the dominant light impurity observed in tokamaks [61], but in any case the radiated power profiles versus temperatures for other light impurities such as carbon or nitrogen are very similar to oxygen. It is not justified to neglect heavy impurity ions like iron which are commonly observed, and which have quite different power profile characteristics. At typical tokamak temperatures Fe is still incompletely ionized even in the hot core, so the heavy ion radiation cooling is peaked on axis, unlike that from light impurities which is strongly localized at the plasma edge. Here the question of heavy impurities is left to future study as the computational cost of solving large numbers of coupled equations becomes prohibitive, and the presence of two or more impurities could mask their respective effects on island growth and make the simulation unduly complicated.

The boundary conditions for eq.(6.2) are $dn_z/dr = 0$ for $r = 0$, and $n_z(a) = 0$ for $z > 0$. The neutrals are assumed to have some specified density $n_0(a)$ at the limiter, and to penetrate the plasma with a constant velocity v_{ox}, where v_{ox} is the velocity of a thermal atom with an energy of 1eV. Finally the impurity fluxes ψ_z are defined:

$$\psi_z = -n_0(r)v_{ox} \text{ for } z=0, \qquad \psi_z = -D\frac{\partial n_z}{\partial r} \text{ for } z=1..8 \tag{6.3}$$

where D is some constant anomalous diffusion coefficient, taken to be 0.5 m^2s^{-1} in TRID. Any contribution of neoclassical flux to eq.(6.3) has been neglected, as most present-day experiments indicate that anomalous diffusion is predominant. Scaling of D with plasma parameters is not well understood so the simplest case of constant D is used, except in the island regions where D is enhanced by a large amount as for the thermal conductivity.

Charge exchange collisions betwen ionized impurities and neutral deuterium (and also the opposite reaction) are neglected in eq.(6.2). They have the effect of increasing the penetration depth and recycling of neutral oxygen [81]. In ref. [82], by varying the neutral oxygen penetration energy between 0.2 and 10eV, it is shown that there is negligible effect on the power loss from O^{3+} to O^{8+}, while for the lower states it is increased by a factor of 2-3. However the radiation from these states also depends sensitively on $n_e(r)$ which is fixed in TRID. Therefore the inclusion of charge exchange processes, which also entails a modelling a neutral deuterium, is left for further work. The radiation model implemented here is still expected to describe the main features of low-Z impurity radiation, and it's interaction with magnetic islands.

When differenced system (6.2) can be cast it into a 9×9 block tridiagonal form which is simply inverted using the recursive method of Appendix B. Upwind differencing of the first order equation for n_0 ensures diagonal dominance of the matrices and stability of the recursive method. Centre differencing the diffusion terms, then eq.(6.2) with $z = 0$ becomes, for $i = 1, N-1$:

$$b_i n_{0,i}^{n+1} + c_i n_{0,i+1}^{n+1} + e_i n_{1,i}^{n+1} = w_{0,i} \tag{6.4}$$

with coefficients:

$$b_i = -1 - p_0 S_{0,i} n_{e,i} - p_1, \quad c_i = r_{i+1}/r_i, \quad e_i = p_0 \alpha_{1,i} n_{e,i},$$

$$w_{0,i} = -p_1 n_{0,i}^{n}, \quad p_0 = n_D S_0 t_0 D, \quad p_1 = D/(v_{0x}\Delta t)$$

and for z=1...8:

$$A_i n^{n+1}_{z,i-1} + B_{z,i} n^{n+1}_{z,i} + C_i n^{n+1}_{z,i+1} + D_{z-1,i} n^{n+1}_{z-1,i} + E_{z+1,i} n^{n+1}_{z+1,i} = w_{z,i} \qquad (6.5)$$

with matrix coefficients defined by:

$$A_i = r_{i-1} D_{i-1}/r_i, \quad C_i = r_{i+1} D_{i+1}/r_i, \quad B_{z,i} = -A_i + C_i + D_{z,i} + E_{z,i} + p_3,$$

$$D_{z,i} = p_2 n_{e,i} S_{z,i} \quad E_{z,i} = p_2 n_{e,i} \alpha_{z,i} \quad w_{z,i} = -p_3 n^n_{z,i}$$

$$p_2 = n_D S_0 a^2 \Delta^2 / D \quad p_3 = a^2 \Delta^2 / D t_0 \Delta t$$

For given $T_e(r)$, $n_e(r)$, and a given neutral density at the wall $n_0(a)$, eqs.(6.4) and (6.5) can be solved, and using the expressions in ref.[69], such as eq.(6.1), the power loss profile at time t^{n+1} can be calculated.

Figure 6.1 compares two steady–state (d/dt= 0) radiated power calculations for a DITE plasma. The density is assumed Gaussian and given by eq.(3.29), with $n_D = 3\times10^{19} m^{-3}$, $n_e(0) = 2n_D$, and other relevant parameters are a= 0.26m, $D = 0.5 m^2 s^{-1}$, and $n_0(a) = 3\times10^{15} m^{-3}$, T_{ea}= 5eV, and $T_e(0)$= 400eV. All dashed lines correspond to a Gaussian electron temperature profile

$$T_e(r) = T_{ea} + (T_e(0) - T_{ea}) \frac{e^{-\sigma r^2} - e^{-\sigma}}{1 - e^{-\sigma}} \qquad (6.6)$$

with σ= 2, while solid lines represent calculations for an idealised temperature profile with both sawteeth and a 2/1 island present. A small temperature difference across the island regions $(0, r_m)$ and (r_1, r_2) of 5eV is assumed, with a constant temperature gradient elsewhere. Such an idealised profile is an approximation to those observed with TRID simulations such as in figure 3.2. The temperature of the island, T_{isl}, is assumed to be that of the Gaussian at the outer edge r_2. Figure 6.1(a) shows both of these profiles, with $r_m = 0.4a$, $r_{21} = 0.7a$ and $h_2 = 0.1a$. In figures 6.1(c) and (d) the radial profiles for the various ionized states are plotted for the island–modified and the Gaussian T_e profiles respectively. Progressing from the limiter inwards the densities peak at some radius which moves into the plasma as z increases. The effect of anomalous diffusion is to shift the peak densities of the lower states deeper into more dense plasma where they radiate more strongly than in pure coronal (D= 0) equilibrium. The dashed line of figure 6.1(e) shows the radiated power/unit volume as a function of radius for the Gaussian T_e profile. For the relatively low temperatures near the edge, and even for the core temperatures of a DITE plasma, the line

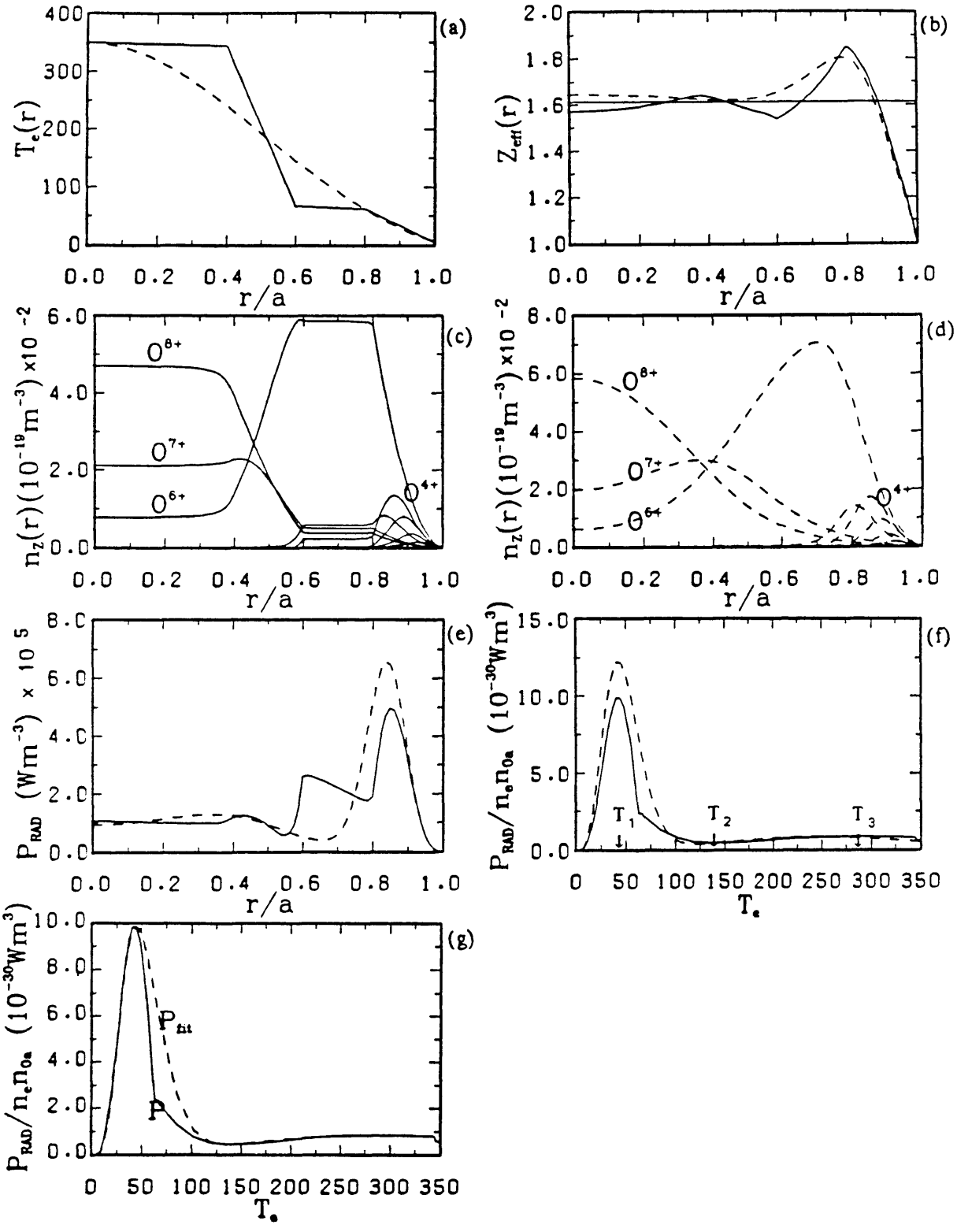

Figure 6.1 *Comparison of two radiated power calculations for a DITE plasma. All solid lines correspond to the island-flattened profile of (a), and dashed lines to the Gaussian $T_e(r)$. (b) Radial profiles and averaged value for Z_{eff}. (c) and (d) The radial distributions of the ionized states of oxygen impurity. (e) Radial profiles of radiated power. (f) Normalised power loss as a function of T_e. (g) Comparison of the fitted curve, eq.(6.8), to the actual power loss in (f).*

radiation comprises almost all the radiation losses. The peak near the edge is associated with excitation of line radiation from ions up to O^{5+}. The minimum near r= 0.65a is due to most of the ions at this radius being O^{6+} (He–like) which are not easily excited at outer region temperatures. With islands present flattening of the $n_z(r)$ profiles is naturally observed. Although the actual peak densities achieved in figure 6.1(d) are less, so the radiation peak is smaller, the larger fraction of lower ionized states across the island means the radiation at these radii is greater, and the total losses are also larger. The shape and magnitude of the axial temperature has little influence on the edge radiation profile and the total losses.

The presence of impurities will also give rise to an increase in ohmic heating, due to their raising Z_{eff}, the effective charge of the plasma:

$$Z_{eff}(r) = [n_i + \Sigma n_z z^2]/[n_i + \Sigma n_z z] \qquad (6.7)$$

which is substituted into the Spitzer–Harm resistivity, eq.(3.25). Typically with $n_0(a)= 2\times10^{-4} n_D$, Z_{eff} increases to somewhere in the range 1.5 to 2.0. It is the highly ionized heavy impurities that have been neglected that give rise to Z_{eff} of 3–5 frequently observed. In figure 6.1(b) the $Z_{eff}(r)$ is plotted for both temperatures profiles, with little difference observed between them, while the constant value 1.61 plotted here is the resistance–averaged Z_{eff} [68] for the Gaussian temperature.

6.3 *A Curve–Fit for Steady–State Radiation Loss*

The radiation calculation described above is very time–consuming, especially when losses are large and the timestep becomes limited by eq.(3.38) to small values. Therefore an algebraic form is fitted to the loss curve that will accurately represent the steady–state radiation over a large range of conditions. In figure 6.1(e) the two forms for P(r) are quite different; it is not possible to represent them with the same general form. However in figure 6.1(f) power loss, normalised by density, $P_T(T)= P(r)/n_e(r)n_0(a)$ Wcm^3, is plotted as a function of temperature. Both forms are now very similar, the islands have only a small effect on P_T, and for a variety of simulations with varying parameters (eg $n_e(0), T_e(0), T_{isl}, r_{21}$) the widely separated twin–peak shape for P_T is quite general. P_T can be described in terms of six parameters: P_1 and P_3 are the maxima of P_T at T_1 and T_3 respectively and P_2 the minimum at T_2. The functional form fitted to P_T is:

$$P_f(T) = aT^b\exp(-bT/T_1) + cT^d\exp(-cT/T_3) \qquad (6.8)$$

here a, b, c, d are constants to be determined. If T_1 and T_3 are widely separated as in figure 6.1(f) then the maxima of $P_f(T)$ simply correspond to T_1 and T_3, so $P_1 = aT_1^b\exp(-b)$, and similarily for $T = T_3$. Requiring a minimum at $T = T_2$, the determination of a to d in eq.(6.8) reduces to finding B, the root of:

$$F(B) = b(1-T_2/T_1)B + d(1-T_2/T_3)(P_2-B) = 0 \qquad (6.9)$$

where

$$b = \frac{\ln(B)/P_1}{1-T_2/T_1+\ln(T_2/T_1)}, \quad d = \frac{\ln(P_2-B)/P_3}{1-T_2/T_3+\ln(T_2/T_3)}, \quad B = aT_2^b\exp(-bT_2/T_1)$$

$P_f(T)$ has been fitted to the solid curve in figure 6.1(f) and the comparison between it (dashed line) and the actual loss is shown in figure 6.1(g). $P_f(T)$ in this case overestimates $P_T(T)$ slightly in this case, but as the ionization cross-sections are accurate to a factor of two, this difference, which is less than this, is not important.

Before $P_f(T)$ can be used, the variation of $P_1..P_3$, $T_1..T_3$ and also Z_{eff} must be calculated over a wide range of plasma conditions. At each timestep in a TRID simulation, area-weighting then interpolates to find the P_1 etc for the particular plasma quantities at this time, and $P_f(T)$ evaluated with eq.(6.8). This procedure allows a large saving in computational time, simulations of density-limit disruptions, and an examination of the disruption behaviour in response to variation of radiation parameters. The scan of radiation parameters is made with the Gaussian $n_e(r)$ profile, with variable n_D, and with the electron temperature parametrized by the island-modified profile of figure 6.1(a), but with a quadratic dependence for $r < r_1$, i.e.:

$$\begin{aligned} T_e(r) &= T_e(0)-[T_e(0)-T_e(r_{s1})](r/r_1)^2 && 0<r<r_1 \\ &= T_e(r_1)-[T_e(r_1)-T_e(r_2)](r-r_1)/(r_2-r_1) && r_1<r<r_2 \\ &= T_e(r_2)-[T_e(r_2)-T_{ea}](r-r_2)/(1-r_1) && r_2<r<1 \end{aligned} \qquad (6.10)$$

here $r_1 = r_2-2h_{21}$, $T_e(r_2) = T_e(r_{21})-2.5$

$r_{21} = r_2-h_{21}$, $T_e(r_1) = T_e(r_{21})+2.5$

Variation in the five independent quantities, n_D, $T_e(0)$, $T_e(r_{21})$, r_2 and h_{21}, over suitable ranges should represent all the possible $T_e(r)$ that arise during during a TRID

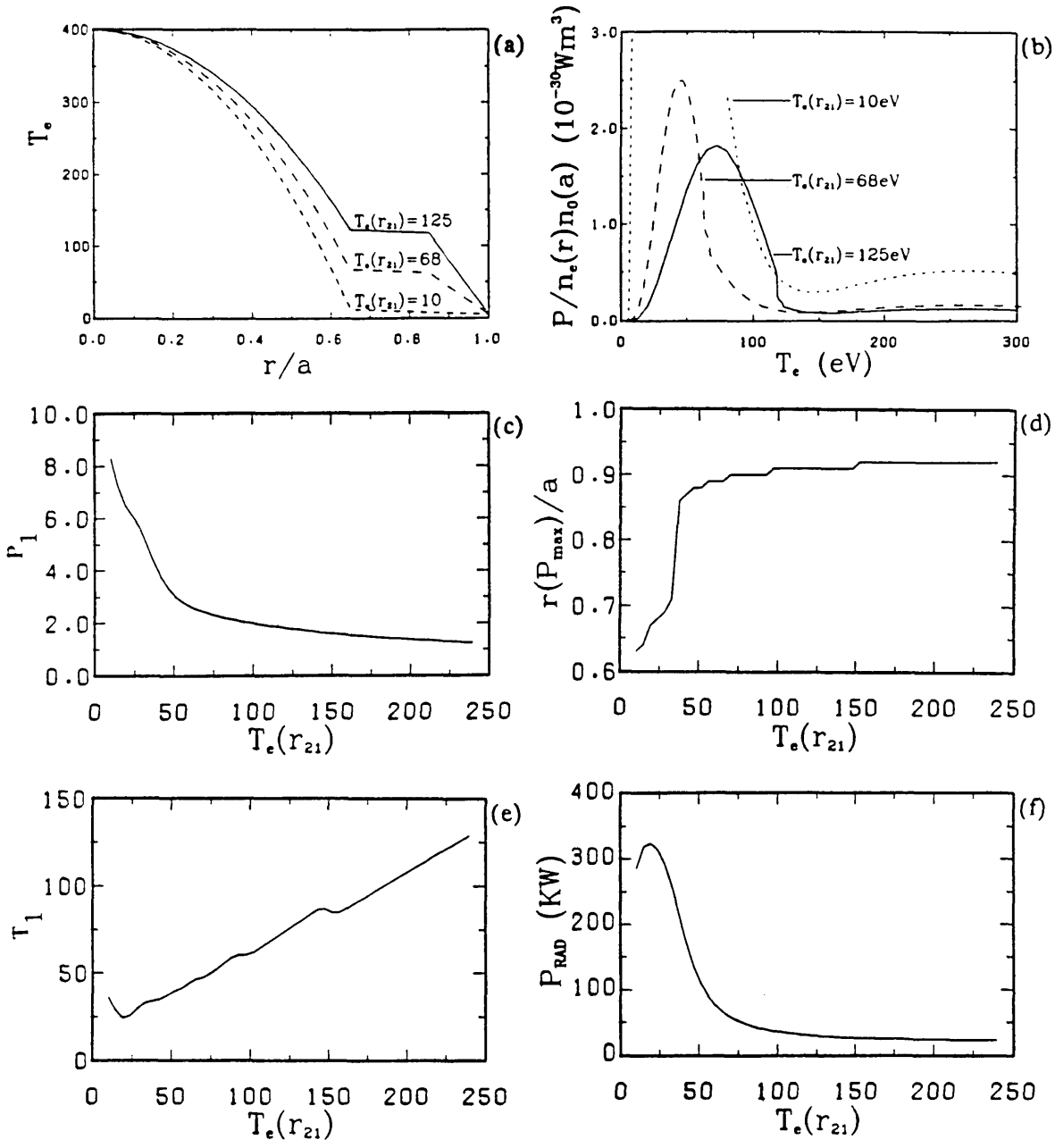

Figure 6.2 The effect of island cooling on radiated power loss. (a) Three representative island–flattened electron temperature profiles. (b) The corresponding normalised power loss as a function of T_e. (c) Maximum value of (b) as a function of the island temperature. (d)–(e) The position and temperature respectively at which the peak power loss in (b) occurs, as a function of $T_e(r_{21})$. (f) The total radiated power for $T_e(r_{21})$ varying.

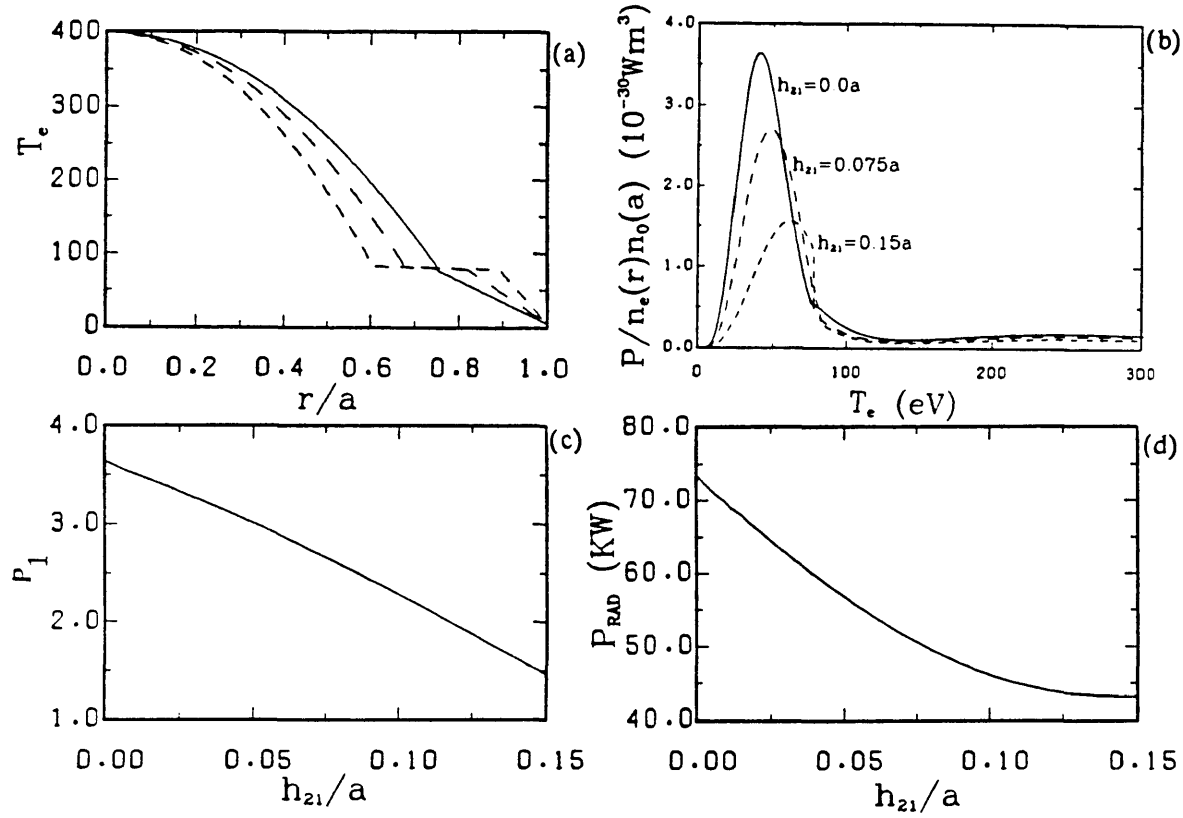

Figure 6.3 *The effect of island width (at constant $T_e(r_{21})$) on radiated power. (a) Three $T_e(r)$ profiles with h=0.0, 0.075a, and 0.15a. (b) The corresponding normalised power loss as a function of $T_e(r)$. (c) The maximum value of (b) as a function of h_{21}. (d) Total radiated power as a function of h_{21}.*

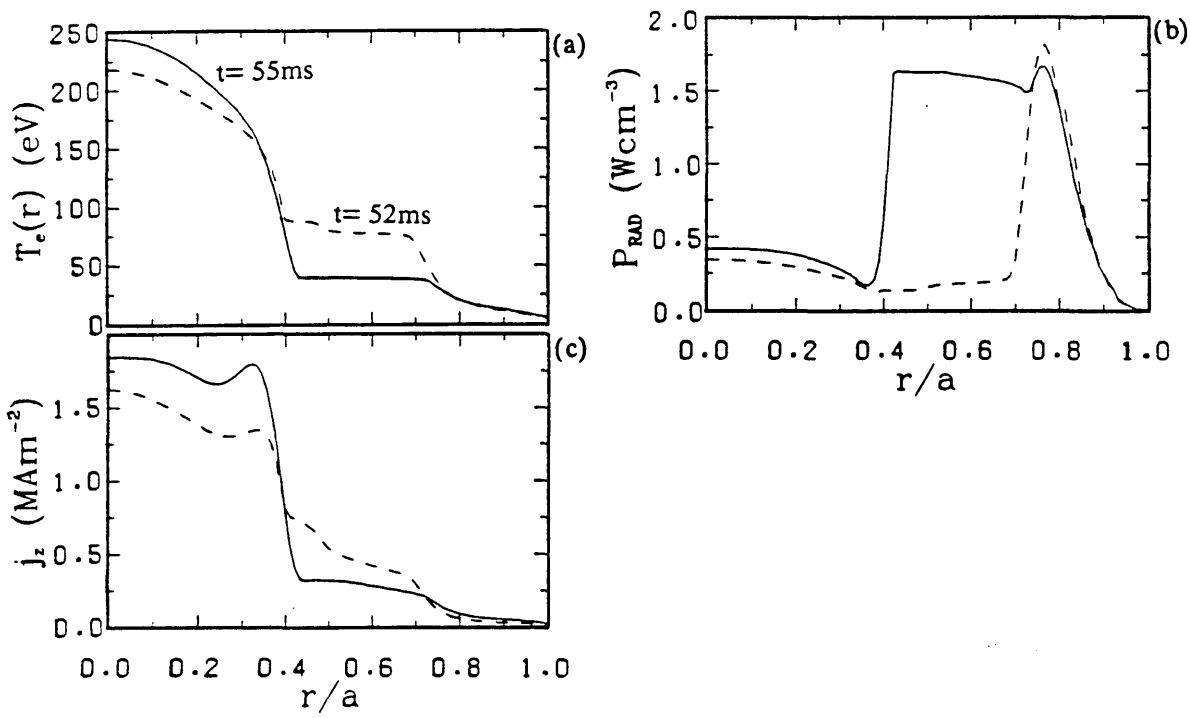

Figure 6.4 *Radial profiles of (a): electron temperature, (b): radiated power, and (c): current, during the radiative collapse simulation of figure 6.5. Profiles are plotted at t=52ms (dashed lines), and t=55ms (solid lines).*

simulation. For example for DITE

n_D = 1, 3, 5, $7\times10^{19}m^{-3}$

$T_e(0)$ = 200, 300, 400, 500eV

$T_e(r_{21})$ = 10, 40, 70... 190eV

r_2/a = 0.35, 0.48, 0.60, 0.73, 0.85, 0.98

h_{21}/a = 0.00, 0.05, 0.10, 0.15

are chosen.

The idealised temperature profiles of eq.(6.10) are used in figure 6.2 and 6.3 to gain some understanding of how the radiation profiles vary in response to the island. The axial temperature is fixed at 400eV, $n_0(a)/n_D = 3\times10^{15}/3\times10^{19}$, the 2/1 island has r_1 and r_2 specified to be 0.65a and 0.85a, while the island temperature is free to vary. Figure 6.2(a) shows three such profiles for $T_e(r_{21})=10$, 68, and 125 eV. and (b) shows the corresponding $P_T(T)$ profiles. The maximum value P_1 of (b) is plotted as a function of $T_e(r_{21})$ in (c) while the temperature T_1 and radial position r_p at which this maximum occurs are plotted in (d) and (e). Finally in (f) the total radiated power as a function of $T_e(r_{21})$ is given. For $T_e(r_{21})>70$eV the radiation losses are largely insensitive to $T_e(r_{21})$, although T_1 decreases linearly as cooler islands are considered. When $T_e(r_{21})$ approaches T_1 the radiation begins to cool the island, the densities of the lower ionized states increase strongly in the island region, and both the total and the maximum radiated power increase rapidly, so that more than ten times as much total radiative loss is seen with $T_e(r_{21})=20-40$eV. The position of maximum power also shifts rapidly inwards and locates near the inner island edge.

The time–dependent effect of the results of figure 6.2 would be to lead to radiative contraction of the plasma. As the island cooled this would lead to greater impurity content, the radiation loss would therefore increase, producing even stronger cooling of the island. Without the enhanced island transport this positive feedback effect of the radiation cooling on itself still exists, but in a much weaker form. The profile modification of this cooling will have a strong destabilizing effect on the island, so it is useful to see how the radiated loss varies with island size. In figure 6.3 r_{21} is fixed at 0.75a, $T_e(0)=400$eV, $T_e(r_{21})=80$eV, while h_{21} now varies. The figures here plot equivalent quantities to figure 6.2. The important point to note here is that for fixed $T_e(r_{21})$ the radiation losses decrease smoothly as the island becomes larger. This agrees qualitatively with figure 6.2 as the outer temperatures are less for small h_{21} so more impurities are allowed into the plasma. Two competing effects are illustrated here:

(i) Cooling of the island produces an increase in radiation.

(ii) Growth of the island decreases the radiation losses.
The combined effect of the radiation–island interaction is therefore complicated and must be observed time–dependently.

6.4 *Radiation–Induced Disruptions*

A simulation is presented here of the effect on island stability of a sudden influx of oxygen impurity ions into a stable tokamak discharge. A stable DITE discharge with $q_a = 4.5$, $n_D = 3\times10^{19}m^{-3}$, and no radiation losses is set up in figure 6.5 by running TRID for 40ms from initialisation. At this time the impurity influx is modelled by linearly increasing the neutral oxygen density at the wall from zero to $3\times10^{15}m^{-3}$ in 4ms, after which time it remains constant. Current and deuterium density are assumed constant throughout the simulation. It is convenient at this point to define the impurity fraction f of the discharge as the ratio of the neutral oxygen density at the limiter to the average deuterium density:

$$f \equiv n_0(a)/n_D \qquad (6.11)$$

The fitted model $P_f(T)$ is not used in this instance but system (6.2) is solved in full. Several plasma quantities, from just before impurity influx until disruption, are shown in figure 6.5. They are:
a) The positions of the 3/1, 2/1, and 3/2 islands. No sawtoothing is present until near 54ms when the mixing radii (crosses) intersect the outer islands. The dashed line follows the position r_p of the peak in the radiation loss.
b) The 2/1 and 3/1 (dashed line) island widths.
c) Electron and ion axial temperatures.
d) The electron temperatures of the 2/1 and 3/1 islands.
e) The average effective ionic charge.
f) The average impurity fraction, i.e.: $n_{ox}/n_D \equiv \int\Sigma n_z(r)rdr/\int n_D(r)rdr$.
g) The total input (ohmic) power, and the total radiated power.
h) The ratio of the perturbed radial magnetic field at the limiter to that of the zero order poloidal field, for the 2/1 and 3/1 modes.
The radiation induced disruption has the following scenario.

Initially the radiated power increases as the impurity fraction increases, cooling the outer plasma only, as evidenced by a falling T_{isl} and constant $T_e(0)$. This causes contraction and peaking of the current profile, and the $q=2$ surface moves outwards in

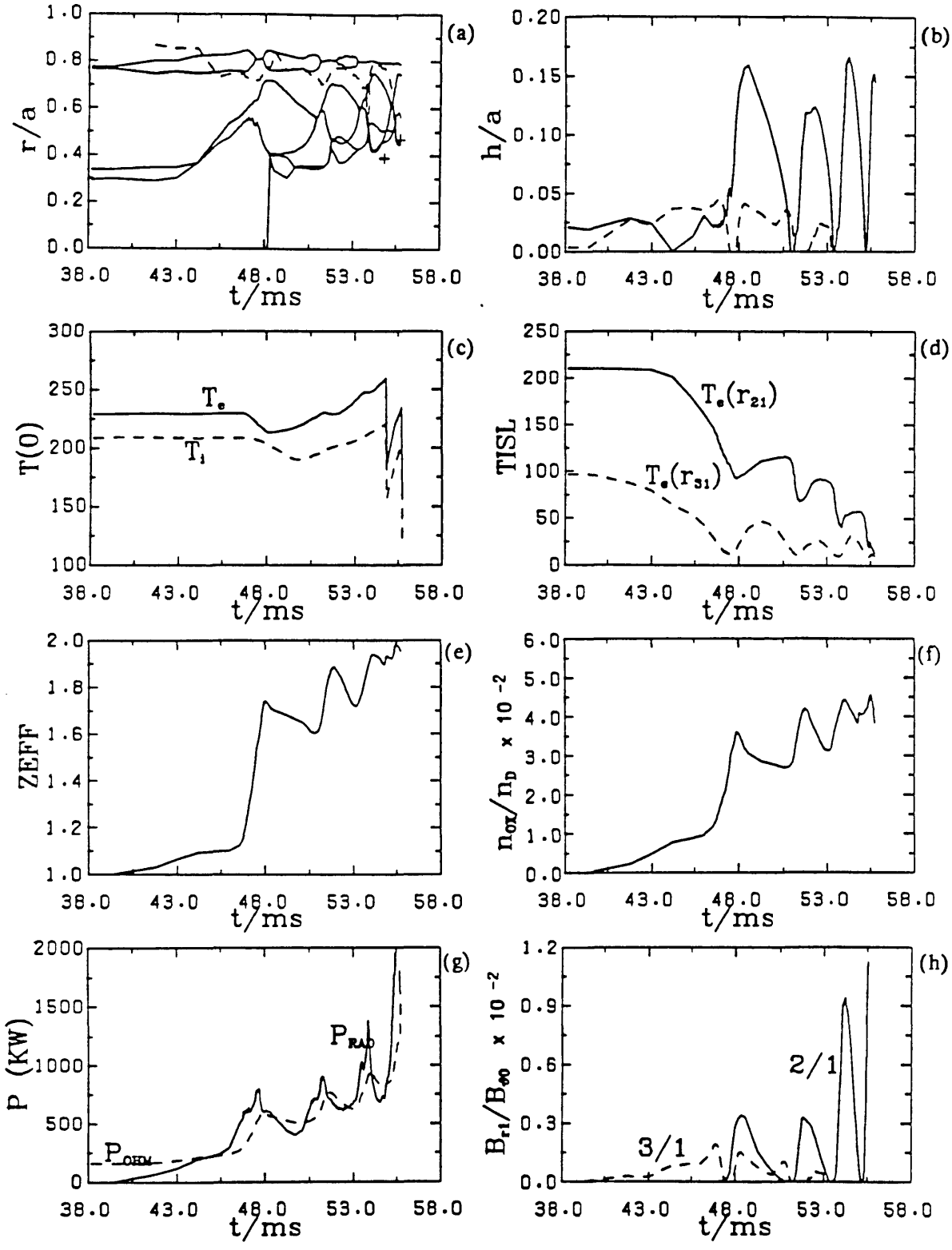

Figure 6.5 Simulation showing the results of a sudden oxygen impurity influx with limiter density $n_0(a)=3\times10^{15}m^{-3}$, at t=40ms, into a DITE plasma with $n_D=3\times10^{19}m^{-3}$ and $q_a=4.5$ (description of curves can be found in section 6.4).

radius, with the 2/1 island however remaining stable. At 45ms there is an increase in the total radiated power from one to two times the input power, associated with the 3/1 island becoming larger and r_p moving inside the $q=3$ surface. As the 3/1 island grows it allows the lower ionized states to penetrate deeper into a more dense part of the plasma where they radiate more strongly. At this time Z_{eff} and n_{ox}/n_D, which are closely correlated, also increase significantly, while T_{isl} falls rapidly. The flattened current profile leads to an explosive growth of the 2/1 island, but this strong growth, along with induced 3/2 growth has a stabilizing effect, and h_{21} then decays to zero. The process repeats giving further oscillations, with a collapse of island temperature whenever the mode is destabilized and strong island growth occurs. Each collapse leaves a cooler island than the previous one, and eventually at $t=53.5$ms and again at $t=55$ms the radiation losses become large over both the island and exterior regions, and r_p moves rapidly inward to locate at the inner edge of the 2/1 island. Figure 6.4 plots the electron temperature, the radiated power profiles, and the current profile at $t=52$ms (dashed lines) before strong radiation cooling of the island, and after it commences at $t=55$ms (solid lines). After 55ms the plasma is very cool from 0.4a to the limiter, and radiation is large over this region. The outer region current is restricted and a skin current diffuses inwards, to give $q<1$ and sawtooth behaviour. As the outer plasma is cold the sawtooth collapses are very large, indicating likely disruption. Prior to the cooling of the 2/1 island and collapse of T_{isl}, a lossy, MHD–active, but non–disruptive plasma is present, but after the island–radiation interaction disruption appears inevitable.

Figure 6.6 shows an identical simulation to figure 6.5 but with q_a now equal to 3.0. The curves in both figures plot equivalent quantities except figure 6.6(f) plots the sawtooth period and not the average impurity fraction. After impurity influx the resonant surfaces shift outward slightly and a modest increase in h_{21} to 0.075a results. No disruption is observed and a steady state with $P_{rad}/P_{in}=0.4$ is attained. This relatively low radiation fraction, along with the absence of a 3/1 mode to aid impurity penetration means no radiative contraction occurs and h_{21} remains stable. The most noticeable effect of the radiation in this case is on the sawtooth. The larger, radiatively cooled 2/1 island contracts the current profile, forcing the $q=1$ surface to greater radii. The collapses have greater amplitude, the period is reduced (for the reasons of section 4.6), and therefore the ramp phase has a more linear shape than figure 4.6.

A further radiating, non–disruptive DITE discharge, similar to figure 6.5, is simulated in figure 6.7. The safety factor is again 4.5 but a smaller fraction

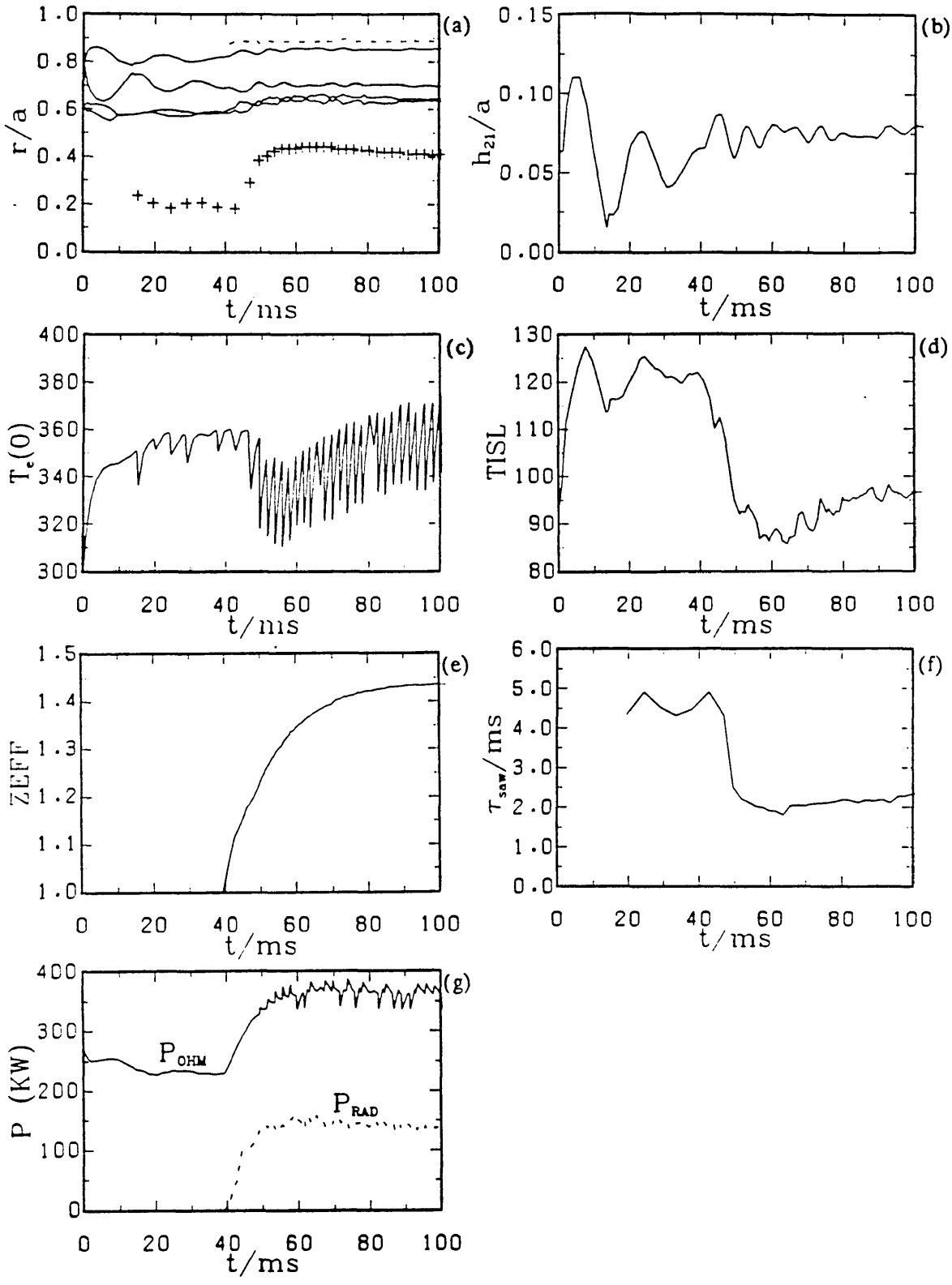

Figure 6.6 Equivalent simulation to figure 6.5, but with q_a now equal to 3.0. The same quantities are plotted, except for (f), which shows the sawtooth period.

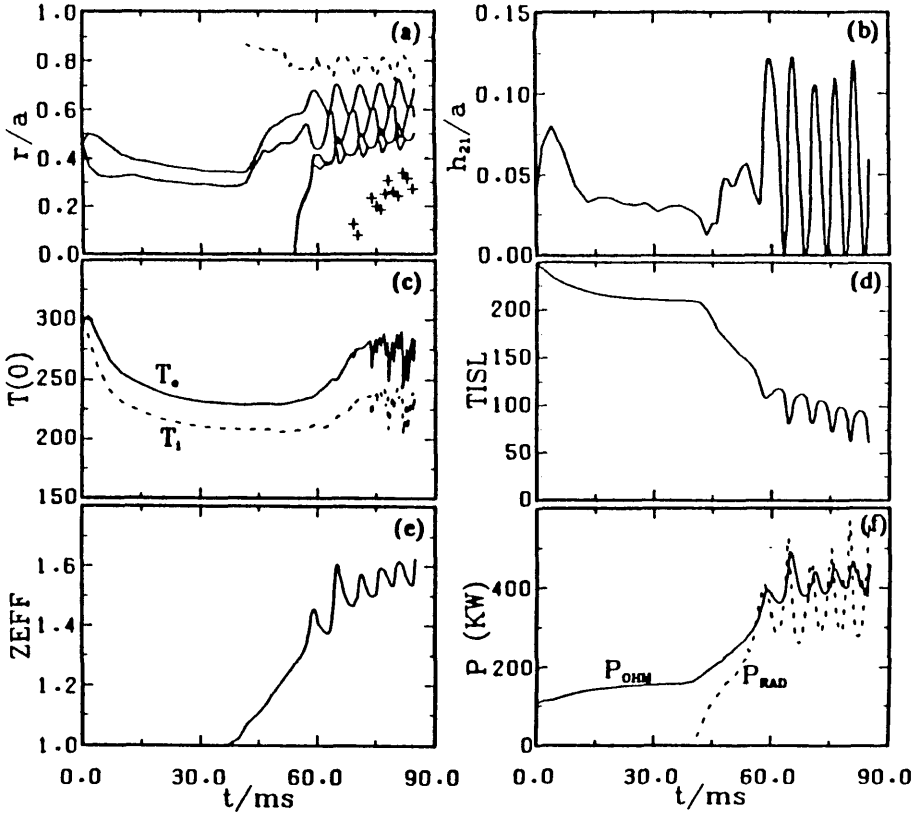

Figure 6.7 *Impurity influx simulation similar to fig. 6.5, with* q_a=4.5 *and* $n_0(a)/n_D$=$1.8\times10^{15}/3.0\times10^{19}$. *No disruption is observed.*

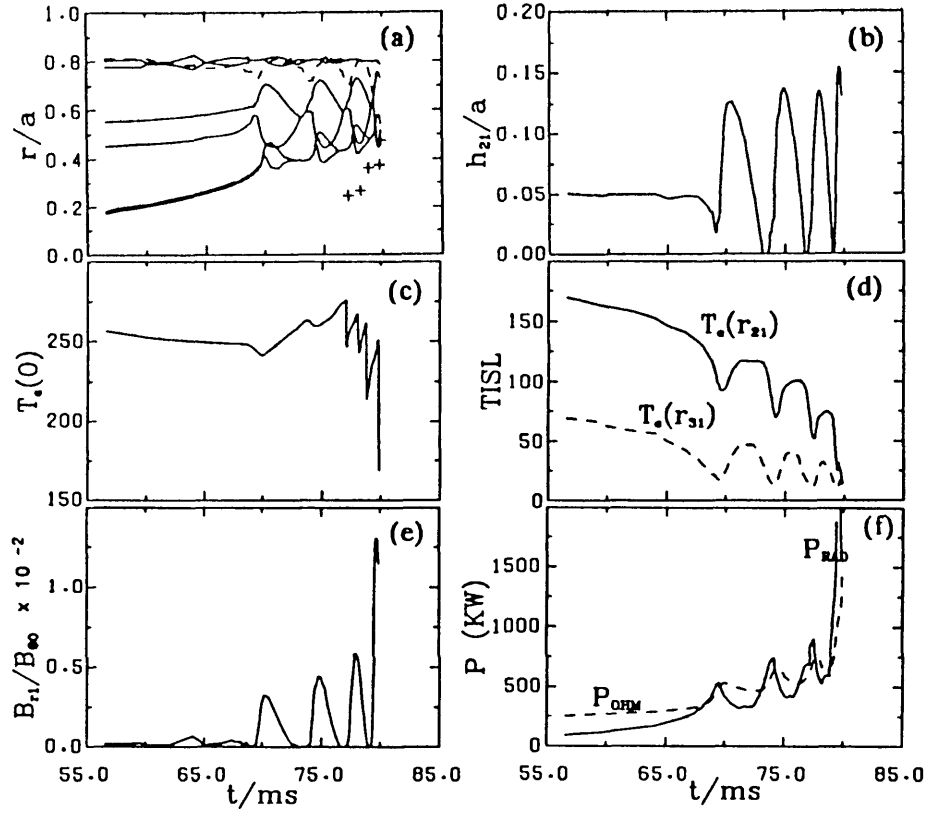

Figure 6.8 *Density ramp simulation of DITE plasma with* q_a=4.5. *The ramp is switched on at t=40ms, when* n_D=$1\times10^{19}m^{-3}$, *and doubling time for density is 20ms. Disruption observed at t=79.8ms.*

$n_0(a)/n_D = 1.8\times10^{15}/3\times10^{19}$ of oxygen is introduced into the plasma at t= 40ms. Similar behaviour to the oscillations observed in figure 6.5 results, but the radiation in this case is insufficient to cool the island, and no collapse of T_{isl} and r_p is seen. The 3/1 island remains stable and is not shown. Variable amplitude sawtoothing is initiated, with largest collapse correlated with a large 2/1 island also being present. The total radiation losses do at times exceed the input power but P_{rad}, along with T_{isl}, also exhibit oscillatory behaviour correlated to h_{21}. The times at which the island goes unstable and suddenly begins to grow are also precisely the times at which the island temperature T_{isl} begins to drop rapidly. Peaks in the impurity radiation correspond to minima in T_{isl}, in agreement with the predictions of section 6.3. The changes in T_{isl} are in the range 30−40%, and resemble the "minor" disruptions in ref. [83].

Finally for this section the results of a density ramp simulation are shown in figure 6.8. A DITE plasma with $q_a = 4.5$, $n_D = 1\times10^{19}m^{-3}$, and a constant impurity fraction $f = 10^{-4}$, is run from initialisation toward equilibrium, until at t= 40ms a density ramp is switched on. The doubling time for the density is 20ms, and as the TRID model does not include evolution of the deuterium density, the Gaussian profile shape is assumed unchanged while n_D increases linearly. Time dependent simulation of the background plasma density profile is a necessary extension to the TRID model. After t= 40ms the radiation losses in figure 6.8(f) initially increase quadratically (see eq.(6.15)), and both $T_e(0)$ and T_{isl} gradually fall, while the islands are unaffected. However at t= 68ms P_{rad} becomes equal to P_{ohm}, r_p moves inward, T_{isl} begins to drop more rapidly and the 2/1 island is very suddenly destabilized. The plasma recovers from this mode destabilization as at this time the radiation losses are insufficient to cool the island and cause a total collapse in T_{isl}. After several such oscillations in h_{21} and T_{isl}, the radiation losses are great enough to cause disruption, almost identical in nature to that in figure 6.5. Disruption occurs for this current and impurity fraction at a density of $n_D = 3.0\times10^{19}m^{-3}$. Variation of this density limit is examined in the following section.

The onset of destabilization of the 2/1 mode, for the simulations of this section, coincides with the ratio Φ of radiated power to input power becoming equal to one. In the next section the $\Phi = 1$ criterion for 2/1 destabilization is found to be independent of current. This criterion has been previously proposed [70] as a necessary, although not sufficient criterion for producing thermal contraction of the plasma. [70] then argued that such a contracted plasma would be unstable to tearing modes and disruption would result. The simulations here not only support this argument, but links the $\Phi = 1$ criterion directly to 2/1 instability. However figure 6.7 shows that although

$\phi = 1$ is sufficient to produce 2/1 instability, it does not necessarily guarantee disruption. The island is not cooled, T_{isl} remains high, and the profiles are not contracted sufficiently for the sawtooth to interact. In figure 6.8 the density and radiation continually increase and only when losses are sufficient to cause a collapse in T_{isl} does disruption occur. This implies figure 6.7 is a discharge very close to disruption, and that only a small increase in f or n_D would be sufficient to cause one.

6.5 *Disruption Control with Additional Heating*

In section 5.5 stabilization of the 2/1 island was achieved with additional heating outside the 2/1 resonant surface. Prior to the disruption in figure 6.5 the 2/1 island width grows to large size, so if a condition such as $h_{21} > h_{21,crit}$ (= 0.12a for example) were used as the trigger for such an exterior region heating pulse, then stability should be restored and disruption prevented. This hypothesis is tested in figure 6.9, where the simulation in figure 6.5 of impurity influx at t= 40ms is repeated. In figure 6.9(a) to (c) a 10ms pulse of 300kW of additional heating, centered at 0.75a with width $h_w = 0.1$a, is switched on when $h_{21} > 0.12$a. The other figures are for various other combinations of heating position, power and heating time, as described in the figure.

In (a) and (d) the condition $h_{21} > 0.12$ is met at t= 48ms, heating halts the collapse in $T_e(r_{21})$, and outer region temperatures are raised so impurity levels and P_{rad} fall. The q= 2 resonant surface moves inward as current diffuses into the hotter outer region and after a brief delay the 2/1 island starts to decay, finally reaching a near steady value of ≈0.03a. The heating is switched off at 58ms, but the island remains stable for a considerable time after this until P_{rad} exceeds P_{ohm} and $T_e(r_{21})$ collapses again. In (a) the final island behaviour prior to disruption is then identical to figure 6.5. In (d) the heating is reapplied at t= 72 and 100ms when $h_{21} > 0.12$a a second and third time. The heating periodically forces $T_e(r_{21})$ to rise and provides stability of the 2/1 island, but with the impurity content fixed at $f = 10^{-4}$, the current and temperature then try to collapse again when H_e is removed.

The other simulations have been made with the same triggering condition for H_e but with different centres of heating. If $r_H = 0.3$ (i.e. just inside the island) then large oscillations in h_{21} are not prevented but island temperatures are raised sufficienly to prevent a buildup of impurities and radiative collapse. If the heating is not pulsed but applied continuously after 58ms then an equilibrium containing a large 2/1 island of width $h_{21} = 0.1$a results. In the case of axial heating then giant sawteeth are initiated.

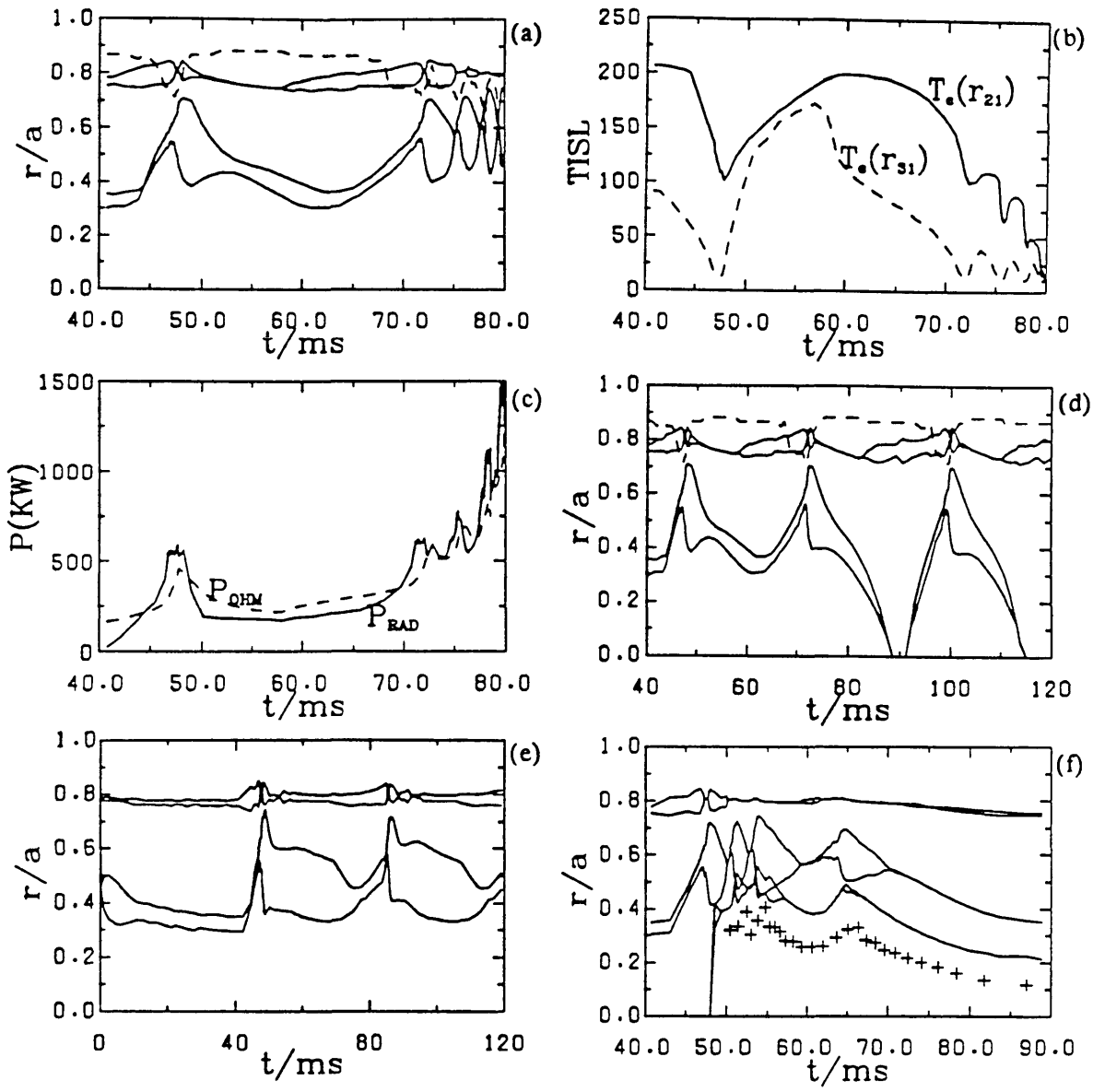

Figure 6.9 *Impurity influx simulations similar to 6.5 but with various forms of additional electron heating, triggered when $h_{21}>0.12a$.*

(a) to (c): Island positions and temperatures, and the total ohmic and radiated powers, for a single 10ms heat pulse with $P_H=300kW$, $h_w=0.1a$, and $r_H=0.75a$.

(d): Same as (a) but heating is applied periodically whenever $h_{21}>0.12a$.

(e): Island positions for 10ms heat pulses applied periodically. $P_H=300kW$, $h_w=0.1a$, $r_H=0.3a$.

(f): Island positions with continuous axial heating switched on when h_{21} first exceeds 0.12a. $P_H=300kW$, $h_w=0.2a$, $r_H=0.0a$.

If the applied power is great enough, as in figure 6.9(f), the island temperatures are raised sufficiently so that outer region current restriction does not force the subsequent sawteeth to large enough radii so they interact with the island and radiation dominated region. With lesser amounts of applied power, or greater impurity fractions than in (f), then the outer region is cooled more and disruption results. Axial additional heating is therefore less reliable in controlling disruptions.

The results of this section are consistent with section 5.5. Additional heating prevents collapse and disruption, with maximum 2/1 stabilization if $r_H > r_{s21}$. If the impurity levels are constant then disruption is delayed until after the end of the heat pulse. To test these predictions experimentally, a triggering condition for heating could be supplied by the B_{r_1} perturbations (proportional to h^2; see eq.(4.18)) reaching some critical level.

6.6 *Disruption–Free Operating Regions*

The maximum density attainable before disruption varies with current, and this relationship is traditionally shown with the aid of a Hugill diagram, which plots $1/q_a$ on the vertical axis, and on the horizontal axis the maximum value before disruption of the average "normalised" density: $n_M \equiv n_D \times 10^{-19} R/B_z$. Figure 6.10 is such a diagram [70], that plots the instant of disruption for a series of ohmic discharges on JET. Disruption–free operation is possible to the left–hand side of the straight–line curve that has been fitted to the data. This experimentally observed linear relation between current and density limit was first observed by Murakami et al. [71], and so the density limit is now given in terms of the Murakami parameter (symbol M here):

$$\frac{n_D}{10^{19}} \equiv M \frac{B_z}{R q_a} \qquad (6.12)$$

which for figure 6.10 approximately equals 12. Prior to disruption the total radiated power increases, reaching about 100% of the input power at disruption, when the 2/1 mode is destabilized as in section 6.4. A test for the TRID model of a radiation disruption is therefore to produce such behaviour for the density limit, and figure 6.11 shows the results.

Each point in figure 6.11 corresponds to a single TRID simulation of DITE that has been run from initialisation until disruption occurs. A slow ramp in time of the density is applied, the impurity fraction is constant, and the current is a prescribed

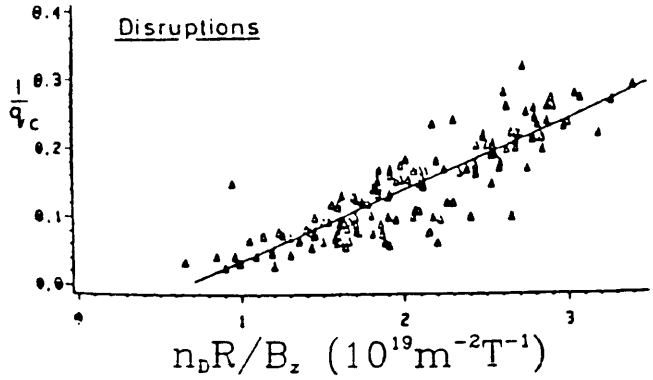

Figure 6.10 Hugill plot of density limit disruptions in JET ohmic discharges (from [70]).

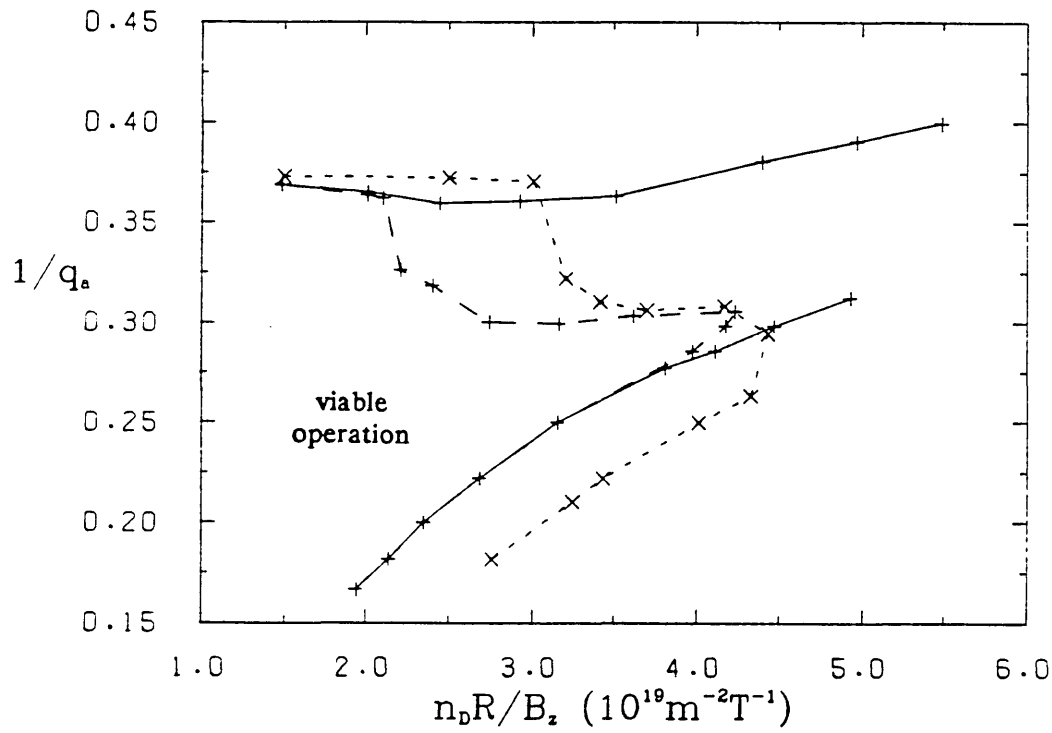

Figure 6.11 Hugill diagram obtained from TRID simulations. Disruption-free operation is possible in the lower left region of the figure. The three cases shown are (i): $f=10^{-4}$, 2/1 island only (solid line), (ii): $f=10^{-4}$, 2/1 and 3/1 islands (large dashed line), (iii): $f=0.5\times10^{-4}$, 2/1 and 3/1 islands (small dashed line).

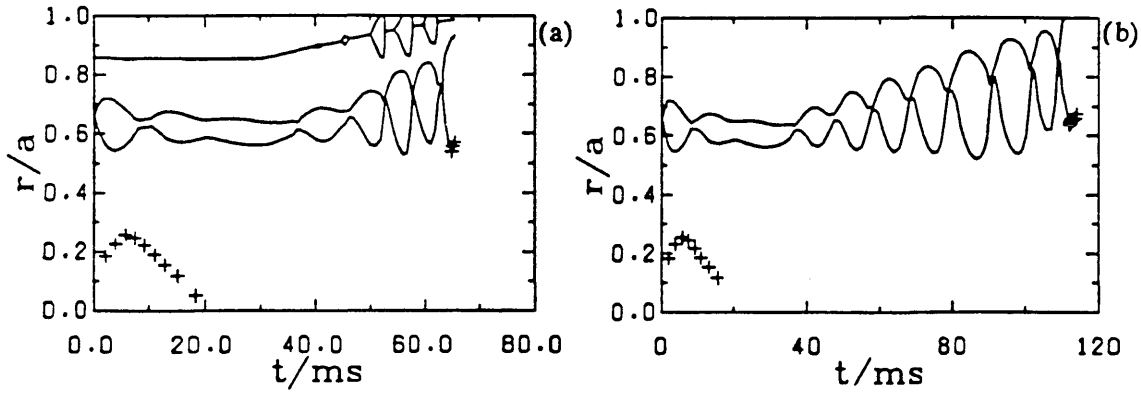

Figure 6.12 Comparison of island behaviour with (a), and without (b) the 3/1 mode, during identical density ramp simulations (DITE, $f=10^{-4}$, $q_a(t=0)=4.0$, $n_M(t=0)=2$, $g=0.043$, $t_d=40ms$, ramp on at $t=30ms$).

linear function of density, so:

$$n_M(t) = n_M(0)(1+t/t_d) \qquad (6.13)$$

$$1/q_a(t) = 1/q_a(0) + g[n_M(t)-n_M(0)] \qquad (6.14)$$

Typically $n_M(0)=2$, $q_a(0)=4$, and $t_d=600$ms. g is the gradient of the straight-line trajectories the discharges follow in figure 6.11, from $(n_M(0),q_a(0))$ until disruption. The curve-fitted steady-state radiation model is used and the Kadomtsev sawtooth is explicitly modelled. As t_d is chosen large then the plasma will always be close to steady-state and the radiation model will be valid. Stable operation is obtained within the bottom left corner of figure 6.11 with the disruption boundaries corresponding to three different situations;

(i) solid line: $f=10^{-4}$, 2/1 island only;

(ii) large dashed line: $f=10^{-4}$, 2/1 and 3/1 islands included;

(iii) small dashed line: $f=0.5\times10^{-4}$, 2/1 and 3/1 islands.

With slowly varying quantities, other islands (eg 3/2 mode) only become unstable after destabilization by the 2/1 mode just prior to disruption and have a negligible effect on the stability limits of figure 6.11. With the shorter ramp times of experimental discharges, q_a would be able to reach lower values before disruption, so the curves given by TRID in figure 6.11 are conservative, and give lower bounds for the density limit.

The curves to the bottom right all represent density-limit disruptions. For low currents there is no difference between case (i) and (ii), the curves are close to linear, and the Murakami parameter goes from $M=11.8$ at $q_a=5.5$, to $M=12.6$ at $q_a=4.0$. With half the impurity fraction in (iii) and consequent reduction in radiation losses, the density limit shifts to the right, and M is increased to 15.4, and 16.1, for the same q_a values. As the trajectories are made steeper, then both the (ii) and (iii) curves turn over and give a disruption limit when the $q_a=3$ barrier is approached, while (i) shows no such limit. Figure 6.12 compares the island behaviour in a simulation including the 3/1 mode (a), with an identical simulation in which it is excluded (b). To allow equilibrium conditions to develop the density ramp is started after $t=30$ms, $t_d=40$ms, and the impurity fraction equals 10^{-4}. Initially $n_M=2$ and $q_a=4.0$, while during the density ramp eq.(6.13) applies with $g=0.043$. At the time of disruption in (a), $q_a=3.29$ and $n_M=3.25$, while in (b) $q_a=2.37$ and $n_M=6.0$. With sufficient radiation the 3/1 mode is destabilized as in (a) when q_a approaches 3, and the combined cooling due to the radiation and the island in turn destabilizes the 2/1 mode to initiate disruption. This difficulty in crossing the $q_a=3$ barrier is commonly encountered during tokamak discharges [72]. For small enough n_D the radiation losses are insufficient to

drive 3/1 unstable and the $q_a = 3$ barrier disappears. This occurs at higher density for case (iii) since the radiation losses are less. The near horizontal lines in figure 6.10(b) that then appear at high current ($q_a \simeq 2.6-2.7$) and low density (radiation) correspond to the current-limit disruptions described in sections 4.7 and 5.2. The stabilizing influence of plasma rotation [60] would imply current-limits closer to 2.0 and not the 2.6 reported here, but the TRID code gives a satisfactory representation of the density limit.

All three cases deviate from true linear behaviour, with M increasing for large $1/q_a$. This can be understood in terms of simple energy balance arguments. The 2/1 mode is destabilized when $\Phi = 1$, and as line radiation constitutes practically 100% of P_{rad} then

$$P_{rad} = 4\pi^2 Ra^2 (n_D \times 10^{-19})^2 f R_1 \qquad (6.15)$$

where the radiation factor R_1 is

$$R_1 = \int_0^1 \frac{n_e(r)}{n_D} \sum_Z \frac{n_Z(r)}{n_0(a)} \sum_j Q_{zj} \Delta E_{zj} e 10^{38} r dr \qquad (6.16)$$

The input power in figure 6.11 is purely ohmic:

$$P_{in} = \frac{4\pi^2 Ra^2}{\mu_0} \int_0^1 r j E dr = \frac{4\pi^2 a^2 B_z E}{\mu_0 q_a} \qquad (6.17)$$

and substituting for electric field E,

$$E = \frac{B_z}{\mu_0 q_a R} \frac{\eta_{sp}}{A(Z)} T_{e0}^{-3/2} p_1^{-1} \qquad (6.18)$$

where the temperature profile factor

$$p_1 = \int_0^1 \left[\frac{T_e(r)}{T_e(0)}\right]^{3/2} r dr \qquad (6.19)$$

gives for Φ:

$$\Phi = \left[\frac{q_a R n_D \mu_0}{B_z 10^{19}}\right]^2 \frac{f A(Z)}{\eta_{sp}} T_0^{3/2} p_1 R_1 \qquad (6.20)$$

In terms of the parameters in eq.(6.12) this gives

$$M = \left[\frac{\eta_{sp}\Phi}{A(Z) f \mu_0^2 p_1 R_1 T_{e0}^{3/2}}\right]^{1/2} \qquad (6.21)$$

A comparison of the quantities appearing in eq.(6.21) is made for $q_a = 4.0$ and 5.5 with $f = 10^{-4}$. For both cases just prior to disruption the average $T_e(0)$ is 300±20eV, and Z ($= Z_{eff}$) is also constant at 1.66. However both p_1 and R_1 vary slowly giving rise to the curved shape in figure 6.11, i.e.; $q_a = 5.5$: $p_1 = 0.11$, $R_1 = 1.52 \times 10^8$; $q_a = 4.0$: $p_1 = 0.076$, $R_1 = 2.62 \times 10^8$. At lower current the island is more deeply embedded in the plasma, and radiation cooling therefore covers a greater proportion of the outer region before the 2/1 mode feels it's influence and is destabilized. Temperature profiles are therefore more peaked at lower current prior to disruption, which is borne out by the increasing p_1 observed for higher $1/q_a$. The radiation factor has a complicated dependence on temperature through the impurity profiles and the excitation-rate coefficients, but is observed to decrease somewhat for increasing current, and this effect dominates p_1 variation to give the slightly higher M at higher current in figure 6.11. Equation (6.21) predicts a $\sqrt{2}$ increase in M when f is halved going from case (ii) to (iii), if all other factors remain constant. Figure 6.11 does give an increase, but of only 30%. In fact Z_{eff}, T_{e0}, p_1, and R_1 all vary significantly with f, making precise predictions of M difficult.

6.7 *Experimental Comparisons and Discussion*

A recent paper by Wesson et al. [83] reviews the experimental characteristics of JET disruptions, and seems to support many of the ideas presented here, while also describing new and unexplained disruption phenomena. Clear evidence is presented for a flattening of electron temperatures close to q= 2 resonant surfaces, and this can be correlated to a large island growing at this surface. The curves labelled T_o and T_x in figure 6.13(a) correspond to radial temperatures measured at the o-point and x-point respectively, and show asymmetric islands, as proposed in section 2.4. These islands occur at the same time as bursts of m= 2, n= 1 $\dot{B}_\theta$ oscillations.

Prior to JET density limit disruptions, these precursor oscillations occur shortly after the radiated power fraction has become equal to one, and radiative contraction has begun, as in figures 6.5 and 6.8. However prior to, and during the contraction,

JET radiated power−loss profiles are poloidally asymmetric. Before the point of 100% radiation, most power is radiated from plasma interacting with the limiter on the large major radius side of the tokamak. As density increases, P_{rad} increases to equal the input power and a "marfe" thermal instability occurs (a toroidally symmetric, but poloidally localized region, on the small major radius side, of dense, cold and strongly radiating plasma). After a short time (50−100ms) the marfe decays, the temperature starts to shrink away from the limiter, and the radiation then becomes poloidally symmetric as the profiles contract.

The 1−D nature of the TRID radiation model precludes nothing more than a good qualitative description of the earlier features of the asymmetric radiation profile, but the radiative contraction stage is well described. Oscillations in P_{rad} and P_{ohm} in ref. [83] during density ramp discharges resemble those of the simulations of the previous section.

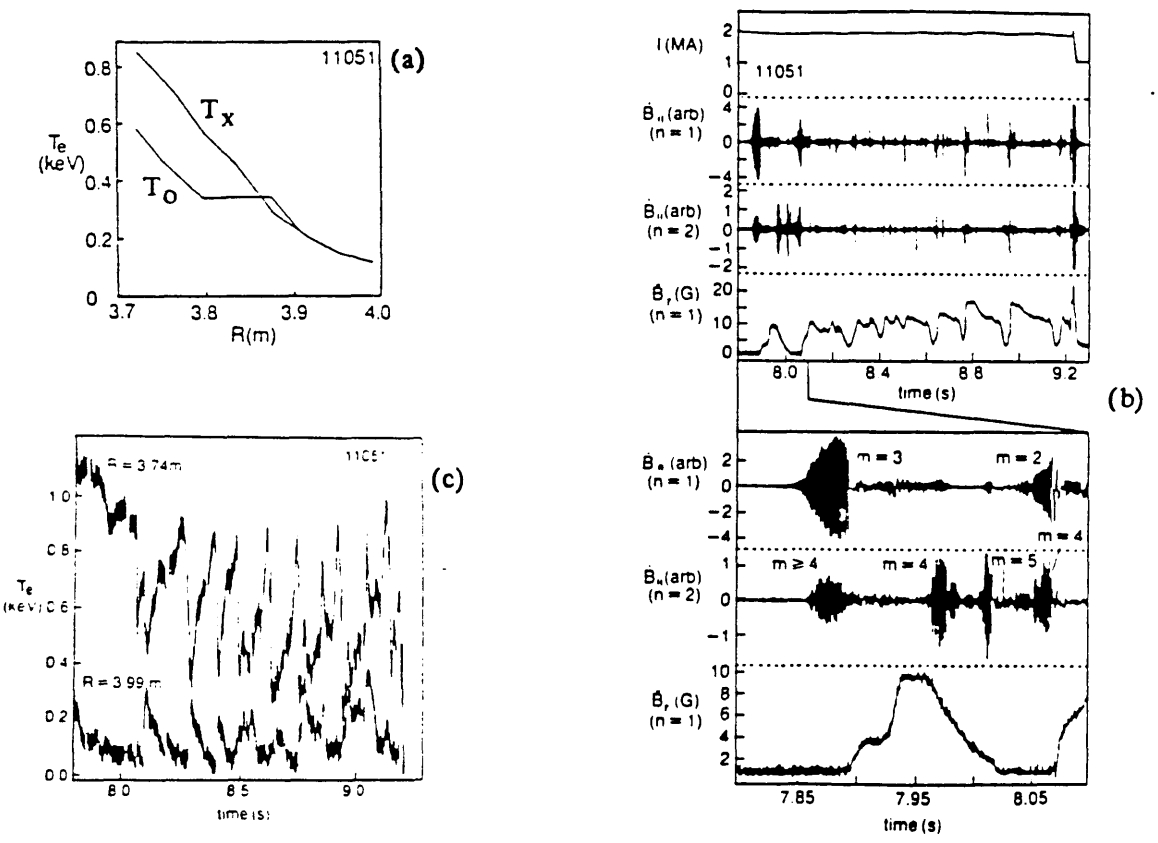

Figure 6.13 (a) Measured temperature profiles on JET through the o−point and x−point. (b) JET sequence of MHD oscillations preceding a major disruption at 9.25s. (c) T_e for the discharge in (b) above, at radial positions 3.74m close to the q=2 resonant surface, and at 3.99m outside the 2/1 island. Profile flattening is observed during minor disruptions that is correlated to sudden growth in the B_{r_1} signal (from [83]).

The magnetic precursor oscillations are in general very complicated, with a typical JET sequence, after radiative contraction and prior to disruption, shown in figure 6.13(b). Figure 6.13(c) shows the corresponding electron temperatures signals, at radii calculated to be at the resonant surface R= 3.74, and just outside it. It is the 3/1 island that first becomes unstable, and after initial growth, locking of the mode rotation occurs so that $\dot{B}_\theta$ disappears and B_r begins to grow. It then decays away and a burst of m= 2 $\dot{B}_\theta$ oscillations is then observed. The associated 2/1 island in turn locks, and then repeatedly oscillates in size, as indicated by the oscillations in the B_r signal. Each sudden growth in B_r (or h_{21}) is correlated to a minor disruption, with a rapid collapse (2–3ms in JET) of the island temperature, and a small rise in temperature outside. After a series of such minor disruptions, a major disruption at 9.25s terminates the discharge.

Although the simulations in this chapter were made with DITE parameters, it is found with JET parameters that the island behaviour is very similar to that described here. In both figures 6.5 and 6.8 the 3/1 mode is the first to be destabilized, as in figure 6.13, and the 2/1 mode then shows unstable behaviour, with sharp drops in $T_e(r_{21})$ occurring whenever sudden growth of the 2/1 island is initiated. The number of minor disruptions is less in the simulations, but figure 6.6 shows that as this depends sensitively on the impurity fraction then more or fewer collapses would be expected with small changes in f. The shape of the B_{r1} signal also differs with the experimental signal often exhibiting a flat–top phase (sometimes with a moderate linear decrease) between periods of more rapid growth and decay, whereas the simulated signal is more sinusoidal in nature. The experimental minor disruptions also have a significantly greater amplitude of T_e collapse, and between minor disruptions the ramping of $T_e(r_{21})$ is more linear than that of the simulations.

These discrepancies could be due to a variety of factors, including:
(i) The basic simplicity of the 1D TRID model.
(ii) The assumption of constant impurity fraction after radiative contraction. Inclusion of a plasma–wall interaction model (eg ref. [81]) within TRID would obviate the need for such an assumption.
(iii) Neglect of the deuterium density evolution.
(iv) Neglect of carbon and heavy impurities.
Nevertheless the TRID model gives support to the assertion that minor disruptions are due to successive destabilizations of the 2/1 magnetic island by impurity radiation.

New light has also been provided by ref. [83] on the mechanisms of the final

energy quench and major disruption of the plasma. During the density ramp phase prior to radiative contraction, steady sawtoothing is generally observed, even for high q_a [84], while with TRID simulations sawtoothing only begins when $q_a \approx 3.1$ (fig. 5.1). A significant reduction in axial $K_e(r)$ (eg. setting α to ≈ 2.5 in eq.(5.8)) is found to be the only way, in the transport studies here, of allowing a sufficient peaking of T_e and j to drive q(0) below one and so initiate high$-q_a$ sawtoothing. Before disruption though the normal sawtooth activity frequently stops, but during the final energy quench a m=1, n=1 structure develops that, through what has been described as a profile "erosion", leads to flattened, symmetric profiles [83] with a loss of half the plasma energy. One ms later (typically) a rapid loss of the remaining energy occurs and the n=1 and n=2 modes rapidly grow to large amplitude, and following this the current decay begins. Resolution of the temperature profiles shows no displacement of the central region of the plasma, as would be expected with the rigid shift eigenfunction of the m=1 mode. These experimental findings seem to require the growth of a m=1 mode that is locally zero on axis. Another disturbing feature of JET discharges is that recent Faraday rotation measurements [85] have shown that the axial q value is possibly as low as 0.8 throughout the normal sawtooth cycle.

These observations are at odds with the current sawtooth theories described in chapter 4, and in particular with the TRID model for the final energy quench of the Kadomtsev sawtooth interacting with the radiation$-$island cooled outer region. However as this work is primarily concerned with influences on the pre$-$disruptive state, then knowledge of the actual mechanism of the final energy quench is not required. It is apparent though that the sawtooth oscillation still remains one of the most important unsolved problems in tokamak physics today.

CHAPTER 7

CONCLUSIONS

7.1 *Summary*

Chapter 1 introduced the experimental characteristics of a typical tokamak disruption, and discussed the motivations for gaining a greater understanding of their causes and dynamics. This disruptive instability is linked to the sudden growth of resistive MHD instabilities, so chapter 2 then reviewed the linear theory of tearing modes and the energy source for their growth. The need for a nonlinear treament when magnetic islands exceed the tearing width is highlighted, and the derivation of the saturated island growth expression is discussed in some detail. Chapter 3 then describes how the island growth can be coupled to a 1D transport code, in a similiar fashion to the TRINIO code [9]. When flattening of the current due to enhanced island transport is accounted for, then this gives greater island stability to that provided by quasilinear effects alone.

There is agreement between the gross features of the current-limited disruption when modelled by TRINIO and by TRID. The experimental disruption signatures of growing $m=2$ magnetic perturbations, and loss of core thermal energy correspond to interaction of the sawtooth with a large, cool 2/1 island. In chapter 4 it is shown that strong island growth occurs prior to limiter intersection, when the $q=2$ resonant surface approaches the plasma boundary so that outer region current stabilization largely disappears, and when sawtoothing gives rise to steep current gradients inside the $q=2$ surface. Once the island intersects the limiter, rapid loss of island thermal energy increases η_S and island growth accelerates, but more significantly the cooling of the outer region restricts the current flowing there, the $q=1$ surface expands in radius and and subsequent sawtooth collapse overlaps the cold island region to give a thermal shortcircuit.

To model the sawtooth explicitly the well known Kadomtsev prescription for the post-collapse profiles is used. The trigger for collapse is assumed to be a $m=1$ resistive mode, whose linear growth is reduced by diamagnetic effects. The growth rate and size of the perturbation is shown to be small throughout almost all the ramp phase, so the linear assumption is good. The sawtooth periods predicted are in the range 1.5 to 4.5ms for DITE, and 20 to 50ms for JET, with no heating or radiative

cooling. There is good agreement for DITE, but the periods are a factor of 2 to 4 too small to account for typical JET sawtooth periods. The usefulness for 1–D transport codes of a minimum energy state model for the post–collapse profiles was investigated. The arbitrariness in mixing radius, the strong dependence of sawtooth period on r_m, and the necessity for considering a redistribution of toroidal magnetic energy rendered this approach impractical. If only the average effect (restriction of axial current) of the sawtooth oscillation is considered, then good agreement with the current–limited disruption with explicit sawtoothing is obtained.

Detailed analysis was made of the effect on plasma dynamics of additional modes with $m>2$. Neglect of the 3/2 mode is unjustified. It's stability is strongly coupled to the 2/1 mode through the zero–order current, and it's growth provides an additional stabilizing influence to quasilinear effects for the 2/1 mode. Inclusion of the 3/2 mode induces island oscillations on the resistive timescale of the outer region. Prior to disruption when the sawtooth region is close to these two modes then a successive destabilization of modes with increasing poloidal mode number occurs. This is the first time an inwardly accelerating "shock–front" has been reported in 1D, and agrees with a full 3D simulation. This supports the validity of the simple model of tearing instability discussed here. However the onset of disrupton may be understood in terms of the interaction of just two MHD modes, the 2/1 tearing mode, and the sawtooth oscillation.

Prior to the current–limited disruption large sawtooth collapses in $T_e(0)$ of 20% are observed, when r_m is close to the outer region occupied by large $m\geq 2$ islands, and these could be interpreted as "minor" disruptions. The actual current limit corresponds to $q_a = 2.6-2.7$. This is due to the effects of the first order term now included in the expression for island growth so for example when $q_a = 3.3$, h decreases from 0.095a to 0.055a. Neglect of this first order term is not justified if accurate saturated island widths are to be predicted, but the catastrophe model for current–limited models is still found to be valid.

The presence of a conducting wall at positions other than infinity is shown to be strongly stabilizing, with no disruptions predicted for a conducting wall on the plasma boundary. The saturated island width is shown to be independent of the conducting wall position when $q_a \geq 3.0$, and should be the same for both rotating and mode–locked modes. Modelling of the current–limit with a constant $b/a = \infty$ could therefore be invalid with poloidal rotation, but for density–limit disruptions where q_a is much greater than 3 then the conducting wall can be neglected.

The effect on island width of a spatially varying electron thermal conductivity was examined. The width is largely independent of $K_e(r)$ with no sawtoothing, although the position of the island moves outwards with increasing steepness of K_e. Eventually reduction of $K_e(0)$ allows sufficient peaking of current and initiates sawtoothing. The sawtoothing region increases in size with increasing K_e', and the resultant steepening of the outer current profile produces a steady growth in h_{21}. Constant or gradually varying $K_e(r)$ give profiles that are most stable to island growth.

The response of saturated islands to additional heating has been modelled and is broadly similar for just electron heating only, or else only ion heating. Axial heating produces giant sawteeth whose periods agree, perhaps fortuitously, with those in additionally heated JET discharges. Simultaneously the 2/1 island shifts outwards and is much reduced in size. If heating is applied outside the island then the axial value of the safety factor may rise sufficiently to remove the 2/1 mode altogether from the discharge, although only a small rise in core temperature results. However heating applied just inside the inner edge of the island is strongly destabilizing. The resulting island can be over 200% greater than with no heating, although it moves inward away from the outer cooler region, while the increased current permitted in this region removes sawtoothing. Therefore even with the larger island present, these discharges are not likely to be more disruptive. Clearly though, additional heating should be preferably axial, to maximize both the thermal energy content of the plasma, and the stability of the 2/1 island.

The hypothesis that steep pressure profiles between the $q=2$ and $q=1$ surfaces would be ballooning unstable was not proven. However due to the presence of low–shear regions after sawtooth collapse, ballooning was predicted on axis during steady sawtoothing, and at greater radii prior to disruption. The q profiles however depend delicately on the collapse dynamics, and the doubts concerning the sawtooth collapse must also apply to these predicted ballooning mode unstable regions.

A hydrodynamic–coronal model for the densities of oxygen impurities and the radiation they emit has been combined with the transport code. This coupling of radiation to islands and transport cannot be neglected since idealised temperatures showed at least a ten–fold increase in radiated power when the island temperature was cooled to become comparable to the temperature of peak radiation power density. However an increase in island size with constant island temperature was predicted to give a modest reduction in radiation loss. With this model, radiation–induced

disruption at low current for both a sudden impurity influx, and a linear density ramp have been simulated. When the radiated power and input ohmic power become equal then radiative collapse begins, and the position of peak loss moves rapidly inward. The small, quiescent islands present are destabilized, but disruption is only initiated if the radiation losses are strong enough to begin cooling the 2/1 island. If not then island oscillations are predicted.

A curve-fit model for the oxygen impurity radiation losses allowed simulations of many near steady-state radiating equilibria in the DITE tokamak. Agreement was observed between experimental density limits, and the point in the simulations at which destabilization and cooling of the 2/1 mode occurred, giving disruption. At high impurity concentrations difficulty in crossing the $q=3$ barrier was observed since the 3/1 island was then destabilized, allowing the impurities to penetrate deeper to cool the 2/1 island. Additional heating prevents radiative collapse and disruption, but once heating is removed the plasma subsequently disrupts if the impurity radiation source is not also removed. Additional heating outside the $q=2$ surface offers the best chances for disruption control.

7.2 *Conclusions and Further Work*

The requirements for disruption are:

(i) The growth to large size of a 2/1 magnetic island. This can drive other modes unstable.

(ii) Cooling of the 2/1 island by interaction with either a limiter or else a cold plasma region cooled by light impurities. This restricts the outer region current near $q=2$.

(iii) Expansion in radius of the sawtoothing region until it overlaps with the outer modes and the thermal quench occurs.

In the absence of a conducting wall, condition (i) occurs when the 2/1 surface is in close proximity to the plasma boundary, while at lower current this sudden growth is initiated by radiative collapse of the plasma. The sawtooth is responsible for the final thermal quench, but the validity of the Kadomtsev prescription with the trigger proposed here is still an open question. With present-day knowledge, and with the evidence presented here it remains the most complete and useful description for one dimensional modelling. Should other mechanisms for the final sawtooth collapse (such as the toroidal ideal internal kink discussed in chapter 4) eventually supercede the Kadomtsev model, this does not invalidate the events described here leading to

disruption, although the precise triggering condition for interaction of some internal region instability with the cold outer plasma would no doubt change. Continued research into the mechanisms of the sawtooth collapse is a necessity. Questions regarding the existence or not of low—shear ballooning unstable regions could also be resolved.

The 1D simulations presented here with quasilinear saturation of magnetic islands, plus an enhancement of radial transport across islands not only models the gross experimental features of the predisruptive plasma, but also in many respects agrees with the fine details of 3D simulations. The simplicity of a one dimensional teatment allows analysis of the effect on disruption of variations in heating and radiation parameters. It is possible to stabilize the 2/1 island growth, and prevent disruption, with additional heating of the exterior region. A coupling of ray—tracing models of ICRF heating to the transport code would allow more precise prediction of the island dynamics with additional heating, but it is unlikely the general conclusions would change.

A limitation of the code described here is that the deuterium density remains constant in time. Implementation of particle diffusion would be a useful extension to the TRID code, and although this should not alter the gross behaviour of the islands presented here, the impurity radiation profile would then be more accurately calculated, and this could be significant. Low Z impurity contamination of some level is unavoidable in tokamaks, but only if these levels can be minimized through careful wall conditioning will the likelihood of density—limit disruptions be reduced. The q—limit near $q_a = 2$ is simply avoided by operating at lower current, and if clean discharges are achievable then the $q_a = 3$ limit is also avoidable. The probability of disruption is inevitably finite though, and only practical operating experience can determine what disruption frequencies are possible.

APPENDIX A

LINEAR GROWTH RATE OF THE TEARING MODE

In the interior region, $x<<x_T$ so $\psi_1''>>k^2\psi_1$, $\psi_1''>>k^2\varphi_1$, and $F(x)\simeq x$. The constant-ψ approximation is also made [73]. It assumes that within the tearing layer $\psi_1\simeq\psi_1(0)$ is constant, equivalent to requiring $\Delta' x_T<<1$. Equations (2.22) and (2.23) become

$$\psi_1(0)-x\varphi_1(x) = (\gamma\tau_R)^{-1}\psi_1''(x) \tag{A.1}$$

$$\gamma^2\tau_A^2\varphi_1''(x) = -x\psi_1''(x) \tag{A.2}$$

Equation (A.2) is integrated across the tearing layer and if this is to be matched to the exterior solution then

$$\frac{-\gamma^2\tau_A^2}{\psi_1(0)}\int_{-x_T}^{x_T}\frac{\varphi_1''(x)}{x}dx = \Delta' \tag{A.3}$$

The asymptotic ($x\to\infty$) behaviour of φ is assumed to give constant ψ_1' and so allow matching to Δ'. The limits of the integral in eq(A.3) are therefore extended to $\pm\infty$, and convergence guarantees matching. Once the solution for φ_1 is known, eq.(A.3) determines γ. Equations (A.1) and (A.2) are combined, eliminating ψ_1'', and a convenient rescaling is made,

$$x \equiv \left[\gamma\tau_A^2/\tau_R\right]^{1/4}z \tag{A.4}$$

$$\varphi_1 \equiv -\left[\tau_R/\gamma\tau_A^2\right]^{1/4}\psi_1(0)\chi(z) \tag{A.5}$$

so $\chi(z)$ satisfies

$$\chi''-z^2\chi=z \tag{A.6}$$

and the matching condition becomes

$$\gamma^{5/4}\tau_R^{3/4}\tau_A^{1/2}\int_{-\infty}^{\infty}\frac{\chi''}{z}dz = \Delta' \tag{A.7}$$

Equation (A.6) was first solved in ref.[73], but Rutherford and Furth [74] give a simple form for the solution,

$$\chi = -\frac{z}{2}\int_0^1 \left[1-u^2\right]^{-1/4} \exp\left[-\frac{1}{2}z^2 u\right] du \qquad (A.8)$$

that asymptotically gives constant ψ_1' in the interior. With (A.8) the matching condition gives

$$\gamma = \left[\frac{\Gamma\left[\frac{1}{4}\right]\Delta'}{2\pi\Gamma\left[\frac{3}{4}\right]}\right]^{4/5} \tau_A^{-2/5} \tau_R^{-3/5} \qquad (A.9)$$

This implies $\gamma\tau_A \approx S^{-3/5} << 1$ and the timescale assumption is verified. Note there is a typographical error in [21] and [75]; a missing factor of two in the denominator of eq.(A.9).

If the integration (A.7) is truncated at $z = \pm 2$, then very little error results, so x_T is set to

$$x_T = 2\left[\gamma\tau_A^2/\tau_R\right]^{1/4} = 2(0.55)^{1/4}\Delta'^{1/5}S^{-2/5} \qquad (A.10)$$

It scales as $S^{-2/5}$ times the shear length and is very small.

APPENDIX B

RECURSIVE INVERSION OF A BLOCK TRIDIAGONAL MATRIX

Equations (3.36) and (6.2) have the form:

$$A_i u_{i-1} + B_i u_i + C_i u_{i+1} = w_i \tag{B.1}$$

where the A,B,C and w are matrices. A recursive method [32] is used to find u. Assume the solutions at adjacent mesh points are related by

$$u_{i+1} = X_i u_i + Y_i \tag{B.2}$$

where X is a matrix, and Y a column vector. If (B.2) is substituted into (B.1) then

$$u_i = -(B_i + C_i X_i)^{-1} A_i u_{i-1} + (B_i + C_i X_i)^{-1}(w_i - C_i Y_i) \tag{B.3}$$

This is identical in form to (B.2) so the following identifications can be made:

$$\begin{aligned} X_{i-1} &= -(B_i + C_i X_i)^{-1} A_i \\ Y_{i-1} &= (B_i + C_i X_i)^{-1}(w_i - C_i Y_i) \end{aligned} \tag{B.4}$$

The boundary condition for (B.1) at i= N is

$$A_N u_{N-1} + B_n u_n = w_n \tag{B.5}$$

which implies

$$\begin{aligned} X_{N-1} &= -B_N^{-1} A_N \\ Y_{N-1} &= B_N^{-1} w_N \end{aligned} \tag{B.6}$$

Therefore once X_{N-1} and Y_{N-1} are known, all other X_i and Y_i can be found recursively, sweeping down to i= 0 in (B.4). Using (B.2) with i= 0 and the boundary condition for (B.1) at i= 0:

$$B_0 u_0 + C_0 u_1 = w_0 \tag{B.7}$$

an equation for u_0 is obtained

$$u_0 = (B_0 + C_0X_0)^{-1}(w_0 - C_0Y_0) \qquad (B.8)$$

Beginning with u_0, X_0 and Y_0, eq.(B.2) can be solved recursively for u_i. The procedure described is general for any matrix size, and contains many matrix operations. These are performed using the NAG Program Library [35]. In the case of the matrices being just simple coefficients, no matrix algebra is required.

APPENDIX C

NUMERICAL BIFURCATION

An interesting numerical instability was observed in TRID when the average effect of the sawtooth was modelled by a highly enhanced conductivity for $r \leqslant r_m$. For small enough Δt the solutions approached a steady state as expected, but for Δt greater than some critical value the solutions bifurcated, after initially appearing to converge toward the steady state. Within the iteration at each timestep the temperature and field profiles always converge, but between successive timesteps the solutions oscillate and after a long time these oscillations settle on two steady solutions. This oscillation occurs only when $q<1$ somewhere and is an oscillation of the whole plasma radial profile but is best observed by examining the behaviour of r_{s1} or $T_e(0)$. Figure C.1 plots the asymptotic values of $T_e(0)$ against timestep Δt. For each value of Δt, TRID is run for a long time ($300\Delta t$) to allow transient behaviour to settle, and then 80 iterations are graphed. For this run DITE parameters were used, $q_a = 2.7$ and a 1-fluid simulation was implemented to save computer time , although the 2-fluid shows identical behaviour. We see that, as well as the first bifurcation at $\Delta t \approx 1.3$ms, as Δt is further increased, a point is reached at which each of the solutions itself bifurcates. This "periodic doubling" [76] continues with increasing Δt, but with ever decreasing increment between bifurcation, giving rise to 4,8,16... solutions. Finally for Δt 3.5ms the periodicity disappears and chaos appears. There is some evidence for "windows" at $\Delta t = 4$ where there are three separated chaotic bands but more points than have been plotted here are necessary to decide.

Bifurcation diagrams such as figure C.1(a) are common for models of population growth [76] and a universal charateristic of such period-doubling is the Feigenbaum number δ [77]. If Δt_n is the timestep at the nth birfurcation whose period 2^n goes unstable, then defining δ_n as the ratio of lengths of successive intervals between bifurcation:

$$\delta_n = \frac{\Delta t_n - \Delta t_{n-1}}{\Delta t_{n+1} - \Delta t_n} \qquad (C.1)$$

then $\delta = 4.669$ is the limit of δ_n as n tends to ∞. The question of whether this holds for the TRID instability is now examined. Figure C.1(b) has increased resolution near $\Delta t = 3$, and gives $\Delta t_2 = 2.48 \pm .01$, $\Delta t_3 = 3.07 \pm .01$, $\Delta t_4 = 3.21 \pm .01$, and hence $\delta_3 = 4.2 \pm 0.8$. It appears that the period-doubling here is not inconsistent with the Feigenbaum

number, although much finer resolution is needed to properly examine the limit.

If the alternative approach of fixing Δt and increasing K_1 is taken, then identical behaviour to figure C.1 is observed, with bifurcation leading to chaos once again characterised by δ. The value of K_1 at the onset of the first bifurcation decreases with increasing Δt. The consequence of this for TRID is to set a maximum limit for Δt, to remove any chance of bifurcation, but as this limit is of the same size as the timestep needed to adequately resolve moderate island growth, it is not too troublesome.

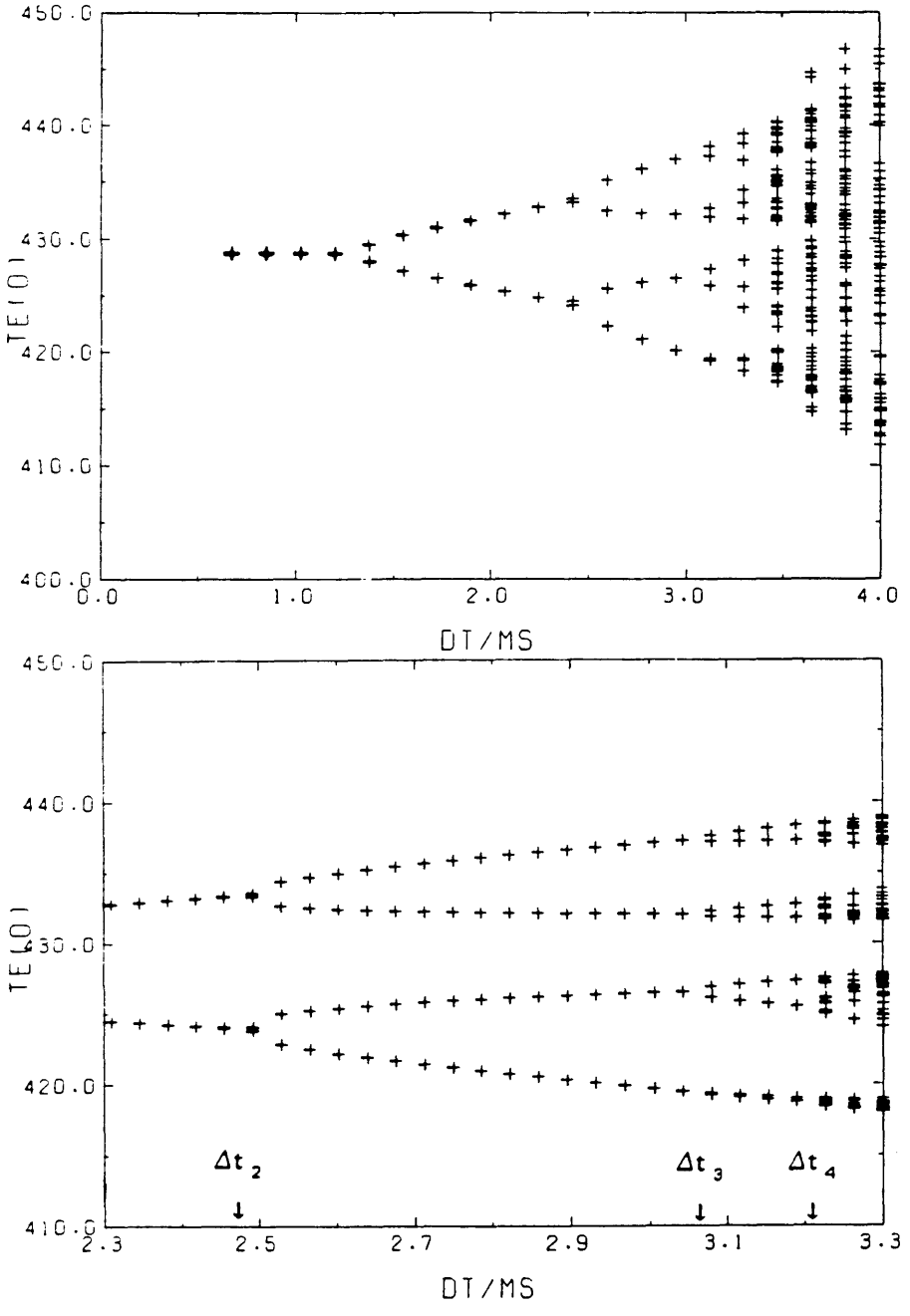

Figure C.1 *(a) Bifurcation diagram of $T_e(0)$, as a function of Δt, for the sawtooth model with K_1=100. (b) Same as (a) but with increased resolution.*

APPENDIX D

DISPERSION RELATION FOR THE M=1 MODE

The outer solution for ξ, eq.(2.72), must be matched to the inner solution, but this is impossible with eq.(2.72), which was found with the reduced equations derived to lowest order in the expansion parameter kr/m. The exterior solution for ξ must be found to the next order, so writing $\xi(r)=\xi_0+\xi_1(r)$ then [52]

$$\begin{aligned} \xi=\xi_0, \quad \xi_1' &= \frac{\xi_0}{r\left[m\psi_0'\right]^2}\int_0^r g\,dr \qquad r<r_s \\ \xi=0, \quad \xi_1' &= \frac{\xi_0}{r\left[m\psi_0'\right]^2}\int_0^{r_s} g\,dr \qquad r>r_s \end{aligned} \tag{D.1}$$

where g is given for example in [52,79]. As $r\to r_s$ then

$$\frac{1}{\xi_0}\frac{\partial\xi}{\partial r}\bigg|_{r\to r_s} = \frac{-\lambda_H}{\pi x^2} \tag{D.2}$$

$$\text{where } x=r-r_s, \quad \text{and } \lambda_H = \frac{-\pi\int_0^{r_s} g\,dr}{r_s\left[B_{\theta s}q_s'\right]^2} \tag{D.3}$$

λ_H is proportional to the linear growth rate of the ideal internal kink [79]. It is eq.(D.2) that gives the matching condition. Coppi et al [52] have done this analytically with the cylindrical analogues of eqs.(A.1) and (A.2) valid in the interior region. Waddell et al. [53] extended this linear analysis to include dimagnetic drifts, and this is now briefly reviewed.

The starting point for this analysis are the two-fluid equations of Braginskii [78]. The reduced equations for toroidal current and momentum balance are essentially unchanged from before, i.e.:

$$\mu_0 j_z = \nabla_\perp^2\psi - \frac{2k}{m}B_z \tag{D.4}$$

$$\rho\frac{d}{dt}\nabla_\perp^2\varphi + \nabla_\perp\rho\cdot\frac{d}{dt}\nabla_\perp\varphi = z\cdot(\nabla_\psi\times\nabla j_z) + z\cdot\nabla\times\Pi_i \tag{D.5}$$

Π_i is the viscous drag. Before linearizing eq.(D.5) it is noted that equilibrium quantities

vary only in r, and there is now an equilibrium velocity in the z direction,

$$v = z\times\nabla\varphi + v_{z0}z \tag{D.6}$$

$$v_{z0} = \frac{-p'_{i0}}{neB_{\theta 0}} + \frac{E_{r0}}{B_{\theta 0}} \tag{D.7}$$

If perturbations have the form $\varphi_1(r)e^{-i\tilde{\omega}t+i(m\theta+kz)}$ then the electric field part of v_{z0} introduces a Doppler shift to $\tilde{\omega}$, so $E_{r0}/B_{\theta 0}$ may be omitted replacing $\tilde{\omega}=i\gamma+\omega_D$. It is also noted in [53] that the magnetic part of the viscosity cancels with the inertial term arising from v_{z0}, and so within the tearing layer eq.(D.5) becomes

$$\rho_0\left[\gamma-\mu\frac{\partial^2}{\partial x^2}\right]\varphi'' = \frac{im\psi'_0}{\mu_0 r_s}\psi''_1 \tag{D.8}$$

where $m\psi'_1/r << \partial\psi'_1/\partial x$ is assumed, and the viscosity parameter μ is defined by

$$\mu = \frac{3T_i}{10m_i\omega_i^2\tau_i} \tag{D.9}$$

but shall be neglected in this analysis. Equation (D.8) is analagous to (A.1)

A second equation valid in the interior comes from reconsidering the reduced equation for magnetic flux, but this time using a generalised Ohm's law for electric field. First note from the definition (2.44) of B that

$$-\psi = A_z - \frac{kr}{m}A_\theta \tag{D.10}$$

$$\text{or } \psi=-h.A, \text{ defining } h\equiv z-\frac{kr}{m}\theta\ . \tag{D.11}$$

Faraday's law can then be written

$$\frac{\partial\psi}{\partial t} = h.E+h.\nabla\varphi = h.E \tag{D.12}$$

The generalised Ohm's law for E, neglecting viscosity, can be written [53,80]

$$E = -v\times B + \frac{1}{ne}j\times B + \frac{1}{ne}R - \frac{1}{ne}\nabla p_e + \frac{m_e}{ne^2}\left[\frac{dj}{dt}+\frac{1}{n}j.\nabla nv-\frac{1}{ne}j.\nabla j\right] \tag{D.13}$$

$$\text{with}\qquad R = ne\eta\left[j_{||}+2j_\perp\right] - 0.71nb(b.\nabla)T_e - \frac{3}{2\omega_e\tau_e}n\left[b\times\nabla T_e\right] \tag{D.14}$$

Equation (D.12) becomes, neglecting all terms of order $(kr/m)^3$ and $(kr/m).(p/B^2)$,

$$\frac{\partial\psi}{\partial t}+\mathbf{v}.\nabla\psi = \frac{1}{ne}\mathbf{j}.\nabla\psi + \eta\left[j_z+2\tau_e\frac{d}{edt}j_z\right] - \frac{0.71}{eB_z}\mathbf{B}.\nabla T_e \qquad (D.15)$$

Use has been made of the identity $\mathbf{h}.(\mathbf{c}\times\mathbf{B})=\mathbf{c}.\nabla\psi$, where $\mathbf{c}$ is an arbitrary vector. Operating on the single fluid momentum balance equation with $\mathbf{b}.$ $(=\mathbf{B}./B)$, and neglecting terms of order γ/ω_i one finds

$$\mathbf{j}.\nabla\psi = B_z^{-1}(\mathbf{z}\times\nabla p).\nabla\psi \qquad (D.16)$$

so the final form for the flux equation is

$$\frac{\partial\psi}{\partial t}+ \mathbf{v}.\nabla\psi+ \left[\frac{1}{neB_z}\nabla p\times\mathbf{z} + \frac{0.71}{neB_z}\nabla T_e\times\mathbf{z}\right].\nabla\psi = \eta\left[j_z+2\tau_e\frac{d}{edt}j_z\right] \qquad (D.17)$$

When linearized this becomes

$$[\gamma+i\omega_{*e}]\psi_1-\psi_0'v_{r1} = \frac{im}{eB_z r_s}\left[\frac{p_1}{n}+0.71T_{e1}\right]\psi_0'-\frac{\eta}{\mu_0}\left[1-2\tau_e\left[\gamma-i\omega_{*i}\right]\right]\psi_1'' \qquad (D.18)$$

where the diamagnetic frequencies are defined by

$$\omega_{*i} \equiv \frac{mp_{0i}'}{ner_sB_z} \qquad (D.19)$$

$$\omega_{*e} \equiv \frac{mp_{0e}'}{ner_sB_z} + \frac{0.71mT_{e0}'}{er_sB_z} \qquad (D.20)$$

To find the perturbed pressure p_1 and temperature T_{e1}, the heat balance equations are used, ignoring $\nabla.\mathbf{v}$, and transport terms that prevent further analysis [53]. For example ion heat balance implies $dp_i/dt= 0$, and after linearization it is found that

$$p_1 = \frac{v_{r1}p_0'}{\gamma+i\omega_{*i}}, \qquad T_{e1} = \frac{v_{r1}T_{e0}'}{\gamma+i\omega_{*i}}. \qquad (D.21)$$

With p_1 and T_{e1} defined, and $\psi_0'\equiv- |\psi_0''|x$, eq.(D.18) gives the second interior equation, analogous to (A.2):

$$\gamma_i\psi_1-v_{r1}x|\psi_0''| = \frac{\eta}{\mu_0}\eta^*\psi_1'' \qquad (D.22)$$

where

$$\eta^* \equiv [1-2\tau_e[\gamma-i\omega_{*i}]]\frac{\gamma_i}{\gamma_e} \quad , \quad \gamma_i \equiv \gamma+i\omega_{*i}, \quad \gamma_e \equiv \gamma-i\omega_{*e} \tag{D.23}$$

At this point it is convenient to normalize time to the poloidal Alfven time

$$\tau_A = \frac{m(\mu_0\rho)^{\frac{1}{2}}}{kB_z} \quad , \tag{D.24}$$

all lengths to a, ψ_1 to $kB_z a^2/m$, φ to a^2/τ_A, and we define

$$\alpha_s \equiv \frac{m|\psi_0''|}{r_s} = q_s' \quad , \tag{D.25}$$

in which case eq.(D.8) and (D.18) become

$$\gamma\varphi'' = -i\alpha_s x\psi_1'' \tag{D.26}$$

$$\gamma_i\psi_1 + i\alpha_s x\varphi = \frac{\eta^*}{S}\psi_1'' \tag{D.27}$$

To match to eq.(D.2), these interior region equations must first be written in terms of the displacement vector, which is defined by

$$\gamma_i\xi = -im\varphi/r_s \tag{D.28}$$

As x is expected to be small we rescale; $X \equiv x/\epsilon_1$, where ϵ_1 is the narrow singular layer width. ψ_1 is also rescaled by $\psi \equiv -\epsilon_1|\psi_0''|\Psi$ so

$$\Psi = -X\xi + \frac{\eta^*}{\gamma_i S\epsilon_1^2}\Psi_1'' \tag{D.29}$$

$$\xi'' = \frac{\epsilon_1^2\alpha_s^2}{\gamma\gamma_i}X\Psi'' \tag{D.30}$$

Defining the eigenvalue

$$\lambda \equiv S\gamma_i\epsilon_1^2/\eta^*, \tag{D.31}$$

then also requiring

$$\lambda^2 = \frac{\gamma\gamma_i}{\alpha_s^2 \epsilon_1^2} \tag{D.32}$$

implicitly defines the tearing width ϵ_1, and eqs.(D.29) and (D.30) can be solved [52,53] and matched to (D.2). It is found that

$$\Gamma\left[\frac{\lambda^{3/2}+5}{4}\right]\Gamma\left[\frac{\lambda^{3/2}-1}{4}\right]^{-1} = \frac{\lambda^{5/4}\lambda_H}{8} \tag{D.33}$$

The growth rate is obtained from λ by rearranging eqs.(D.31) and (D.32) so

$$\lambda^3\gamma_T^3 = \gamma\gamma_i\gamma_e \ , \qquad \gamma_T = S^{-1/3}\alpha_s^{2/3} \tag{D.34}$$

If the ideal internal m=1 kink is marginally stable (or stabilized by nonlinear effects at small amplitude) then $\lambda \to 1$ as the right hand side of (D.33) tends to zero. In the absence of diamagnetic effects then with $\lambda = 1$, eq.(D.34) shows that $\gamma = \gamma_T$, the growth rate of the pure m=1 resistive tearing mode.

ACKNOWLEDGEMENTS

It is a pleasure to thank:

Professor M.G.Haines, my supervisor, for his guidance and encouragement throughout the work described in this thesis;

Dr. K.I.Hopcraft for encouragement, advice and many valuable discussions;

Dr. P.Gibbon for the plotting routines;

Graham for proving it possible, and for looking after my sister;

Greg for his insanity, Marie–Laure for her sanity;

and all members, past and present, of the Plasma Physics Group of Imperial College.

This work would not have been possible without financial support from the 1851 Exhibition Scholarship, and the Edward Boyle Memorial Scholarship.

REFERENCES

1. M.Fleischmann, S.J.Pons, J. Electroanalyt. Chem., 261 (1989) 301.
2. F.Engelmann et al. Fusion Technology, 14 (1988) 30.
3. J.D.Lawson, Proc. Phys Soc. B, 70 (1957) 6.
4. J.A.Wesson, A.Sykes, M.F.Turner, Plasma Physics and Cont. Nuc. Fus. Res. (1985) Vol II, 23, IAEA Vienna (Proc. 10th Int. Conf. London 1984).
5. F.Karger et al. "Current Disruptions in Toroidal Devices", (Proc. IAEA Symp., Garching 1979), Max Planck Inst. Plasmaphysik, Garching, Rep. IPP 3/51 (1979) A4.
6. The JET Team, Plasma Physics and Cont. Nuc. Fus. Res. (1987) Vol I, 31, IAEA Vienna (Proc. 11th Int. Conf. Kyoto 1986).
7. S.M.Kaye, "Survey of Energy Confinement Scaling Expressions", Princeton PPL Report in Publication (1988).
8. INTOR Phase II-A, European Contributions to the Workshop, Group F (Physics).
9. M.F.Turner, J.A.Wesson, Nuc. Fus. 19 (1982) 1069.
10. B.B.Kadomtsev, Sov. J. Plasma Physics 1 (1975) 389.
11. S.I.Braginskii, in "Reviews of Plasma Physics", ed. M.A.Leontovich, vol 1, p205, Consultants Bureau, 1965.
12. G.Bateman, "MHD Instabilities", p32 MIT Press 1978.
13. F.Cap, "Handbook on Plasma Instabilities", vol 1, p310, Academic Press.
14. J.A.Wesson, Nuc. Fus. 18 (1978) 87.
15. F.L.Hinton, R.D.Hazeltine, Rev. Mod Phys. 48 (1976) 239.
16. M.N.Rosenbluth, D.A.Monticello, H.R.Strauss, Phys. Fluids, 19 (1976) 1987.
17. P.H.Rutherford, Phys. Fluids, 16 (1973) 1903.
18. R.B.White, D.A.Monticello, M.N.Rosenbluth, B.V.Waddell, Phys.Fluids, 20 (1977) 800.
19. H.R.Strauss, Phys. Fluids, 19 (1976) 134.
20. K.I.Hopcraft. A.Sykes, M.F.Turner, Nuc. Fus. 28 (1988) 1265.
21. E.A.Adler, R.M.Kulsrud, R.B.White, Phys. Fluids, 23 (1980) 1375.
22. G.Bateman, "MHD Instabilities", p96 MIT Press 1978.
23. A.Bondeson, Nuc. Fus. 26 (1986) 929.
24. L.Spitzer, R.Harm, Phys. Rev. 89 (1953) 977.

25. V.M.Leonov et al., Plasma Phys. Cont. Nuc. Fus. Res. (1981) Vol I, 393, IAEA Vienna (Proc. 8th Int. Conf., Brussels, 1980).
26. G.Becker, Nuc. Fus. 27 (1987) 11.
27. C.Bolton, A.A.Ware, Phys. Fluids 26 (1983) 459.
28. B.Coppi, N.Sharky, Nuc. Fus. 21 (1981) 1363.
29. C.Mercier, F.Werkoff, J.P.Morera, G.Cissoko, H.Capes, Nuc. Fus. 21 (1981) 291.
30. D.A.Monticello, R.B.White, Phys. Fluids 23 (1980) 366.
31. B.Carreras, H.R.Hicks, J.A.Holmes, B.V.Waddell, Phys. Fluids 23 (1980) 1811.
32. D.Potter, Computational Physics, John Wiley and Sons, London (1972).
33. S.C.Whitfield, PhD. Thesis, Imperial College, London (1985).
34. H.P.Furth, P.H.Rutherford, H.Selberg, Phys. Fluids, 16 (1973) 1054.
35. Numerical Algorithms Group, Oxford and Illinois, Program Library Mk 11.
36. J.Allen et al., Plasma Physics and Cont. Nuc. Fus. Res. (1987) Vol I, 227, IAEA Vienna (Proc. 11th Int. Conf. Kyoto 1986).
37. B.V.Waddell, B.Carreras, H.R.Hicks, J.A.Holmes, Phys. Fluids, 22 (1979) 896.
38. S.von Goeler, W.Stodiek, N.Sautoff, Phys. Rev. Lett. 33 (1974) 120.
39. K.McGuire, D.C.Robinson, Nuc. Fus. 19 (1979) 505.
40. D.J.Campbell et al., Nuc. Fus. 26 (1986) 1085.
41. M.N.Rosenbluth, R.Y.Dagazian, P.H.Rutherford, Phys.Fluids 16 (1973) 1894.
42. D.J.Campbell et al., Plasma Physics and Cont. Nuc. Fus. Res. (1987) Vol I, 433, IAEA Vienna (Proc. 11th Int. Conf. Kyoto 1986).
43. B.V.Waddell, M.N.Rosenbluth, D.A.Monticello, R.B.White, Nuc. Fus. 16 (1976) 528.
44. T.Yamauchi, T.Shoji, A.Funahaishi, K.Kumagai, Nuc.Fus. 20 (1980) 1381.
45. A.Sykes, J.A.Wesson, Phys. Rev. Lett. 37 (1976) 140.
46. W.Pfeiffer, F.B.Marcus, C.J.Armentrout, G.L.Jahns, T.W.Petrie, R.E.Stockdale, Nuc. Fus. 25 (1985) 655.
47. S.Yamamoto et al., Nuc. Fus. 21 (1981) 993.
48. D.J.Ward, PhD Thesis, Imperial College, University of London, 1987.

49. A.Sykes, J.A.Wesson, Nuc. Fus. 14 (1974) 645.
50. M.N.Bussac, R.Pellat, D.Edery, J.L.Soule, Phys. Rev. Lett. 35 (1975) 1638.
51. G.L.Jahns, M.Soler, B.V.Waddell, J.D.Callen, H.R.Hicks, Nuc. Fus. 18 (1978) 609.
52. B.Coppi, R.Galvao, R.Pellat, M.N.Rosenbluth, P.Rutherford, Sov. J. Plasma Phys. 2 (1976) 533.
53. B.V.Waddell, G.Laval, M.N.Rosenbluth, "Reduction of the Growth Rate of the m=1 Resistive MHD Mode by Finite Gyro-radius Effects." ORNL/TM-5968 Oak Ridge National Laboratory, Oak Ridge, Tennessee (July 1977).
54. W.Pfeiffer, Nuc. Fus. 25 (1985) 673.
55. J.A.Wesson, Plasma Physics and Controlled Fusion, 28 (1986) 243.
56. J.A.Wesson, P.Kirby, M.F.F.Nave, Plasma Phys. and Cont. Nuc. Fus. Res., (1987) Vol II, 3,IAEA Vienna (Proc. 11th Int. Conf. Kyoto 1986).
57. L.Woltjer, Proc. Nat. Acad. Sci., 44 (1958) 489.
58. B.Carreras, B.V.Waddell, H.R.Hicks, Nuc. Fus. 19 (1979) 1423.
59. K.I.Hopcraft, M.F.Turner, Phys. Rev. Lett. 56 (1986) 2372.
60. M.Persson, A.Bondeson, Theory of Fusion Plasmas, Proc. of the Workshop (EUR-11336-EN) Varenna, Italy 1987 (Bologna, Italy, Editrice Compositori 1988) 325.
61. D.E.Roberts, Nuc.Fus. 23 (1983) 311.
62. W.Stodiek, R.Goldston, N.Sautoff et al., Plasma Phys. Cont. Nuc. Fus. Res. (1981) Vol I, 9, IAEA Vienna (Proc. 8th Int. Conf., Brussels, 1980).
63. R.Bartiromo, M.Brusati, M.Buratti et al., Plasma Phys. Cont. Nuc. Fus. Res. (1981) Vol I, 43, IAEA Vienna (Proc. 8th Int. Conf., Brussels, 1980).
64. V.P.Bhatnagar. R.Koch, P.Geilfus, R.Kirkpatrick, R.R.Weynants, Nuc. Fus. 24 (1984) 955.
65. The JET Team, Plasma Physics and Cont. Nuc. Fus. Res. (1987) Vol I, 449, IAEA Vienna (Proc. 11th Int. Conf. Kyoto 1986).
66. D.Lortz, J.Nührenberg, J. Phys. Lett. A68 (1978) 49.
67. O.P.Pogutse, E.I.Yurchenko, JETP Lett. 28 (1976) 318.
68. D.E.Roberts, Nuc.Fus. 21 (1981) 215.
69. C.Breton, C.De Michelis, M.Mattioli, J. Quant. Spect. Rad. Trans.

19 (1978) 367.

70. J.Wesson, C.Gowers, W.Han, F.Mast, F.Nave, M.Turner, M.Watkins, Cont. Fusion and Plasma Physics (Proc. 12th European Conf. Budapest, 1985) Vol I, 147.
71. M.Murakami, J.D.Callen, L.A.Berry, Nuc.Fus. 16 (1976) 347.
72. F.C.Schuller, F.Alladio, D.Campbell, Cont. Fusion and Plasma Physics (Proc. 12th European Conf. Budapest, 1985) Vol I, 151.
73. H.P.Furth, J.Killeen, M.N.Rosenbluth, Phys. Fluids, 6 (1963) 459.
74. P.H.Rutherford, H.P.Furth, (1971), Princeton Plasma Physics Lab. Report No. Matt-872.
75. R.B.White, Rev. Mod. Phys., 58 (1986) 183.
76. R.L.Devaney. Introduction to Chaotic Dynamic Systems. Benjamin Cummings, Menlo Park, 1986.
77. M.Feigenbaum, J. Stat. Phys. 19 (1978) 25.
78. S.I.Braginskii, "Reviews of Plasma Physics", edited by M.A.Leontovich, (Consultants Bureau, New York, 1965) Vol 1, p205.
79. G.Bateman, "MHD Instabilities", (MIT Press, 1978), p117.
80. M.G.Haines, Plasma Phys. Cont. Nuc. Fus., 28 (1986) p1705.
81. M.Tendler, J.Neuhauser, R.Wunderlich, Nuc. Fus. 24 (1984) p989.
82. R.J.Hawryluk, S.Suckewer, S.P.Hirshmann, Nuc. Fus. 19 (1979) p607.
83. J.A.Wesson et al. Nuc. Fus. 29 (1989) p641.
84. D.J.Campbell, private communication.
85. J.O'Rourke, A.E.Edwards, R.D.Gill, M. von Hellermann, E.Lazzaro, G.Magyar, P.Nielsen, The Institute of Physics 16th Annual Conference on Plasma Physics, Univ. of York, July 1989.